Future global warming informed by past emissions and mid-Pliocene climate sensitivity

Michelle Dvorak

A dissertation
submitted in partial fulfillment of the
requirements for the degree of

Doctor of Philosophy

University of Washington

2025

Reading Committee:

Kyle Armour, Chair

LuAnne Thompson

Dargan Frierson

Program Authorized to Offer Degree:
School of Oceanography

University of Washington

Abstract

Future global warming informed by past emissions and mid-Pliocene climate sensitivity

Michelle Dvorak

Chair of the Supervisory Committee:
Kyle Armour
Oceanography

Warming over the next hundred years is almost certainly expected to differ from that of the next few decades, as evolving spatial patterns of sea surface temperatures modify the global radiative feedback and thus climate sensitivity. On much longer timescales, very slow feedbacks associated with the reduction of large ice sheets and changes in vegetation and biomes are expected to enhance the ultimate "Earth system" warming in response to greenhouse gas forcing. Present-day radiative feedbacks govern the modern geophysical climate commitment (i.e., the near-future warming that will occur from only past emissions), while past climate states, such as the mid-Pliocene, permit an examination of climate feedbacks operating on much longer timescales.

In Chapter 1, I describe the framework of global mean radiation balance in the climate system and the separation of forcings and feedbacks central to this thesis. I then introduce the mechanisms by which spatial patterns of sea surface temperatures alter the global mean radiative feedback. Lastly, I introduce the mid-Pliocene Warm Period (mPWP) and its utility as an analogue of future climate.

In Chapter 2, I use the framework of global energy balance to estimate the magnitude of global mean warming following an abrupt cessation of anthropogenic emissions – a geophysical climate commitment – both in the present-day and in the future, following realistic emissions pathways. I find that the probability of our past emissions committing us to surpassing 1.5°C of global warming, at least temporarily, is already greater than 40% (as of

2020), and increases to 66% by 2029.

In Chapter 3, I estimate the forcings and feedbacks operating in the mid-Pliocene in a global climate model hierarchy. I find that the non-CO_2 boundary conditions of the mPWP induce a spatial pattern of warming that results in a more sensitive climate relative to the modern-day, potentially reducing estimates of modern-day climate sensitivity that are constrained by mPWP warming. On long timescales, however, these feedbacks imply that Earth System Sensitivity may be higher than previously recognized.

In Chapter 4, I separate the climate response to the loss of the West Antarctic Ice Sheet from Northern Hemisphere boundary condition changes on the sea surface temperature patterns of the mPWP in a coupled climate model. I find that increasing high latitude ocean heat transport results in gradual Southern Ocean warming in response to a loss of the West Antarctic Ice Sheet, driving the higher sensitivity of this paleoclimate state. The results suggest that a loss of the West Antarctic Ice Sheet could produce more future global warming than previously appreciated.

TABLE OF CONTENTS

LIST OF FIGURES

ACKNOWLEDGMENTS

The author wishes to express her sincere appreciation to her advisor, Kyle Armour, and her supervisory committee members, LuAnne Thompson, Randie Bundy and Dargan Frierson, for their patience, kindness and enthusiasm for this work; to the encouraging and instructive faculty within the University of Washington's School of Oceanography, Department of Atmospheric and Climate Science, and Department of Earth and Space Sciences; to her fellow 2020 cohort within each of these departments, who helped her with her fluid dynamics homework –and so much more–; to her collaborators at other institutions of higher learning; to her loving family and friends, both near and far; and finally, to the UW Crags Climbing Center, for installing a climbing training board in an old squash court at the IMA.

DEDICATION

To the *Climate Dynamics* lab group: I hope this helps you decide if the oceans matter.

Chapter 1

INTRODUCTION

The question of how much more global warming we can expect in the future depends not only on our emissions, but also on the timescale that we are primarily concerned with, of which there are many different opinions even in the climate science community. The most commonly used metric of eventual climate change is the equilibrium climate sensitivity, or ECS, traditionally defined as the steady-state warming following a hypothetical doubling of CO_2 relative to preindustrial levels. This is a convenient definition for streamlining collaborative modeling efforts (i.e., Coupled Model Intercomparison Projects, or CMIPs), and has been shown to be well-correlated with projected 21st century warming within these models, making it a relevant measure of near-future warming (Sherwood et al., 2020). However, for oceanographers and geologists, the "E" in ECS is somewhat of a misnomer, as full equilibration to a perturbation of atmospheric CO_2 concentrations will rather take thousands of years to realize, as the deep ocean slowly circulates to the surface, and ice sheets and biomes adjust in size and type – hence a different metric, the "Earth System Sensitivity" (ESS). Nevertheless, for society, the 21st century is probably the most relevant timeline for informing immediate policy decisions, while a clearer understanding of the ultimate implications of our emissions is of relevance to those who concern themselves, or have a curiosity about, the fate of the Earth's ecosystems and posterity as a whole.

Generally speaking, the magnitude of global warming expected with any given radiative forcing (emissions) scenario can be estimated using a simple model of Earth's energy balance (Gregory et al., 2004):

$$\Delta N = \Delta F + \lambda \Delta T, \tag{1.1}$$

where ΔN is the global mean change in the top-of-atmosphere radiation imbalance (approximately equal to total ocean heat content change) for a given radiative forcing (ΔF) and

a radiative response at the surface that is proportional to the surface temperature change (ΔT), where λ is the net radiative feedback. The value of λ determines ECS in the case where the radiative forcing is that of the aforementioned doubling of CO_2 ($\Delta F = F_{2x}$), and the climate has reached equilibrium with respect to the net radiative balance at the top-of-atmosphere ($\Delta N = 0$):

$$\text{ECS} = -\frac{F_{2x}}{\lambda} \tag{1.2}$$

The satellite record of surface warming, combined with observations of ocean heat content change (ΔN) and modeled estimates of radiative forcing (ΔF) over the industrial era, can be used to estimate λ, and thus future warming – assuming no difference in λ between the observed climate, and that of the future.

In Chapter 2 of this thesis, I use equation 1.1 within a probabilistic framework that combines uncertainty in the best-available estimates of λ, and observed radiative forcing and heat uptake, to predict the magnitude of warming that can be expected along a variety of emissions scenarios, were we to abruptly stop emitting all anthropogenic greenhouse gases (GHGs) and forcing agents. I focus on short timescales: the few decades over which the climate warms in response to a reduction in short-lived climate forcers, such as aerosols, and the eventual temperature reached at the end of the century, when only long-lived GHGs (namely, CO_2) remain. Both are measures of "climate commitment" – the magnitude of temperature change that can be considered as an unavoidable geophysical response to past anthropogenic emissions, with clear relevance to policy targets and immediate climate trajectories.

That λ is, however, expected to change over time, and over climate states, is now widely accepted (e.g., Forster et al., 2021; Armour, 2017; Andrews et al., 2015; Armour et al., 2013; Caballero and Huber, 2013). This has been shown to largely result from evolving patterns of sea surface temperatures (SSTs): historically, the Earth has not warmed homogeneously, but with a trend toward enhanced warming that is collocated with areas of deep atmospheric convection in the western tropical Pacific (efficiently communicating that warming to space via enhanced longwave emission), and slight cooling in areas of atmospheric subsidence over the eastern tropical Pacific, favoring low-cloud growth in an area where the cloud feedback

is locally strongly amplifying (Andrews et al., 2018, 2022; Dong et al., 2019). In contrast, models tend to converge upon a more homogeneous pattern of surface warming in response to GHG emissions, which, all else being equal, leads to more enhanced warming globally via the activation of these same feedbacks. And because the warming is greater with this pattern of warming, per unit forcing, λ is less negative, implying a more sensitive climate – a phenomenon referred to in recent literature as the "pattern effect" (Stevens et al., 2016; Dong et al., 2019), the correction for which I will refer to as $\Delta\lambda$, following Cooper et al. (2024).

The next several hundreds to thousands of years is more difficult to model, both due to the high computational cost of running global climate models (GCMs) to equilibrium, and to the present lack of dynamical ice sheets within them. Most modeling studies focused on future projections assume fixed ice sheet mass and biomes for practical reasons. Past climate states, such as the Last Glacial Maximum and the mid-Pliocene Warm Period (mPWP), are therefore useful representations of the equilibrated earth system with respect to these slowly-evolving features. When used to help constrain estimates of modern-day ECS, it is common practice to treat these changes as forcing anomalies with respect to the modern-day climate, since they are not expected to be observed in response to GHG emissions on centennial timescales (Sherwood et al., 2020; PALEOSENS, 2012). Observational and modeling estimates of ice sheet extent and GHG concentrations (ΔF_{net}) and global temperature change (ΔT) enable an estimate of ECS that is informed by a broader range of known climate states (Sherwood et al., 2020).

But what about the pattern of surface warming, and therefore the global λ, of these paleoclimate periods? If ice sheet changes (a high latitude forcing) induce a pattern of warming that is coincident with postively-amplifying feedbacks, then the net pattern effect is toward a more sensitive climate ($\Delta\lambda > 0$). And, since these slow forcings are not expected to occur over the 21$^{\text{st}}$ century, this additional sensitivity, or "paleo-pattern effect," should be accounted for in estimates of ECS that are constrained by our knowledge of past climate states, with a view toward a less pessimistic prediction of the near-term future.

However, insofar as such ice sheet and vegetation changes are actually the ultimate response to an initial GHG forcing (either lower than preindustrial, as in the Last Glacial

Maximum, or higher, as in the mPWP), they should be treated as additional feedbacks on warming; the equilibrated temperature response, combined with an estimate of the known GHG forcing of the paleoclimate, then becomes a reasonable metric of climate sensitivity on very long timescales, or more specifically, ESS. The consequence of this definition being that a relatively small perturbation in GHGs, such as that which has occurred any number of times over the last several million years (and which has already occurred over the last several decades), can have an effect on global temperature beyond that which would be expected with the feedbacks that operate on a centennial timescale.

Given that the mPWP was a warm climate state with GHG concentrations similar to today's, it has often been invoked as an analogue of future warming. In Chapter 3, I show that if the mPWP is to be accurately used in this way, the drivers of warming, and the timescale on which it occurs, need to be elucidated. Toward that aim, I provide a quantification of the total forcing and feedbacks that give rise to the global warming of the mPWP in a GCM, with consequences for estimates of both modern-day ECS and future ESS.

The forcing-feedback framework described in this introductory chapter makes it clear that there is a difference between warming that is induced by large forcings over areas of stabilizing feedbacks, and that which is induced by small forcings acting upon de-stabilizing feedbacks (the latter indicative of a much more sensitive climate). In Chapter 3, I provide evidence to suggest that the climate of the mPWP may have been highly sensitive overall due to changes in ocean heat transport and high-latitude warming. In chapter 4, I then ask, can this be clearly attributed to the small forcing associated with the loss of the West Antarctic Ice Sheet, a feature relevant to the future climate on timescales of ESS? And, if so, how? I address this question using a hierarchy of GCM simulations in which the Antarctic ice sheet and northern hemisphere biomes of the mPWP are imposed separately, and show that an ocean dynamical response to a complete loss of the ice sheet leads to greater climate sensitivity.

Chapter 2

ESTIMATING THE TIMING OF GEOPHYSICAL COMMITMENT TO 1.5 AND 2.0°C OF GLOBAL WARMING

This chapter is published as: Dvorak, M.T., Armour, K.C., Frierson, D.M.W. et al. Estimating the timing of geophysical commitment to 1.5 and 2.0°C of global warming. *Nature Climate Change* **12**, 547–552 (2022). https://doi.org/10.1038/s41558-022-01372-y.

Abstract

Following abrupt cessation of anthropogenic emissions, decreases in short-lived aerosols would lead to a warming peak within a decade, followed by slow cooling as greenhouse-gas (GHG) concentrations decline. This implies a geophysical commitment to temporarily crossing warming levels prior to reaching them. Here we use an emissions-based climate model (FaIR) to estimate temperature change following cessation of emissions in 2021 and in every year thereafter until 2080 following eight Shared Socioeconomic Pathways (SSPs). Assuming a medium-emissions trajectory (SSP2-4.5), we find that we are already committed to peak warming greater than 1.5°C with 42% probability, increasing to 66% by 2029 (340 $GtCO_2$ relative to 2021). Probability of peak warming greater than 2.0°C is currently 2%, increasing to 66% by 2057 (1550 $GtCO_2$ relative to 2021). Because climate will cool from peak warming as GHGs concentrations decline, committed warming of 1.5°C in 2100 won't occur with at least 66% probability until 2055.

2.1 Introduction

The Paris Agreement has affirmed an international goal to hold global warming to well below 2°C and to pursue efforts to limit it to 1.5°C relative to pre-industrial temperatures. However, global warming is projected to exceed 1.5°C within decades, and 2°C by mid-century in all but the lowest emission scenarios (Lee et al., 2021). That is, there is limited time and allowable carbon dioxide (CO_2) emissions (i.e., a remaining carbon budget) be-

fore these temperature thresholds are exceeded. Assessing the possibility of avoiding these global warming levels requires a clear understanding of the unrealized warming that is inevitable due to past emissions (a geophysical warming commitment), treated separately from the warming associated with future, and therefore theoretically avoidable, emissions (a socioeconomic warming commitment).

Here we provide a quantification of the geophysical warming commitment and its evolution over time in terms of the zero emissions commitment (ZEC) [°C], a common metric used to estimate the global temperature change that follows an abrupt cessation of emissions. The magnitude of the ZEC depends on the evolution of atmospheric greenhouse gas and aerosol concentrations after emissions cease, along with the multiple timescales of climate response to changes in radiative forcing. If only CO_2 emissions cease, global temperature is expected to remain relatively constant as both ocean heat uptake and atmospheric CO_2 forcing slowly decline by similar, and compensating, amounts (Solomon et al., 2009; Armour and Roe, 2011; Ehlert and Zickfeld, 2017; Goodwin et al., 2015; Williams et al., 2017). Estimates of the ZEC following a cessation of only CO_2 emissions (referred to here as ZEC_{CO_2}) range from slight cooling to continued warming (Williams et al., 2017; Frölicher et al., 2014) over multiple centuries, depending upon model representations of ocean heat uptake, carbon cycle, climate feedbacks and historical emissions pathways (Ehlert and Zickfeld, 2017; Williams et al., 2017; MacDougall et al., 2020; Winton et al., 2010; Zhou et al., 2021). On average, ZEC_{CO_2} is taken to be small throughout the 21st century when estimated from multi-model simulations (Lee et al., 2021; MacDougall et al., 2020). This suggests that future warming is primarily governed by future emissions rather than by past emissions, and thus society is not geophysically-committed to exceeding key global warming levels prior to reaching them.

However, the situation becomes more complex when the emissions of short-lived climate forcers, including non-CO_2 greenhouse gases (GHGs) and aerosols, are considered (Hare and Meinshausen, 2006; Armour and Roe, 2011; Mauritsen and Pincus, 2017). Tropospheric aerosols produced through the combustion of fossil fuels and biomass burning have atmospheric lifetimes of days to weeks and currently exert a strong net cooling effect on the climate (a negative radiative forcing). Thus, the ZEC associated with the cessation

of all anthropogenic emissions (referred to here as ZEC_{anthro}) would include warming associated with the rapid reduction of aerosols and consequent 'unmasking' of a portion of GHG forcing. This warming is offset in small part by the removal of black carbon on snow (a positive surface albedo forcing) and in larger part by a decrease in tropospheric ozone, nitrous oxide and methane concentrations over the following weeks to decades, followed by a slower decline as GHG concentrations decrease until the global temperature stabilizes at a value determined by the residual forcing associated with the portion of anthropogenic CO_2 that remains in the atmosphere for millennia (Armour and Roe, 2011; Mauritsen and Pincus, 2017; Smith et al., 2019).

We thus focus on two measures of the climate commitment following a complete cessation of anthropogenic emissions: the peak temperature reached in the decades following emissions cessation (ZEC^{peak}_{anthro}) and the eventual temperature reached in the year 2100 (ZEC^{2100}_{anthro}). These two measures represent different aspects of committed warming that may be relevant to different components of the climate system and impacts thereupon; i.e., systems that respond quickly to global temperature change would be sensitive to peak warming (e.g., sea ice, the hydrological cycle, hurricanes, agriculture, and many ecosystems), while those that respond slowly to global temperature change would be sensitive to long-term warming (e.g., glaciers, ice sheets, and sea level).

Both measures of commitment (ZEC^{peak}_{anthro} and ZEC^{2100}_{anthro}) depend on the magnitude and evolution of GHG and aerosol radiative forcing following emissions cessation, the sensitivity of climate to forcing changes (often characterized in terms of the equilibrium climate sensitivity (ECS) [°C]), and the timescales of climate adjustment associated with the oceans (Armour and Roe, 2011; Smith et al., 2019). Cessation of emissions from present-day levels generally results in a ZEC^{peak}_{anthro} of a few tenths of a degree Celsius above the current temperature, with an overshoot lasting approximately a decade before cooling to near-present temperatures (Smith et al., 2019; Allen et al., 2018; Matthews and Zickfeld, 2012). However, a larger ZEC^{peak}_{anthro} with a more prolonged overshoot is possible if aerosol forcing is strong and climate sensitivity is high (Armour and Roe, 2011; Matthews and Zickfeld, 2012). Thus, a full accounting of past emissions suggests that society may be geophysically-committed to peak warming exceeding key global warming levels many years before those levels are

reached – absent efforts to directly remove CO_2 from the atmosphere.

Recent research has substantially advanced scientific understanding of the instrumental record of global warming (Chen et al., 2021), Earth's energy imbalance (von Schuckmann et al., 2020; Forster et al., 2021), aerosol radiative forcing (Bellouin et al., 2020; Forster et al., 2021) and climate sensitivity (Sherwood et al., 2020; Forster et al., 2021). In light of these advances, the current geophysical climate commitment needs to be revisited. Furthermore, both ZEC^{peak}_{anthro} and ZEC^{2100}_{anthro} will change over time as GHG emissions continue and the blend of radiative forcing agents in the atmosphere evolves. We ask, when will the world be geophysically committed to reaching key global warming levels, such as 1.5 and 2.0°C, either temporarily (overshoot) or at the end-of-century, and how do these estimates depend upon the emissions trajectory?

2.2 Committed warming as a function of time

We quantify both ZEC^{peak}_{anthro} and ZEC^{2100}_{anthro} associated with a cessation of all anthropogenic emissions using an emissions-based climate model, FaIR (Finite Amplitude Impulse Response Model, v1.3) (Smith et al., 2018; Millar et al., 2017) with model parameters constrained by observations of global energy budget and temperature trends since the 1800s (Methods). FaIR produces effective radiative forcing from emissions time-series of 39 gases and short-lived climate forcers, with an intermediate concentration calculation for GHGs and a four-timescale carbon-cycle representation that is sensitive to changes in uptake efficiency with cumulative emissions and temperature. Changes in land-use forcing are excluded from this analysis because it is unclear how they should be represented in the ZEC framework (e.g., Jones et al., 2019). Global temperature is calculated using a two-layer ocean model (Held et al., 2010; Geoffroy et al., 2013) (Methods) which was also used for the global temperature projection assessment in the IPCC's Sixth Assessment Report (IPCC AR6) (Lee et al., 2021).

Priors for key model parameters, including the radiative feedback parameter (which governs ECS), the efficiency of ocean heat uptake, ocean effective heat capacities, the magnitude of GHG and aerosol forcing, and carbon cycle parameters are generated to match distributions of state-of the-art global climate models (Geoffroy et al., 2013) and IPCC

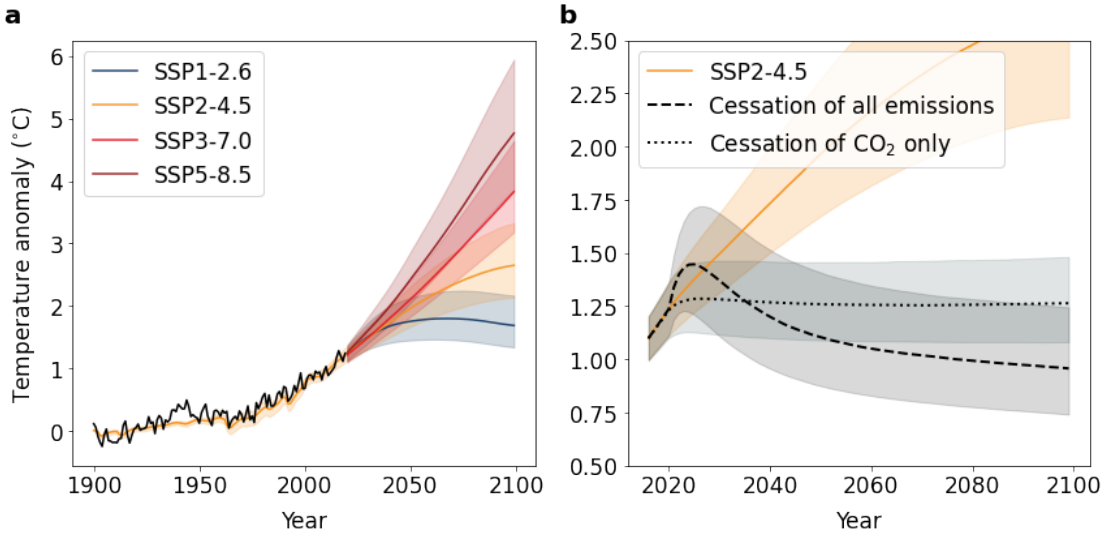

Figure 2.1: Constrained FaIR ensemble global temperature projections. a) Global warming following Shared Socioeconomic Pathways (SSPs) with the historical temperature record from HadCRUT5 Morice et al. (2012) overlaid in black. b) SSP2-4.5 with no cessation of emissions (orange line), a cessation of only CO_2 emissions (dotted line, ZEC_{CO_2}) and of all anthropogenic emissions (dashed line, ZEC_{anthro}) in the beginning of 2021. Shading represents the 66% confidence interval obtained from a 6729 posterior member ensemble (Methods). Global temperature anomalies are taken relative to the 1850-1900 average.

AR6 estimates (Forster et al., 2021; Smith et al., 2021) (Methods; Extended Data Figs. 2.4 to 2.7). Posterior model parameter distributions are then selected based on fits to observational records of global surface temperature, global energy accumulation and radiative forcing since 1850, as well as present-day CO_2 levels. These constraints result in a posterior FaIR model ensemble that accurately fits the historical temperature record to within an estimate of internal temperature variability (Extended Data Fig. 2.8), and closely matches the projections of 21st century warming as assessed by IPCC AR6 (Lee et al., 2021) (Fig. 2.1a).

Posterior estimates of ECS and the transient climate response (TCR) are 2.9°C [1.8-4.7°C, 5-95% confidence] and 1.7°C [1.2-2.5°C], respectively. Median aerosol forcing is estimated to be -1.2 W m^{-2} [-1.8 to -0.6 W m^{-2}] in 2018 relative to 1765. These values are all in good agreement with recent assessments based on multiple lines of evidence (Sherwood et al., 2020; Bellouin et al., 2020) including IPCC AR6 (Forster et al., 2021).

With the posterior FaIR ensemble, we first evaluate ZEC^{peak}_{anthro} and ZEC^{2100}_{anthro} associated with an abrupt cessation of anthropogenic emissions near the present day (taken as January 2021) (Fig. 2.1b). We find a median ZEC^{peak}_{anthro} of 0.22°C relative to 2020, with an overshoot that lasts for approximately 18 years before eventually cooling to several tenths of a degree Celsius below 2020 temperatures by the end-of-century (Fig. 2.1b, dashed line). Smith et al. (2019), also using FaIR, estimated a median ZEC^{peak}_{anthro} of approximately 0.1°C above 2018, while Matthews and Zickfeld (2012), using an intermediate complexity model, found median peak warming of 0.3 °C following a cessation of all emissions. This difference in results is due in large part to differences in aerosol forcing at the time of emissions cessation between Smith et al. (2019) (-1.4 to -0.2 W m^{-2}, 90% confidence range), Matthews and Zickfeld (2012) (-1.9 to -0.8 W m^{-2}), and this study (-1.8 to -0.6 W m^{-2}), as well as larger climate sensitivity in Matthews and Zickfeld (2012).

Similar to Smith et al. (2019), we find net cooling at the end-of-century following emissions cessation (a median ZEC^{2100}_{anthro} of -0.4°C below the 2020 temperature), which is in contrast to the end-of-century warming of approximately 0.3°C found in a previous study (Mauritsen and Pincus, 2017) – a difference that may be due to different assumptions about residual GHG and non-CO_2 forcing in the ZEC experiment, and the sensitivity of atmospheric CO_2 uptake to global temperatures (Smith et al., 2019).

The 2018 IPCC Special Report on global warming of 1.5°C concluded that past emissions alone are unlikely (less than 33% probability) to raise global temperature above 1.5°C relative to 1850-1900 (Allen et al., 2018). We find that there is now a 42% probability that the world is committed to peak global warming (ZEC^{peak}_{anthro}) of at least 1.5°C based on past emissions alone, and a 2% probability that ZEC^{peak}_{anthro} reaches at least 2.0°C (Fig. 2.1b). For sustained warming of greater than 1.5°C and 2.0°C at the end-of-century (ZEC^{2100}_{anthro}), the probabilities are 5% and 0%, respectively, meaning that society is not yet committed to these levels of long-term warming.

For comparison, we find that a cessation of CO_2 emissions (ZEC_{CO_2}), while holding all other forcings fixed at present-day levels, results in temperatures remaining within approximately 0.1°C of the present-day temperature throughout the century (Fig. 2.1b, dotted line), consistent with previous studies (Armour and Roe, 2011; Mauritsen and Pincus, 2017; Mac-

Dougall et al., 2020). The end-of-century ZEC_{CO_2} is approximately 0°C [-0.02 to 0.12°C, 66% confidence] relative to present-day temperatures, in good agreement with the AR6 assessed likely range of 0°C ±0.19°C.

We next consider how ZEC^{peak}_{anthro} and ZEC^{2100}_{anthro} change over time following a range of emissions pathways prior to cessation, as illustrated by eight Shared Socioeconomic Pathway (SSP) emission scenarios: SSP1-1.9, SSP1-2.6, SSP4-3.4, SSP2-4.5, SSP4-6.0, SSP3-7.0-lowNTCF ('Near Term Climate Forcing'), SSP3-7.0, and SSP5-8.5 (Riahi et al., 2017). We conduct simulations of the climate response to a cessation of anthropogenic emissions within FaIR in every year for the period 2021-2080 or until CO_2 emissions reach net-zero, following each of these SSP scenarios, each run with 6,729 posterior ensemble members (Methods). Fig. 2.2a shows ZEC^{peak}_{anthro} and ZEC^{2100}_{anthro} relative to the pre-industrial period 1850-1900 as a function of the year in which emissions cease along a moderate mitigation scenario (SSP2-4.5) (solid black and dashed black lines, respectively). A key result is that the time at which ZEC^{peak}_{anthro} is reached occurs from four to seven years before that temperature would be exceeded following SSP2-4.5 (horizontal distance between orange and solid black lines and shading in Fig. 2.2a); while there is a 66% probability of *exceeding* 1.5°C by 2035, there is a 66% probability of being *committed* to at least 1.5°C of warming by 2029 (ZEC^{peak}_{anthro} in Fig. 2.2a; Table 2.1). For 2°C, this becomes 2061 and 2057, respectively (ZEC^{peak}_{anthro} in Fig. 2.2a; Table 2.1). The number of years that ZEC^{peak}_{anthro} is reached before a given warming level is exceeded depends on the probability threshold considered, with the 17^{th} percentile of the ensemble (corresponding to high aerosol forcing and high climate sensitivity) producing a larger difference, and the 83^{rd} percentile of the ensemble (corresponding to low aerosol forcing and low climate sensitivity) producing a smaller difference (Table 2.1).

A similar assessment can be made for ZEC^{2100}_{anthro}, for which temperature thresholds are surpassed after the thresholds themselves are reached in the emissions scenario. We find that end-of-century warming commitments of 1.5 and 2.0°C are reached by 2055 and 2061 with 66% probability – 15 and 16 years after those temperatures are reached, respectively, when following SSP2-4.5 (Fig. 2.2a). Since global temperature in 2100 after a cessation of emissions is relatively stable compared to peak warming, this implies that society is not committed to long-term warming of a given magnitude prior to when that temperature is

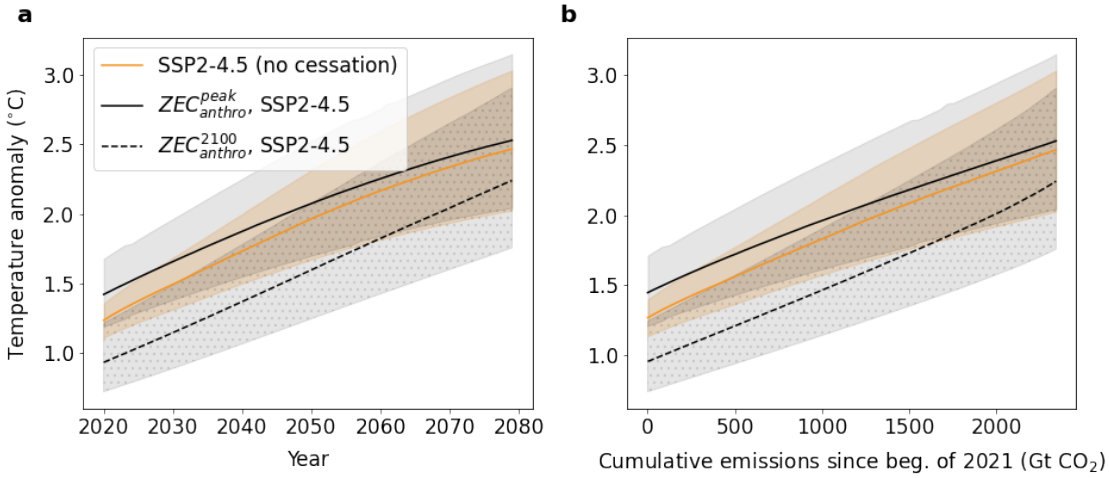

Figure 2.2: Committed warming and scenario warming following SSP2-4.5. FaIR ensemble temperature projections assuming no cessation of emissions (orange line) and warming commitments, $\mathrm{ZEC}^{\mathrm{peak}}_{\mathrm{anthro}}$ (solid black line) and $\mathrm{ZEC}^{2100}_{\mathrm{anthro}}$ (dashed black line), as functions of emissions cessation year (a) and cumulative anthropogenic CO_2 emissions since the beginning of 2021 (b). For SSP2-4.5 in (a), the x-axis is 'Year'. Shading indicates the 66% confidence interval. Global temperature anomalies are taken relative to the 1850-1900 average.

reached following an emissions trajectory.

Considering the seven other emissions scenarios, results show that committed warming of 1.5 and 2°C ($\mathrm{ZEC}^{\mathrm{peak}}_{\mathrm{anthro}}$) occurs roughly half a decade before those temperatures would actually be exceeded if emissions were never halted (Fig. 2.3a,c,e; Table 2.1). The choice of emissions pathway becomes increasingly important with time, with high and very high emissions scenarios (SSP3-7.0, SSP5-8.5) generating a $\mathrm{ZEC}^{\mathrm{peak}}_{\mathrm{anthro}}$ of 2°C earlier than lower emissions scenarios. Conversely, only high mitigation (SSP1-1.9, SSP1-2.6) avoids $\mathrm{ZEC}^{\mathrm{peak}}_{\mathrm{anthro}}$ of 2°C over this century in the 66$^{\mathrm{th}}$ percentile. A $\mathrm{ZEC}^{2100}_{\mathrm{anthro}}$ exceeding 1.5°C and 2.0°C following a cessation of emissions in this century is avoided in low (SSP1-2.6) and in low to moderate (SSP4-3.4, SSP2-4.5) emissions scenarios, respectively.

The elevated warming following a cessation of emissions in 2021 (temperature overshoot) lasts 11-48 years (66% confidence range). The length of the temperature overshoot generally declines with aerosol forcing, and is therefore dependent upon the emissions trajectory; by

Table 2.1: Year in which a cessation of anthropogenic emissions leads to ZEC^{peak}_{anthro} and ZEC^{2100}_{anthro} of 1.5, 1.7 and 2°C following SSP2-4.5 at the 17th, 50th, 66th, and 83rd percent confidence levels. 'No cessation' refers to the year in which these temperatures are reached following the emissions scenario without a cessation of emissions. 'A/R' indicates that the temperature commitment has already been reached at that probability level as of the beginning of 2021, while 'N/R' indicates that the commitment is not reached at that probability level within the bounds of the experiment (up to year 2080).

Global warming since 1850-1900 (°C)	Temperature metric	Commitment year by ensemble percentile			
		17th	50th	66th	83rd
1.5	ZEC^{peak}_{anthro}	A/R	2024	2029	2037
	ZEC^{2100}_{anthro}	2031	2046	2055	2065
	No cessation	2024	2031	2035	2040
1.7	ZEC^{peak}_{anthro}	A/R	2032	2040	2050
	ZEC^{2100}_{anthro}	2038	2055	2064	2076
	No cessation	2031	2039	2044	2052
2.0	ZEC^{peak}_{anthro}	2032	2047	2057	2074
	ZEC^{2100}_{anthro}	2048	2068	N/R	N/R
	No cessation	2040	2052	2061	2077

2060, a cessation of all emissions along medium-to-high aerosol forcing scenarios (SSP3-7.0, SSP4-6.0; Fig. 2.9) results in 6-31 year overshoots, while low aerosol forcing scenarios (SSP1-1.9, SSP1-2.6), result in 3-10 year overshoots (66% confidence range).

2.3 Committed warming as a function of cumulative emissions

The projected 21st century warming following different SSP emissions scenarios (Fig. 2.3a) simplifies greatly when cast in terms of the cumulative CO_2 emissions (Fig. 2.3b; calculated as cumulative anthropogenic CO_2 emitted since January 2021). Consistent with previous studies (Allen et al., 2009; Matthews et al., 2009; MacDougall and Friedlingstein, 2015),

global warming is nearly proportional to cumulative CO_2 emissions, with small differences between scenarios arising from the assumed rate of emissions and the fractional contribution of non-CO_2 climate forcing to total forcing. A relevant measure of this proportionality is the Transient Climate Response to Emissions (TCRE), defined as the global temperature change per 1000 $GtCO_2$ emitted. We find that the constrained FaIR ensemble has TCRE = 0.44°C per 1000 $GtCO_2$ [0.33-0.59°C per 1000 $GtCO_2$, 66% confidence range] when calculated for SSP2-4.5 for the period 2018-2068. These estimates are in line with Matthews et al.'s (2020) estimate of 0.44°C per 1000 $GtCO_2$ [0.32-0.62 °C per 1000 $GtCO_2$, 90% range] and the IPCC AR6 (Canadell et al., 2021) estimate of 0.45°C per 1000 $GtCO_2$ [0.27-0.63 °C per 1000 $GtCO_2$, 66% range].

We next evaluate how ZEC^{peak}_{anthro} and ZEC^{2100}_{anthro} scale with the cumulative CO_2 emitted until the year emissions cease. The evolution of ZEC^{peak}_{anthro} is nearly proportional to cumulative CO_2 emissions (Fig. 2.3b), despite its dependence on aerosol forcing at the time emissions cease. This is likely due to the approximately constant fraction of aerosol forcing relative to total forcing over time for most individual SSP pathways. Exceptions are SSP1-2.6 and SSP1-1.9, wherein aerosols decrease rapidly during the first half of the 21st century and decline more slowly thereafter (Extended Data Fig. 2.9), resulting in a non-linear response in peak warming as a function of emissions cessation year. The proportionality with cumulative CO_2 emissions is more evident for ZEC^{2100}_{anthro}, which is independent of the emissions scenario (Fig. 2.3c) because the residual CO_2 forcing dominates total forcing by 2100 following a cessation of emissions.

The proportionality of committed warming to cumulative CO_2 emissions permits the quantification of a remaining carbon budget for committed warming of 1.5, 1.7, and 2°C (Table 2.2). Total cumulative carbon emitted between 1850 and 2019 is approximately 2,290 $GtCO_2$, within the IPCC AR6 estimate of 2,390 +/- 240 $GtCO_2$ for the same period (Canadell et al., 2021). A median ZEC^{peak}_{anthro} of 1.5°C is reached after the emission of 120 $GtCO_2$ [0-340 $GtCO_2$, 66% confidence] relative to the beginning of 2021 (Fig. 2.2b); for 2°C the remaining carbon budget is 1,120 $GtCO_2$ [470-1,550 $GtCO_2$]. At the end-of-century (ZEC^{2100}_{anthro}), 1.5°C is reached after the emission of 1,080 $GtCO_2$ [420-1,470 $GtCO_2$]; for 2°C this remaining carbon budget is 1,980 $GtCO_2$ [1,170-not reached within the experiments].

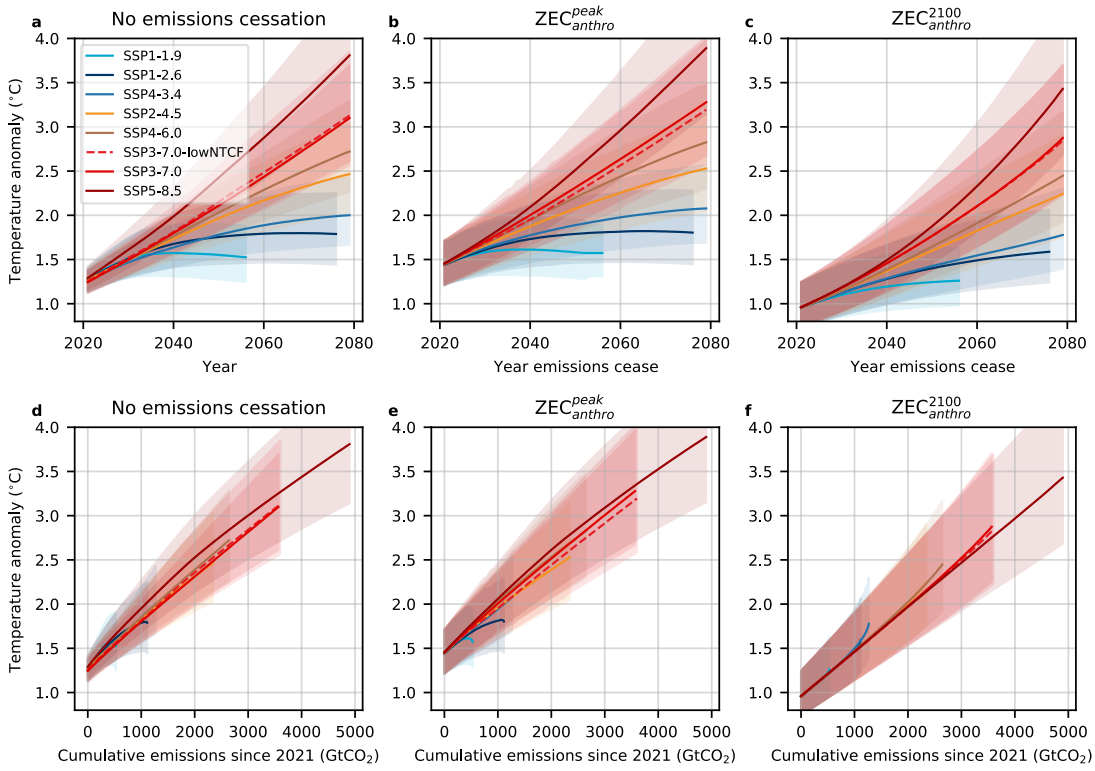

Figure 2.3: Committed warming and scenario warming relative to 1850-1900 for all SSPs. Temperature response following each SSP with no cessation of emissions as a function of year (a); $\mathrm{ZEC}^{\mathrm{peak}}_{\mathrm{anthro}}$ (b) and $\mathrm{ZEC}^{2100}_{\mathrm{anthro}}$ (c) as a function of shut-off year until 2080 or when emissions reach net-zero. d-f are as in a-c, but as functions of cumulative emissions since the beginning of 2021. Note that a, b, and c correspond to the orange, solid black and dashed black lines presented in Fig. 2.2, respectively, but for all SSPs. Shading represents the 66% confidence interval.

Uncertainty in the remaining carbon budgets stems mainly from uncertainties in aerosol forcing and climate sensitivity. However, the results are consistent across the emissions scenarios – a key to maintaining consistency in the calculation of carbon budgets (Matthews et al., 2020).

Remaining carbon budgets estimated using the ZEC can be contrasted to those estimated following emissions pathways without a cessation of emissions (Table 2.2). 1.5°C is exceeded with 66% probability when cumulative emissions since 2021 reach 600 $\mathrm{GtCO_2}$ following SSP2-4.5 (orange line in Fig. 2.2b), a measure of the 'threshold exceedance budget'

(Canadell et al., 2021). This is substantially larger than the 66$^{\text{th}}$ percentile estimate of 340 $GtCO_2$ using ZEC^{peak}_{anthro} because it does not account for the additional warming that would occur as aerosol forcing is reduced upon abrupt cessation of emissions. The smaller carbon budgets obtained using ZEC^{peak}_{anthro} would provide an underestimate for emissions pathways that achieve net-zero CO_2 through the implementation of carbon dioxide removal technologies while maintaining some level of anthropogenic aerosol emissions. However, compared to scenarios that phase out emissions more slowly and without net-negative CO_2, ZEC^{peak}_{anthro} provides the smallest estimate of peak warming over the 21$^{\text{st}}$ century, and therefore can be considered a lower bound on committed warming (Extended Data Fig. 2.10).

Table 2.2: Estimated remaining carbon budget ($GtCO_2$) relative to the beginning of 2021 for ZEC^{peak}_{anthro} and ZEC^{2100}_{anthro} of 1.5, 1.7 and 2°C following SSP2-4.5 at the 17$^{\text{th}}$, 50$^{\text{th}}$, 66$^{\text{th}}$, and 83$^{\text{rd}}$ percent confidence levels. 'No cessation' and 'N/R' are as in Table 2.1.

Global warming since 1850-1900 (°C)	Temperature metric	Estimated remaining carbon budget			
		17$^{\text{th}}$	50$^{\text{th}}$	66$^{\text{th}}$	83$^{\text{rd}}$
1.5	ZEC^{peak}_{anthro}	0	120	340	680
	ZEC^{2100}_{anthro}	420	1080	1470	1870
	No cessation	120	420	600	820
1.7	ZEC^{peak}_{anthro}	0	470	820	1260
	ZEC^{2100}_{anthro}	730	1470	1830	2250
	No cessation	420	770	990	1340
2.0	ZEC^{peak}_{anthro}	470	1120	1550	2190
	ZEC^{2100}_{anthro}	1170	1980	N/R	N/R
	No cessation	820	1340	1720	2280

These calculations are relatively pathway-independent across priority SSPs, and are therefore robust to choice of emissions trajectory. As such, they do not require an examina-

tion of only a subset of emissions trajectories that are calibrated to avoid 1.5 or 2°C (such as those presented in IPCC AR6), or that are constrained by socioeconomic feasibility (Allen et al., 2018; Rogelj et al., 2019). This methodology is appropriate when considering the possibility of a temperature overshoot that may persist for over a decade, with subsequent impacts on human and natural systems that respond quickly, and perhaps irreversibly, to global warming.

Two important insights are that: (i) the world will have a greater than 66% probability of being committed to peak warming above 1.5°C by 2027-2032 in all emissions scenarios, and 2°C by 2043-2057 in medium to high emissions scenarios (SSP2-4.5 to SSP5-8.5), and (ii) these temperature commitments will occur 4 to 6 years before the 1.5 and 2°C warming levels will actually be exceeded, assuming emissions follow SSP2-4.5. We find that the 1.5 and 2.0°C peak warming commitments (ZEC^{peak}_{anthro}) correspond to median carbon budgets of approximately 120 and 1,120 Gt CO_2 relative to the beginning of 2021, respectively. Given that FaIR does not capture the possibility of future destabilizing climate feedbacks such as decreased ice sheet cover (Goosse et al., 2018), thawing permafrost and methane hydrate dissociation due to ocean warming (MacDougall, 2021; Ruppel and Kessler, 2017), or a sea-surface temperature pattern effect that allows for a more substantial shift toward destabilizing cloud feedbacks in the future than modeled here (Andrews et al., 2018; Silvers et al., 2018; Zhou et al., 2016, 2017, 2021), these estimates of the timing of geophysical warming commitments may become underestimates as global temperatures rise.

2.4 Methods

Model.

We use FaIR v1.3.6 (Smith et al., 2018) for all historical and future climate simulations. Historical simulations are run using the Reduced-Complexity Model Intercomparison Project (RCMIP)-generated SSP emissions time-series for the period 1765-2016; future scenarios are run for SSP1-1.9, SSP1-2.6, SSP4-3.4, SSP2-4.5, SSP4-6.0, SSP3-7.0-lowNTCF, SSP3-7.0, and SSP5-8.5 for the period 2016-2100, with an abrupt cessation of all anthropogenic emissions in every year along each pathway until 2080 or until CO_2 emissions reach net

zero; CO_2 emissions are set to zero while all other emissions are set to pre-industrial (1765) levels in order to retain background sources. Background emissions of N_2O and CH_4 for the historical period and into the future are prescribed using the default time-series in FaIR, where emissions vary over the historical period but are constant from 2005 onwards as a proxy for natural sources.

Forcing associated with land-use change is not included over the historical record or in future projections due to the lack of a dynamic vegetation model and its overestimation in FaIR relative to AR6 estimates (Forster et al., 2021). Land-use change associated with the zero emissions commitment was also not modeled in intermediate complexity models participating in ZECMIP (Jones et al., 2019). Volcanic and solar forcing are not included in future emissions scenarios in order to isolate anthropogenic warming. Volcanic forcing for the historical period is scaled by a factor of 0.6 in order to obtain better agreement with historical aerosol forcing and global temperatures (similar scaling-down of volcanic efficacy has previously been performed in the MAGICC simple climate model for better correspondence to observed temperatures (Meinshausen et al., 2011)).

We modify FaIR to use the Held et al. (Held et al., 2010) two-layer energy balance model (EBM) to calculate global temperatures from radiative forcing. The equations for this EBM are:

$$C\frac{dT}{dt} = F + \lambda T - \epsilon\gamma(T - T_0)$$

$$C_0\frac{dT_0}{dt} = \gamma(T - T_0)$$

where C and C_0 are, respectively, the heat capacities of the first layer (representing the surface components of the climate system including the atmosphere, land, sea ice, and ocean mixed layer) and second layer (representing the deep ocean); γ is the coefficient of heat exchange between the two layers, representing a measure of the ocean heat uptake efficiency; λ is the radiative feedback parameter; and ϵ is a deep ocean efficacy factor that expresses the time dependence of the global radiative feedback (see Held et al. (2010), Geoffroy et al. (2013)). The equilibrium climate sensitivity is given by

$$ECS = -\frac{F_2 x}{\lambda}$$

where F_{2x} is the forcing for CO_2 doubling. Retaining the Held formulation of energy balance in FaIR allows us to diagnose heat uptake, account for feedback time dependence, and model feedback parameters estimated from global climate models (GCMs) (Geoffroy et al., 2013).

Ensemble development.

A 300,000 member FaIR ensemble is generated by drawing random values from prior probability distributions of ECS (uniform from 1 to 6°C), ocean model variables, and carbon cycle parameters. Normal prior distributions of γ, C and C_0 are generated using distributions from GCMs (Geoffroy et al., 2013), but with standard deviations (σ) expanded by 50%; the distribution in γ is truncated to avoid values less than 0.1, while C_0 is truncated to avoid sampling deep ocean heat capacities less than 10 W m^{-2} °C^{-1} yr (γ: mean = 0.67 W m^{-2} °C^{-1}, σ = 0.225 W m^{-2} °C^{-1}; C: mean = 8.2 W m^{-2} °C^{-1} yr, σ = 1.4 W m^{-2} °C^{-1} yr; C_0: mean = 124.7 W m^{-2} °C^{-1} yr, σ = 65.8 W m^{-2} °C^{-1} yr). A lognormal prior distribution for ϵ is generated using distributions from GCMs (Geoffroy et al., 2013) (mean = 1.28, σ = 0.375), with values of ϵ above unity reflecting the fact that the effective climate sensitivity is expected to become larger in the future as the geographic pattern of warming changes on timescales of multiple centuries (Forster et al., 2021; Andrews et al., 2015; Dong et al., 2019, 2020).

We scale GHG forcing due to CO_2, CH_4, and N_2O in every year by a constant amount generated from normal distributions that match the updated IPCC AR6 "very likely" range (90% confidence interval) of radiative forcing over the industrial period (1750-2018; CO_2: mean = 2.15 W m^{-2}, σ = 0.16 W m^{-2}; CH_4: mean = 0.54 W m^{-2}, σ = 0.07 W m^{-2}; N_2O: mean = 0.19 W m^{-2}, σ = 0.02 W m^{-2}). Aerosol forcing is also scaled by a constant amount by values drawn from a uniform distribution ranging from -2.2 to -0.1 W m^{-2} in order to adequately sample the full range of possible forcing values. All other gases and short-lived climate forcers (SLCFs) are treated using default parameterizations in FaIR (not scaled).

Uncertainty in FaIR carbon cycle parameters associated with various uptake processes is treated as in Smith et al. (2018; 2019). Because FaIR has no representation of internal variablity, $\mathrm{ZEC}^{\mathrm{peak}}_{\mathrm{anthro}}$ and $\mathrm{ZEC}^{2100}_{\mathrm{anthro}}$ are quantified based on annual mean temperature

values.

Constraining the model.

Following the methods of Armour (2017), a Bayesian framework is used to constrain model outputs to observational estimates of global mean sea surface temperature (T), ocean heat uptake (Q), and radiative forcing (F) for the 2006-2019 mean relative to the 1850-1900 baseline, reducing the model ensemble to 6,729 members. Specifically, only ensemble members that satisfy the condition:

$$\sqrt{\left(\frac{\delta T}{\sigma T}\right)^2 + \left(\frac{\delta Q}{\sigma Q}\right)^2 + \left(\frac{\delta N}{\sigma N}\right)^2} < 1.65$$

are kept, where δT, δQ and δF are the differences between the model-derived estimates of global surface temperature, ocean heat uptake and total radiative forcing anomalies (2006-2019 mean relative to the 1850-1900 baseline) and observational estimates, with σ_T, σ_Q and σ_N representing one standard deviation of the mean for each of these values, and 1.65 corresponding to the 90% confidence level. Observational values are taken from the IPCC AR6: $\Delta T_{obs} = 1.03 \pm 0.2$°C, $\Delta Q_{obs} = 0.59 \pm 0.35$ W m^{-2} and $\Delta N_{obs} = 2.20 \pm 0.7$ W m^{-2} (Forster et al., 2021). Modeled CO_2 concentrations are additionally constrained to be within $\pm$ 2 ppm of the 2006-2018 mean (395.98 ppm) (NOAA, 2020).

This method produces a posterior estimate on the equilibrium climate sensitivity of 2.9°C [1.8-4.7°C], which is consistent with the most recent estimate of 2.3-4.7°C provided by Sherwood et al. (2020) and 2-5°C as assessed in IPCC AR6. Posterior estimates of aerosol forcing and the remaining four free parameters in the two-layer ocean model (γ, ϵ, C and C_0) are shown in Extended Data Figs. 2.4 to 2.7). However, the observational record is not long enough to adequately constrain ϵ owing to the slow adjustment of the deep ocean (the timescale on which the value of ϵ becomes relevant for surface warming). The posterior distribution of ϵ used in this study is thus the same as the prior (Extended Data Fig. 2.5c); however, the choice of prior distribution in ϵ does not significantly affect the conclusions presented here.

2.5 Extended Data

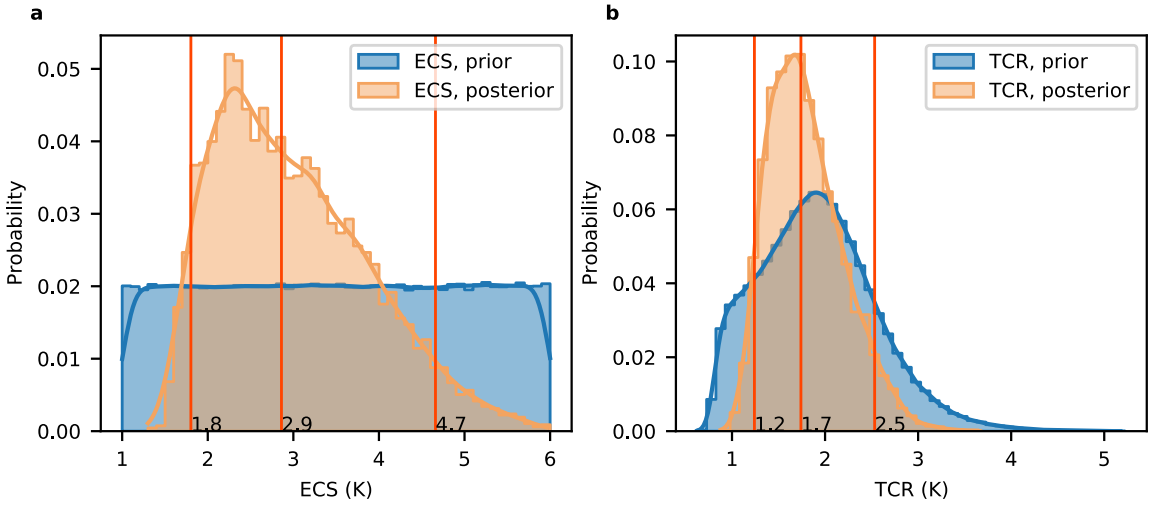

Figure 2.4: Posterior estimates of ECS (a) and TCR (b) are 2.9°C [1.8-4.7°C, 90% confidence] and 1.7°C [1.2-2.5°C], respectively.

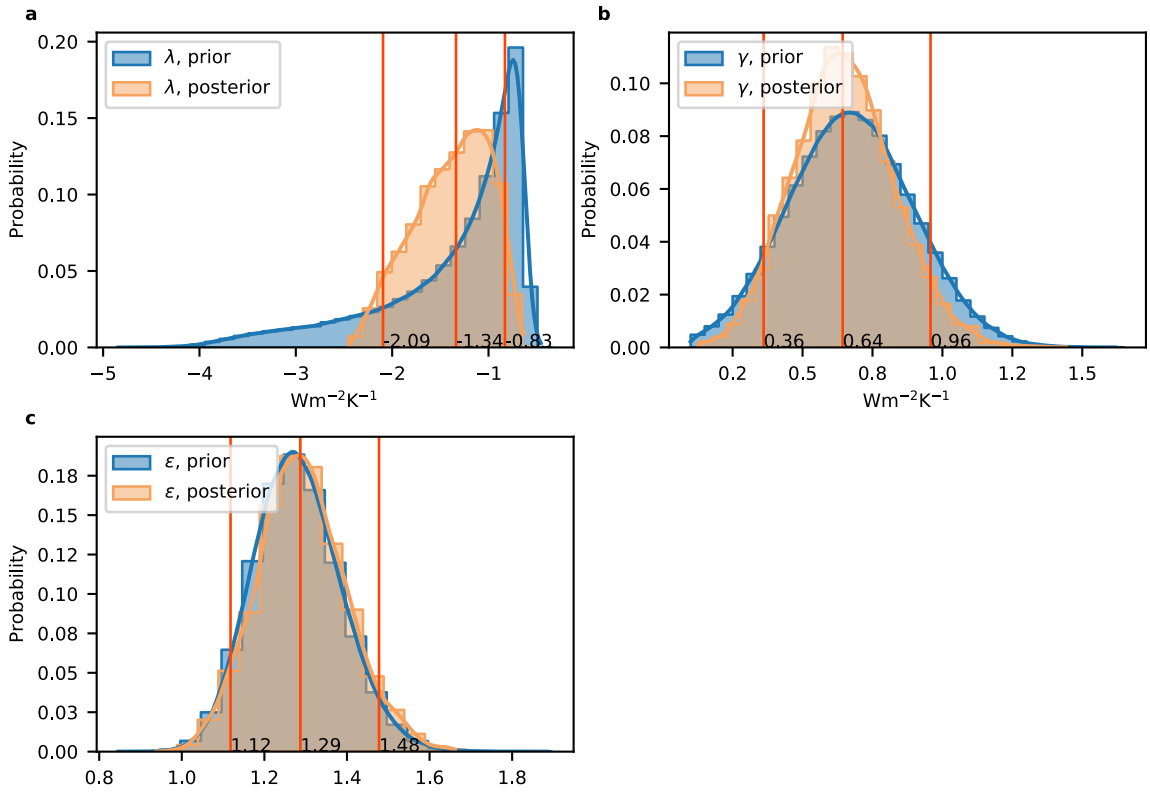

Figure 2.5: The global radiative feedback parameter, λ (a), ocean heat exchange coefficient, γ (b), and deep ocean efficacy factor, ϵ (e). Note that neither γ nor ϵ are well constrained by the observational record.

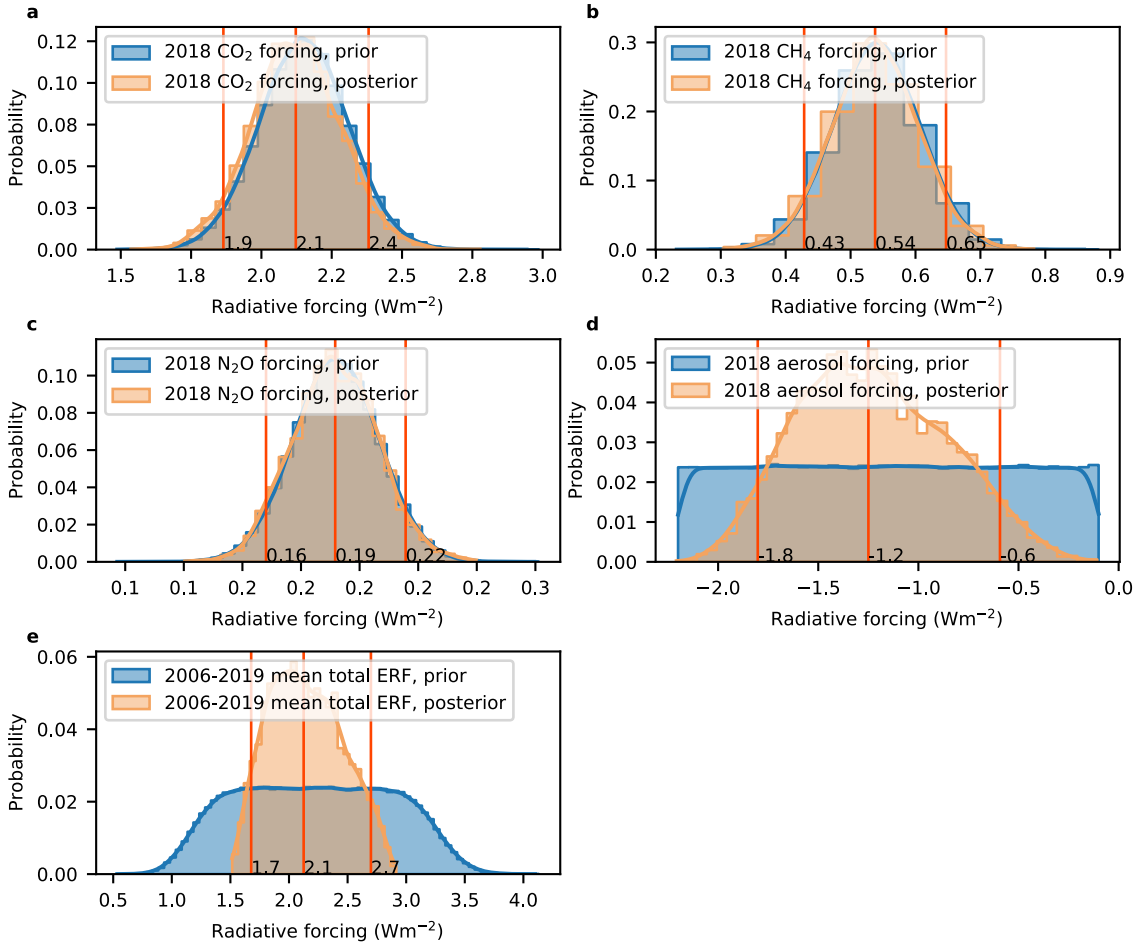

Figure 2.6: CO_2 (a), CH_4 (b), N_2O (c), and aerosol (d) forcing in 2018 relative to 1765. Total ERF (e) is the 2006-2019 mean relative to the 1850-1900 average. Note that the posterior median total ERF of 2.1 W m^{-2} corresponds well with the observational value of 2.2 W m^{-2}, $\sigma = 0.43$ W m^{-2}. Median aerosol forcing agrees well with the AR6 estimate of -1.1 W m^{-2} [-2.0 to -0.4 W m^{-2}] for the same period.

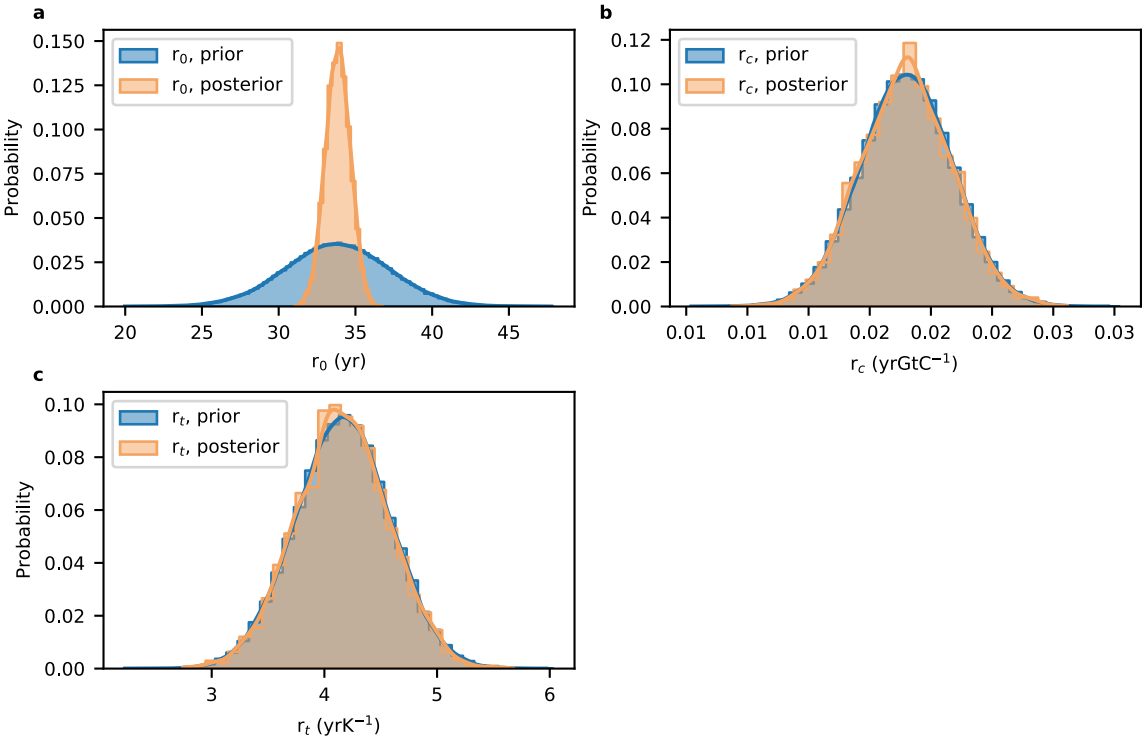

Figure 2.7: R_0 (a) represents the airborne fraction of CO2 during the preindustrial, and r_t (b) and r_c (c) capture the decreasing absorption efficacy of land and ocean carbon sinks with rising global temperatures and CO2 concentrations, respectively. Note that r_c and r_t are not well-constrained by the observational record. The posterior mean r_0 is 33.8 years, which is between that of Millar et al.'s (2017) value of 32.4 years, and Smith et al.'s (2018) value of 35 years.

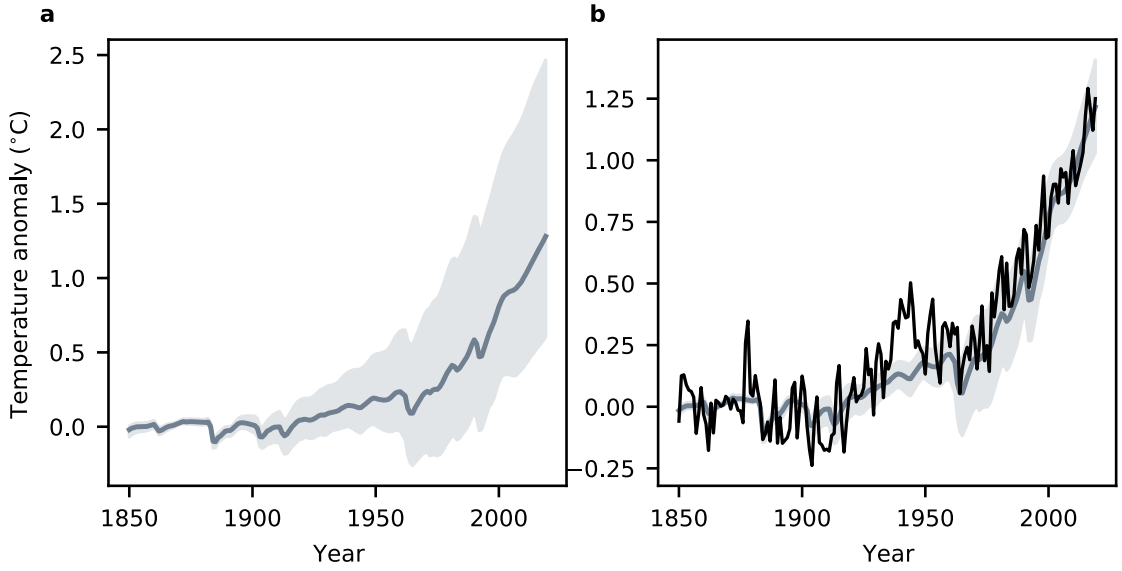

Figure 2.8: Prior (300,000 member) (a) and posterior (6,729) (b) modeled global temperatures. The observed temperature (overlaid in black) is the ensemble mean from the HadCRUT5 blended air and sea surface temperature dataset (Morice et al., 2012). Shading represents the 90% confidence interval.

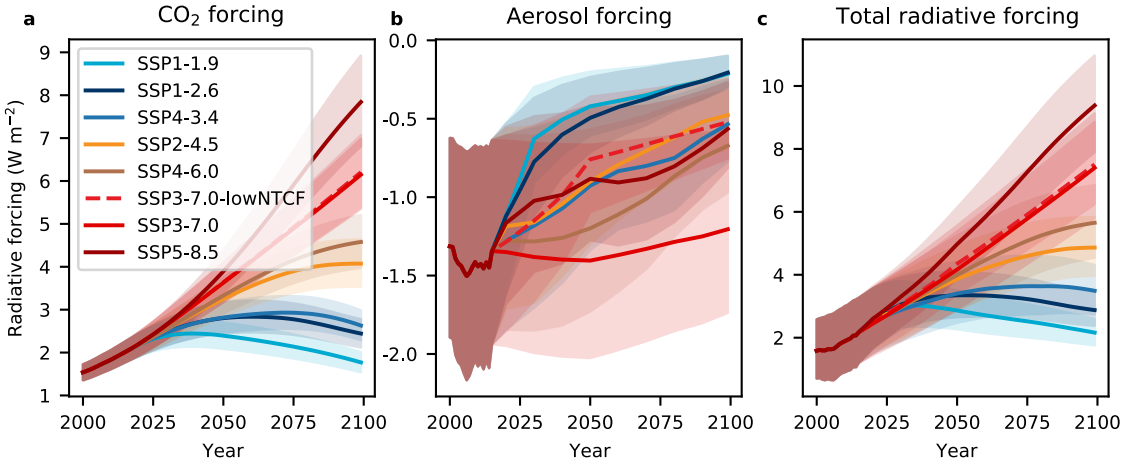

Figure 2.9: CO_2 (a), Aerosol (b), and total (c) radiative forcing. Shading represents the 90% confidence interval.

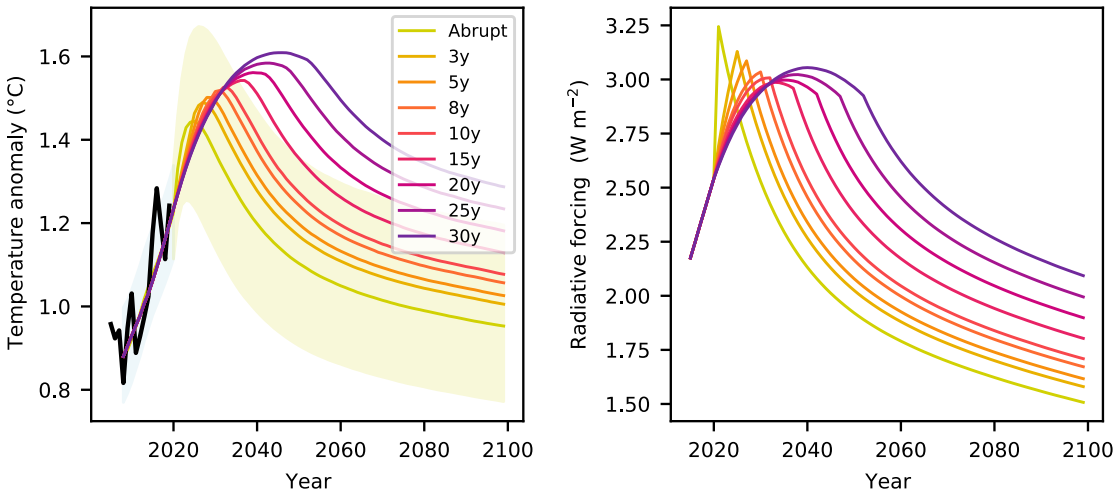

Figure 2.10: Modeled global temperature anomaly relative to 1850-1900 (a) and total radiative forcing relative to 1765 (b) for a phase-out of anthropogenic emissions as compared to the abrupt cessation shown in the main text ('abrupt') following SSP2-4.5. Legend indicates the number of years over which the phase-out occurred, beginning in 2021, where emissions of all gases decrease linearly to zero (GHGs) and to 1765 levels (all other gases), with no net-negative CO_2 emissions.

Chapter 3

MID-PLIOCENE CLIMATE FORCING, SEA SURFACE TEMPERATURE PATTERNS, AND IMPLICATIONS FOR MODERN-DAY CLIMATE SENSITIVITY

This chapter is published as: Dvorak, M., Armour, K.C., Feng, R., Cooper, V.T., Zhu, J., Burls, N. and C. Proistosescu. Mid-Pliocene climate forcing, sea surface temperature patterns, and implications for modern-day climate sensitivity. *Journal of Climate*, **38**, 3037–3053 (2025). https://doi.org/10.1175/JCLI-D-24-0410.1.

Abstract

Characterized by similar-to-today CO_2 levels (∼400ppm) and surface temperatures approximately 3-4°C warmer than the preindustrial, the mid-Pliocene Warm Period (mPWP) has often been used as an analog for modern CO_2-driven climate change, and as a constraint on the equilibrium climate sensitivity (ECS). However, model intercomparison studies suggest that non-CO_2 boundary conditions – such as changes in ice sheets – contribute substantially to the higher global mean temperatures and strongly shape the pattern of sea surface warming during the mPWP. Here, we employ a set of CESM2 simulations to quantify mPWP effective radiative forcings, study the role of ocean circulation changes in shaping the patterns of sea surface temperatures, and calculate radiative feedbacks during the mPWP. We find that the non-CO_2 boundary conditions of the mPWP, enhanced by changes in ocean circulation, contributed to larger high-latitude warming and less-stabilizing feedbacks relative to those induced by CO_2 alone. Accounting for differences in feedbacks between the mPWP and the modern (greenhouse-gas driven) climate provides stronger constraints on the high-end of modern-day ECS. However, a quantification of the forcing of non-CO_2 boundary condition changes combined with the distinct radiative feedbacks that they induce suggests that Earth System Sensitivity may be higher than previously estimated.

3.1 Introduction

The mid-Pliocene warm period (mPWP, ∼3.3–3.0 Mya) – also referred to as the mid-Piacenzian (Dowsett et al., 2016) – was an interval in Earth's history characterized by similar-to-today concentrations of atmospheric CO_2 (∼400ppm; Martínez-Botí et al., 2015) but with global average temperatures approximately 3–4°C warmer than the preindustrial (Sherwood et al., 2020; Forster et al., 2021; Annan et al., 2024; Tierney et al., 2025). The potential for anthropogenic greenhouse gas emissions to drive global warming to similar levels has contributed to the use of this period as an analog for climate change over the 21st century (Burke et al., 2018; Tierney et al., 2020; Burton et al., 2023). It has also been used as a constraint on the equilibrium climate sensitivity (ECS) – a key metric of the long-term global temperature response to CO_2 forcing (e.g., Sherwood et al., 2020; Forster et al., 2021).

However, coupled global climate model simulations from the recent Pliocene Model Intercomparison Project phase 2 (PlioMIP2; Haywood et al., 2016) suggest that a significant fraction of the surface warming during the mPWP may have been driven by paleoenvironmental boundary conditions rather than CO_2 forcing (Lunt et al., 2012; Haywood et al., 2020; Baatsen et al., 2021; Feng et al., 2020). These include topographic anomalies resulting from reduced ice sheet extent over Greenland and Antarctica (the latter resulting in an ice-free, oceanized West Antarctica) and exposure of the Bering Strait land bridge, Arctic Archipelagic and Sunda and Sahul continental shelves in Indonesia (Fig. 3.1), along with major changes in vegetation type and extent (Haywood et al., 2016). In simulations carried out using the US National Science Foundation National Center for Atmospheric Research's (NSF NCAR's) fully coupled Community Earth System Model, version 2 (CESM2; Danabasoglu et al., 2020), this set of paleoenvironmental boundary conditions, with no greenhouse gas changes relative to the preindustrial, lead to globally-averaged surface warming of 2.9°C – more than half of the 5.1°C mPWP warming in the model (Feng et al., 2020).

That more than half of the warming of the mPWP was driven by boundary condition changes implies that care must be taken when using reconstructions of this period as an analog for greenhouse-gas driven near-term warming. The standard method of inferring

climate sensitivity to CO_2 from these reconstructions is by treating these slow changes as forcings, rather than as feedbacks (e.g., Sherwood et al., 2020; PALEOSENS, 2012). In doing so, it has been assumed that the climate's sensitivity to changes in CO_2 and boundary conditions are similar; i.e., that all forcings produce the same amount of global warming per unit forcing.

However, recent studies of the Last Glacial Maximum (LGM) have shown that more of the cooling at the LGM came from non-CO_2 forcings (specifically land ice sheet changes) than previously recognized (Zhu and Poulsen, 2021) and, thus, that ECS and near-future, greenhouse-gas driven warming can be constrained to be a lower value (Cooper et al. 2024). The mechanism by which this occurs is known as the pattern effect (Armour et al., 2013; Andrews et al., 2015; Stevens et al., 2016), whereby radiative feedbacks (mainly associated with cloud responses) depend on the spatial pattern of sea surface temperatures (SSTs) (e.g., Dong et al., 2019; Zhou et al., 2017). Because ice sheet changes occur at high latitudes, the warming or cooling they induce also primarily occurs at high latitudes, where radiative feedbacks are relatively more positive (amplifying) (Stuecker et al., 2018). This leads to a larger global temperature response than that induced by an equivalent amount of CO_2 forcing, which peaks in the tropics and is more spatially uniform (Smith et al., 2020; Bonan et al., 2018).

Does a similar SST pattern effect on radiative feedbacks need to be accounted for when constraining ECS and future warming using reconstructions of the mPWP? To answer this question, we need a quantitative understanding of the drivers of mPWP warmth, and of the radiative feedbacks induced by CO_2 and boundary condition changes in particular. Previous studies have examined the large-scale effects of these boundary conditions on the mPWP climate with fully coupled simulations in which paleogeography, vegetation, ice sheets, and CO_2 are modified individually (Lunt et al., 2021, 2010; Chandan and Peltier, 2018; Feng et al., 2017; Haywood et al., 2016; Feng et al., 2022). The global climate response to paleogeographic changes (including continental topography and ocean bathymetry) are thought to be relatively small (Feng et al., 2017), while changes in vegetation and ice sheets are thought to contribute substantially to mPWP warmth (Chandan and Peltier, 2017; Weiffenbach et al., 2023). Here we build on these findings by performing CESM2 simulations

that allow us to calculate the effective radiative forcing (ERF; Forster et al., 2021, 2016) associated with mPWP CO_2 and boundary conditions. With these ERFs quantified, we are then able to calculate the radiative feedbacks induced by these changes separately, and determine whether the climate's sensitivity to mPWP forcings is different from its sensitivity to CO_2 doubling alone (which defines ECS). We also perform mixed-layer ("slab") ocean CESM2 simulations with the same set of mPWP forcings to assess the role of ocean circulation in shaping the SST patterns that give rise to radiative feedback differences. The results have direct implications for how the mPWP can be used to constrain ECS and future warming.

We use a set of models in the CESM2 family to quantify and understand the forcings and feedbacks shaping the mPWP climate, similar in spirit to the methodology used by Zhu and Poulsen (2021) for the LGM. In what follows, we describe the models used (Section 3.2), provide a novel estimate of mPWP ERFs (Section 3.3), investigate the role of ocean circulation in shaping mPWP SST patterns (Section 3.4), and quantify radiative feedbacks under mPWP forcings (Section 3.5). Finally, we discuss the implications of our results for estimates of modern-day ECS – of relevance for near-term warming – and for the Earth System Sensitivity governing warming in the distant future (Section 3.6).

3.2 Overview of models and approach

We carry out a suite of simulations using CESM2.1 in atmosphere-only, slab ocean, and fully coupled configurations. CESM2 is a coupled atmosphere-land-ocean-sea ice global climate model with 32 vertical levels in the atmosphere and 60 vertical levels in the oceans. In all simulations, the model incorporates the Community Atmosphere Model version 6.0 (CAM6), Community Land Model version 5.0 (CLM5), Community Ice Code (CICE) version 5, and the Parallel Ocean Program (POP) version 2. All simulations are carried out with atmosphere and land models resolved at 0.9° latitude $\times$ 1.25° longitude. Fully-coupled simulations of the preindustrial control and CO_2 forcing simulations were performed with ocean and sea ice components resolved on a 384×320 curvilinear mesh grid; mPWP simulations were performed with an expanded grid of 394×320 to resolve dynamic processes in the oceanized West Antarctica (Feng et al., 2020).

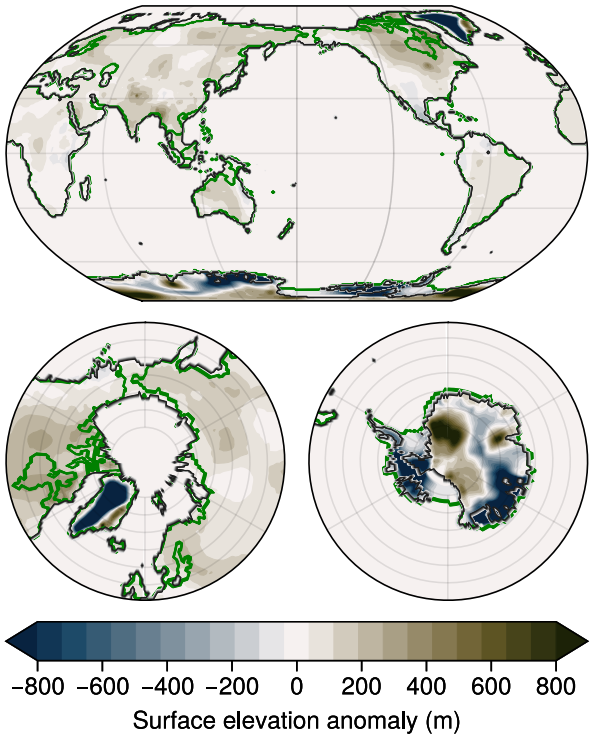

Figure 3.1: PRISM4 topographic land-sea mask used as input to CESM2 mPWP simulations (Dowsett et al., 2016). Ice sheet changes are shown as surface elevation anomalies with respect to preindustrial ice sheet height. Preindustrial coastlines are shown in green while mPWP coastlines are shown in black.

All mPWP simulations employ a set of paleoenvironmental boundary conditions developed through the most recent phase of the Pliocene Research, Interpretation and Synoptic Mapping project 4 (PRISM4) (Dowsett et al., 2016). These include global reconstructions of the land-sea mask, vegetation type and extent, soil and lake distributions, continental topography, ocean bathymetry, and ice sheet height and extent (Fig. 3.1). We refer to this set of features hereafter as simply "boundary conditions." CO_2 concentrations are set to 400ppm, while all other greenhouse gases and aerosol emissions are set to preindustrial levels, as these are not well constrained by paleoclimate reconstructions. Orbital parameters are set to those of 3.205 Ma, which is the same as the preindustrial (Haywood et al., 2016).

We make use of existing fully coupled model (FCM) CESM2 simulations that were performed as part of the PlioMIP2 project (Feng et al., 2020; Table 3.1). These are: a

preindustrial (PI) control simulation with CO_2 at 284.7ppm (FCM-PI, 2000 years long); a mPWP simulation complete with mPWP-level CO_2 at 400ppm and boundary conditions (FCM-mPWP, 1200 years long); a mPWP boundary condition-only simulation with PI-level CO_2 of 284.7ppm (FCM-BC, 400 years long); and a simulation with PI control boundary conditions but mPWP-level CO_2 of 400 ppm (FCM-CO_2, 900 years long) (Table 3.1). These simulations were run with dynamical phenology while plant functional types were prescribed separately for mPWP and PI. Simulations using PI boundary conditions were initialized from the end of the 1200 year PI control simulation performed for the Coupled Model Intercomparison Project phase 6 (CMIP6; Eyring et al., 2016).

Model initialization from a warm ocean state was used to efficiently achieve quasi-equilibrium in FCM-mPWP (Feng et al., 2020). All simulations have a global top-of-atmosphere radiation imbalance of ≤ 0.25 Wm^{-2} by the end of run-time (Table 3.1). The soil carbon reservoir (relevant for vegetation) was initialized to reach equilibrium by running standalone CLM5 with mPWP boundary conditions for 600 years (Feng et al., 2020) before carrying out the FCM-mPWP and FCM-BC simulations.

For comparison with CO_2-driven future climate change, we also make use of an existing 150-year-long simulation of CESM2, contributed to CMIP6, wherein CO_2 concentrations were abruptly doubled from PI levels (referred to here as FCM-2xCO_2). We extended this simulation for another 150 years in order to allow the model to come closer to equilibrium, permitting a more accurate estimate of the model value of ECS (e.g., Rugenstein and Armour, 2021) (Section 3.5), which is defined by the equilibrium surface warming under CO_2 doubling.

As noted above, within these fully coupled CESM2 simulations, boundary conditions alone account for over half of the total global mPWP surface warming (compare 2.9°C in FCM-BC to 5.1°C in FCM-mPWP – see Table 3.1). Meanwhile, mPWP CO_2 forcing alone accounts for less than half of mPWP warming (2.0°C in FCM-CO_2). Note that the simulated responses are relatively linear such that the sum of global temperature changes in FCM-CO_2 and FCM-BC (4.9°C) is nearly equal to the global temperature change in FCM-mPWP (5.1°C). There is substantial polar amplification of surface warming from boundary conditions when compared to CO_2 changes alone (Fig. 3.2b-c). When normalized

Table 3.1: Description of simulations used in this study. All values are taken as averages over the period of analysis unless otherwise noted, and anomalies are taken with respect to preindustrial control simulations.

Model set-up	Simulation long name	Simulation short name	Length (period of analysis) (years)	Global TOA radiation imbalance anomaly, ΔN (Wm^{-2})	Average global surface temperature anomaly, ΔT (°C)
Fully coupled	Preindustrial control	FCM-PI	2000 (100)	0.06	0.
	mid-Pliocene	FCM-mPWP	1200 (100)	0.25	5.10
	mid-Pliocene 284.7ppm CO_2	FCM-BC	400 (50)	0.03	2.85
	400ppm CO_2 only	FCM-CO_2	900 (90)	0.14	2.01
	2xCO_2 (569ppm)	FCM-2xCO_2	300 (250)*	0*	4.07*
Slab ocean	mid-Pliocene	SOM-mPWP	126 (50)	0.08	4.46
	mid-Pliocene 284.7ppm CO_2	SOM-BC	75 (50)	0.02	1.15
	400ppm CO_2 only	SOM-CO_2	84 (50)	-0.03	2.41
	2xCO_2 (569ppm)	SOM-2xCO_2	84 (50)	0.09	5.56
Atmosphere-only	mid-Pliocene	ATM-mPWP	30 (25)	3.40	0.46
	mid-Pliocene 284.7ppm CO_2	ATM-BC	35 (30)	1.34	0.31
	400ppm CO_2 only	ATM-CO_2	33 (28)	2.06	0.11
	2xCO_2 (569ppm)	ATM-2xCO_2	33 (28)	4.27	0.26

*Period of analysis here corresponds to a regression of ΔN on ΔT over years 100-300, with the equilibrium temperature extrapolated to $\Delta N = 0$ Wm^{-2}.

by the global mean sea surface temperature, a pattern of enhanced warming in the Southern Ocean, North Pacific Ocean, and North Atlantic Ocean is evident, especially in FCM-BC (Fig. 3.2d-f). These warming patterns also come along with strong reductions in low cloud cover (Fig. 3.2g-i), suggesting that cloud feedbacks may play a role in how mPWP boundary conditions influence global temperature.

To further probe the drivers of mPWP warmth within CESM2, we first quantify the ERF of mPWP boundary condition and CO_2 changes using atmosphere-only simulations, allowing us to determine the extent to which each contributes directly to mPWP warming. We then consider in greater detail the spatial patterns of warming induced by each forcing,

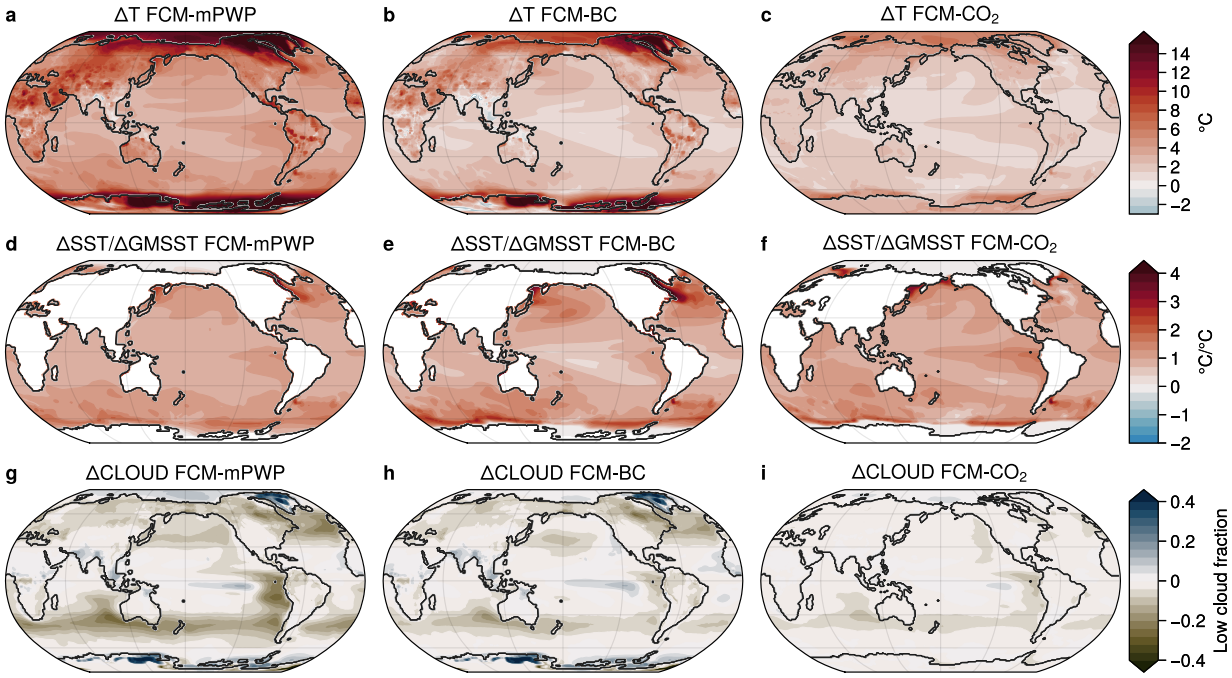

Figure 3.2: Surface air temperature (a-c), sea surface temperature normalized by global mean (d-f), and low cloud fraction (g-i) anomalies from preindustrial diagnosed from fully coupled CESM2 simulations of mid-Pliocene forcings (FCM-mPWP), changes in boundary conditions only (FCM-BC), and changes in CO_2 only (FCM-CO_2). All panels show anomalies relative to FCM-PI.

and quantify the contribution of slow ocean circulation changes to surface warming patterns by comparing the existing fully coupled model results to new slab ocean model simulations in which ocean heat transport cannot change. Finally, we use these simulations to quantify the radiative feedbacks that govern the climate's sensitivity to the different mPWP forcings and connect them to differences in warming patterns.

3.3 mPWP effective radiative forcing (ERF)

To calculate the ERF of mPWP forcings, we follow the now-standard approach (e.g., Hansen et al., 2005; Pincus et al., 2016) of performing simulations with an atmosphere-only model (CAM6, the atmospheric component of CESM2) in which SSTs and sea ice concentrations are prescribed to match the PI climatology while boundary conditions and CO_2 forcing are

imposed. We refer to these as fixed-SST simulations.

We employ a forcing-feedback framework consistent with the standard formulation of global energy balance:

$$\Delta N = \Delta F + \lambda \Delta T, \tag{3.1}$$

where ΔN is the global top-of-atmosphere radiation change from PI, ΔF is effective radiative forcing, ΔT is the global surface air temperature change from PI, and λ is the global radiative feedback (negative for a stable climate). Given ΔN, ERF can be estimated using equation (3.1) in the case where $\Delta T \approx 0$; i.e., the average global surface temperature is unchanged with respect to the PI control. In practice, the simulations show a small amount of global mean surface warming (δT) even with fixed SSTs and sea ice concentrations. The radiative response to this warming effectively reduces ΔN and biases the ERF estimate downward. We correct for this effect by using the common Hansen et al. (2005) adjustment:

$$\Delta F = \Delta F_{fSST} - \delta T_{fSST} \lambda \tag{3.2}$$

where λ is the net radiative feedback estimated from the fully coupled, abrupt CO_2-doubling simulation (FCM-2xCO_2). Note that equations (3.1)-(3.2) can also be applied to estimate shortwave (SW) and longwave (LW) components of ERF separately.

We perform five fixed-SST simulations with CAM6, denoted with ATM for atmosphere-only, corresponding to the five forcing scenarios described above for CESM2 (Table 3.1). We run each of these simulations for a minimum of 30 years, and exclude the first 6 years from the ERF analysis to allow for transient adjustment to the imposed forcings. In all fixed-SST simulations, sea surface temperatures and sea ice concentration are prescribed to match values derived from the climatology of CESM2's PI control simulations. In regions of West Antarctica where the absence of grounded and floating ice shelves in the mPWP (ATM-mPWP and ATM-BC) requires the introduction of new ocean grid cells (Fig. 3.1), SSTs are fixed to the freezing point of seawater (-1.8°C) and sea ice concentration is set to 100%. This choice maintains a realistic ocean surface albedo in the high Southern latitudes, where SSTs are cold enough to support sea ice but no PI sea ice exists (Supplementary Fig. 3.10).

Using our ATM-mPWP simulation and equations (3.1)-(3.2), we calculate a total ERF of the mPWP of 3.8 Wm^{-2}. This accounts for changes in CO_2, land-sea mask, ice sheets, vegetation, and topography between the mPWP and the PI. This total forcing can also be quantified in terms of its SW and LW components (Table 3.2). We find that the ERF of mPWP boundary conditions alone (ATM-BC) is 1.7 Wm^{-2}, while that of CO_2 (ATM-CO_2) is 2.2 Wm^{-2}. Once again, the simulated responses are relatively linear such that the sum of ERFs in ATM-CO_2 and ATM-BC (3.9 Wm^{-2}) is nearly equal to the ERF in ATM-mPWP (3.8 Wm^{-2}).

Table 3.2: Global average ERF and their SW and LW components.

	ΔN (Wm^{-2})	ΔF (after adjustment) (Wm^{-2})	ΔF (SW) (Wm^{-2})	ΔF (LW) (Wm^{-2})
ATM-mPWP	3.40	3.83	2.64	1.19
ATM-BC	1.34	1.65	2.28	−0.63
ATM-CO_2	2.06	2.17	0.58	1.59
ATM-2xCO_2	4.27	4.53	1.18	3.36

We find significant hemispheric asymmetry in the ERF of the mPWP, with strong, positive SW forcing in the northern high latitudes due to land surface albedo changes associated with the reduction of the Greenland ice sheet and increase in vegetation cover, extending from Siberia across the above-sea-level Bering Strait and North America (Fig. 3.3). The tropics are characterized by positive SW forcing associated with vegetation changes in subsaharan Africa, which is slightly offset by the enhanced LW emission to space from the warmer atmosphere.

We also find slight negative SW forcing in Indonesia where the exposure of the Sunda and Sahul shelves leads to an increase in surface albedo, and negative SW forcing over the eastern tropical Pacific Ocean in ATM-mPWP and ATM-BC – possibly due to a cloud response to a change in atmospheric column temperatures and moisture favoring an increase

in atmospheric stability. LW forcing is positive everywhere in ATM-CO_2 owing to higher CO_2 levels reducing outgoing LW radiation. Altogether, the total mPWP forcing is positive in most regions of the globe, except over some localized regions of the ocean, such as the eastern tropical Pacific and North Atlantic, and over Indonesia (Fig. 3.3).

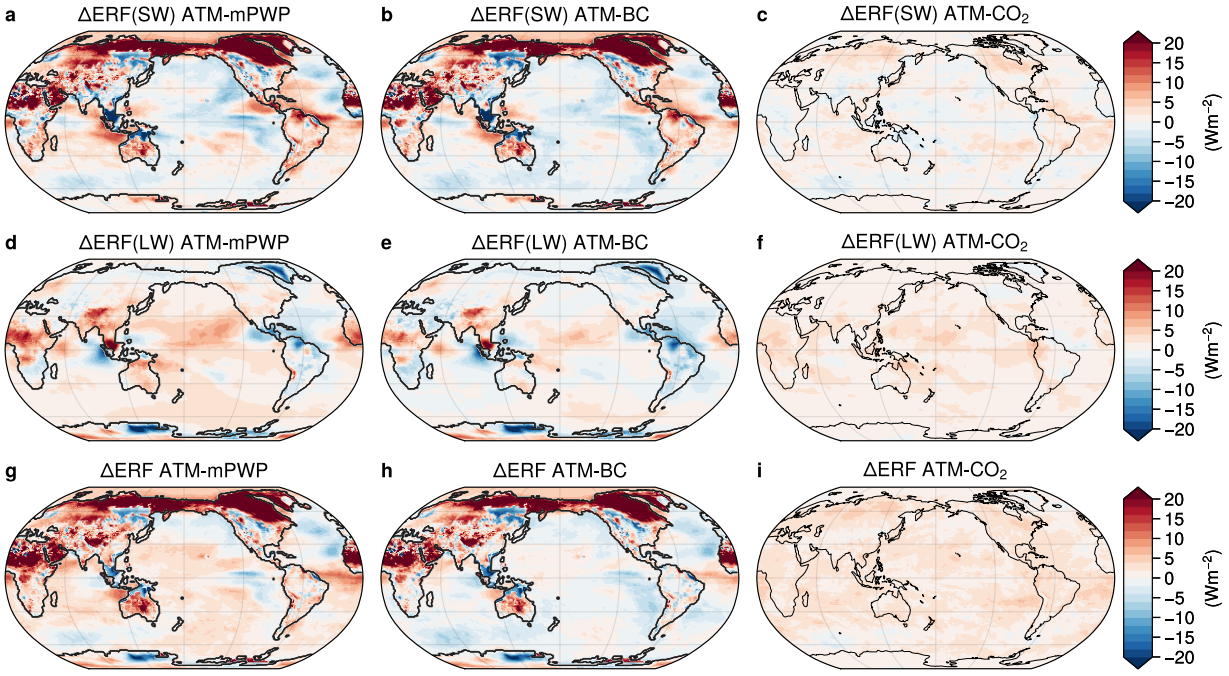

Figure 3.3: Shortwave (a-c), longwave (d-f), and total (g-i) effective radiative forcing (ERF) anomalies diagnosed from top-of-atmosphere radiative imbalances in fixed-SST atmosphere-only (CAM6) simulations. All figures show ERF after making the global mean Hansen et al. (2005) adjustment (equation 3.2).

PlioMIP studies have heretofore focused on estimating the global warming contributions of mPWP forcings through a suite of fully coupled simulations in which boundary conditions are imposed individually (Burton et al., 2023; Baatsen et al., 2021; Lunt et al., 2012, 2010), rather than on quantifying the ERF of these individual changes. CO_2 forcing of the mPWP has been estimated using existing CO_2-driven simulations (e.g., CO_2 doubling) under the assumption that CO_2 forcing scales logarithmically with concentration (Sherwood et al., 2020; Haywood et al., 2020; Feng et al., 2020). The explicit quantification of mPWP ERF, and its separation into contributions from boundary condition and CO_2 changes, presented

here, is the first to use fixed-SST simulations, which are necessary for accurate ERF estimation (e.g., Andrews et al., 2021; Zhu and Poulsen, 2021). This approach is consistent with the CMIP6 protocol for estimating ERF (Smith et al., 2020).

If boundary conditions and greenhouse gases affected global temperature in the same way, then each would induce warming in proportion to their fraction of the total mPWP ERF. The ERF from boundary condition changes in CESM2 is 1.7 Wm^{-2} (around 43% of the total mPWP forcing of 3.8 Wm^{-2}), while ERF from greenhouse gas changes in CESM2 is 2.2 Wm^{-2} (around 57% of the total mPWP forcing). However, we have shown that boundary condition changes alone contribute 55% of total mPWP warming in CESM2, while greenhouse gases contribute only 40% (with a remaining 5% coming from nonlinear interactions). While previous work has cast such differences in terms of varying forcing "efficacies" (e.g., Hansen et al., 2005; Zhu and Poulsen, 2020), more recent work has shown that this is more naturally explained by the different spatial patterns of radiative forcing and the feedbacks that are induced (e.g., Zhou et al., 2023; Cooper et al., 2024). In particular, CO_2 forcing is relatively spatially uniform with a maximum in the tropics, while boundary condition forcing is spatially variable with the largest positive forcing at high latitudes and with some regions of negative forcing in the tropics (Fig. 3.3); these differences give rise to distinct patterns of SST changes and feedbacks, and in turn to distinct global temperature responses. We examine these SST patterns in greater detail in the following section.

3.4 mPWP SST patterns and the role of ocean circulation changes

To better understand the respective contributions of CO_2 and boundary conditions to the mPWP global temperature response, we perform slab ocean simulations (CAM6 coupled to an ocean mixed layer of fixed depth) in which SSTs can change but ocean heat transport is fixed to that of CESM2's PI control simulation. By comparing the results of these simulations to the fully coupled CESM2 simulations described above (Fig. 3.2), we can evaluate the role of ocean heat transport changes in shaping the SST response.

Using the CAM6 slab ocean model (SOM), we perform the same suite of five simulations as for the fully coupled and atmosphere-only configurations described above (Table 3.1). We run the SOM simulations for a minimum of 70 years, with the average over the last ∼50

used for analysis to avoid transient spin-up in the first couple of decades. All simulations show a TOA radiative imbalance of < 0.1 Wm^{-2} at the end of run-time.

In each of these SOM simulations, mixed layer ocean heat flux convergence (Qflx) is prescribed to match that of the seasonally-varying, fully coupled CESM2 PI control climatology (e.g., Zhu and Poulsen, 2021). Analogous to the fixed-SST simulations described above, regions of ocean that are retained in the mPWP simulations are given the PI Qflx; in the region of new ocean grid cells of West Antarctica, where no PI Qflx exists, the Qflx is set to zero to reflect no ocean heat flux convergence in the PI control climatology (Supplementary Fig. 3.11). Nearest-neighbor interpolation is used to smooth the transition from zero Qflx to PI control values, and a small residual is distributed across all grid cells in order to maintain a globally-integrated Qflx of zero.

3.4.1 mPWP warming in the absence of ocean circulation changes

SOM-mPWP gives a globally-averaged surface warming of 4.5°C above the PI control, while SOM-BC and SOM-CO_2 give 1.2°C and 2.4°C of surface warming, respectively (Table 3.1). SOM-BC shows substantial Northern Hemisphere polar amplification, with warming over the North Pacific and North Atlantic Oceans and cooling over the tropical oceans; it also shows cooling over portions of the Southern Ocean (Fig. 3.4b,e). In contrast, SOM-CO_2 shows a much more spatially uniform SST response (Fig. 3.4c,f), which is expected from the more-uniform pattern of radiative forcing (Fig. 3.3i). Boundary conditions alone (SOM-BC) lead to less global warming per unit of forcing than does CO_2 alone (SOM-CO_2), and to much less warming than was seen in the corresponding fully coupled simulation (FCM-BC) despite identical boundary conditions (Table 3.3). The small amount of warming in SOM-BC, despite a large ERF, indicates a more-negative (stabilizing) global feedback in response to boundary conditions than to CO_2 forcing. This is consistent with the increase in low-cloud cover in the eastern tropical Pacific Ocean and lack of low-cloud cover loss in the Southern Ocean in the SOM-BC simulation (Fig. 3.4h), both of which act to reflect relatively more SW radiation than in the other simulations, resulting in less global warming.

The cause of these low-cloud cover changes in SOM-BC appears to be the cooling of the

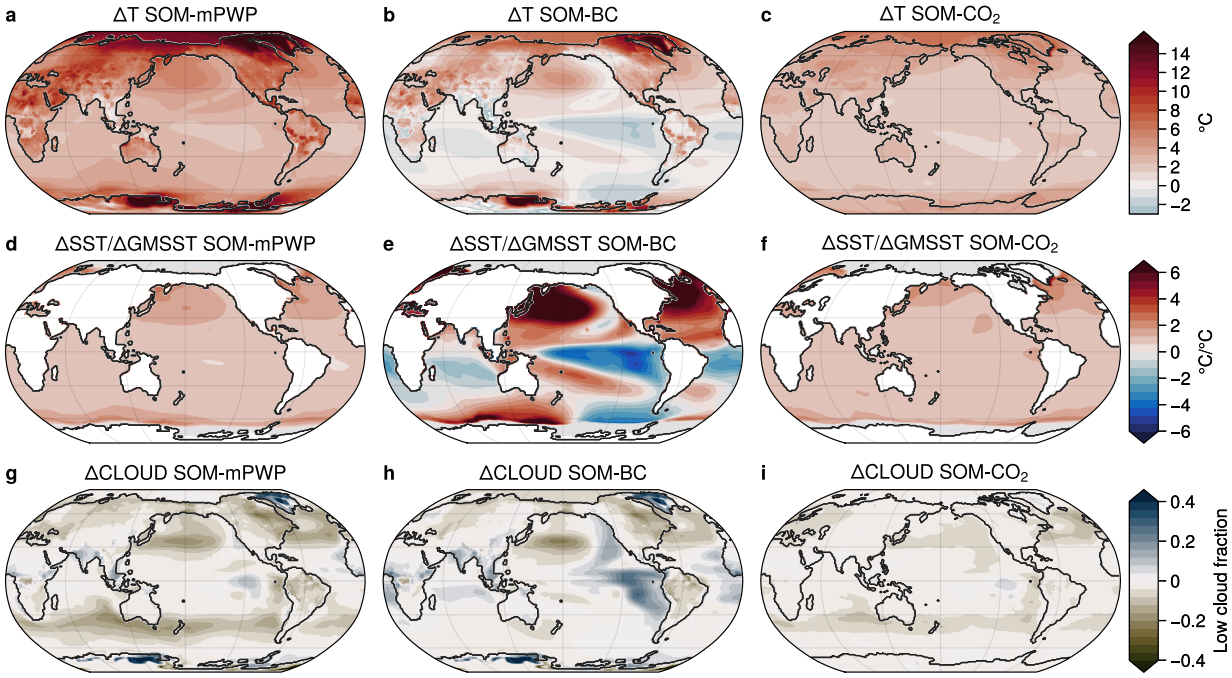

Figure 3.4: Surface air temperature (a-c), sea surface temperature normalized by global mean (d-f), and low cloud fraction (g-i) anomalies from preindustrial diagnosed slab ocean CESM2 simulations of mid-Pliocene forcings (SOM-mPWP), changes in boundary conditions only (SOM-BC), and changes in CO_2 only (SOM-CO_2).

Southern Ocean in response to West Antarctic ice sheet changes. The atmospheric response to a lowering of the ice sheet topography is a cyclonic wind anomaly that advects cold polar air and sea ice northward (Fig. 3.5), resulting in cooling of the Pacific sector of the Southern Ocean via a sea-ice-albedo feedback. These wind and SST anomaly patterns are consistent with those seen in a previous study of the response of slab ocean models to a lowering of West Antarctic topography (Steig et al., 2015).

The prominent surface cooling and low-cloud growth over the tropical east Pacific Ocean in SOM-BC is consistent with recent work demonstrating a southeast tropical Pacific cooling response to Southern Ocean cooling via an atmospheric teleconnection (Dong et al., 2022; Hartmann, 2022; Kim et al., 2022; Kang et al., 2023b), in which advection of Southern Ocean cold air anomalies toward the equatorial Pacific by climatological winds initiates cooling in the southeast Pacific, enhanced by a wind-evaporation-SST (WES) feedback

associated with a strengthening of southeasterly winds; in turn, surface cooling stabilizes the atmospheric boundary layer aloft, resulting in an increase in subtropical low-cloud cover that further amplifies surface cooling. We hypothesize that the same mechanism is at play here. This cooling of the Southern Hemisphere relative to the Northern also results in a large northward shift of the Intertropical Convergence Zone (ITCZ) in SOM-BC, which may further act to enhance southeast tropical Pacific cooling via a strengthening of the Hadley cell and an increase in surface winds. The negative SW ERF over the tropical Pacific Ocean in SOM-BC (Fig. 3.3b) may also contribute to tropical cooling, though this appears to be a secondary effect given that the same ERF is present in all mPWP boundary condition simulations (Fig. 3.3b) while tropical cooling only arises when the Southern Ocean cools as well (i.e., in SOM-BC).

The resulting increase in subtropical low-cloud cover and associated eastern Pacific cooling significantly reduces the global mean temperature response in SOM-BC. Interestingly, while the boundary condition and CO_2-driven ERFs were found to add linearly to the full mPWP ERF, globally-averaged temperature responses in the slab ocean simulations do not. This nonlinearity could arise from: (i) Southern Ocean sea ice loss under CO_2 forcing precluding a strong sea-ice-albedo feedback (and subsequent Southern Ocean cooling) in response to West Antarctic ice sheet changes in the absence of anomalous ocean heat transport; and (ii) asymmetries in the subtropical cloud response that have been shown to result in (locally) less-negative cloud feedbacks in areas of subtropical cooling as opposed to warming (Bloch-Johnson et al., 2024).

3.4.2 The role of ocean circulation changes in mPWP warmth

We now return to the fully coupled CESM2 simulations to assess how ocean circulation changes influence the magnitude and spatial pattern of warming in response to mPWP forcings. Total warming in FCM-mPWP is approximately 5.1°C, or an increase of 0.6°C over SOM-mPWP, while FCM-BC and FCM-CO_2 produce 1.6°C more, and 0.4°C less, warming than their SOM equivalents, respectively. This highlights an important role for ocean circulation changes in enhancing the global temperature response to mPWP boundary

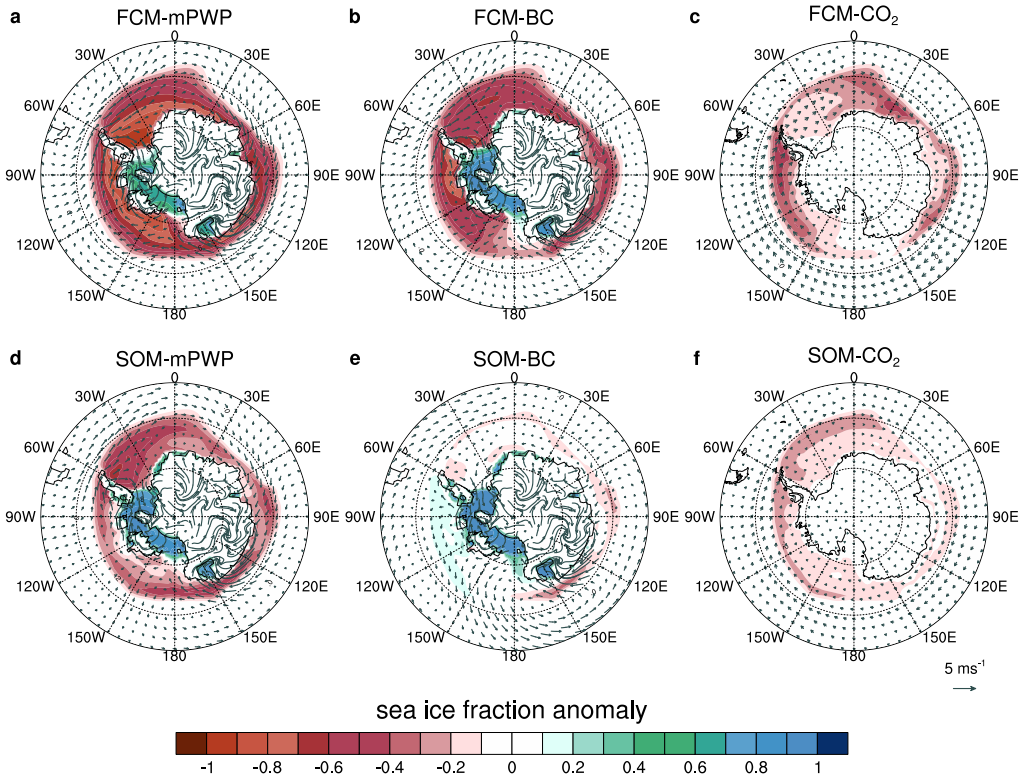

Figure 3.5: Southern Ocean sea ice fraction anomalies for fully coupled (a-c) and slab ocean (d-f) simulations, with surface wind anomalies indicated as vectors.

conditions.

We find that the Southern Ocean and eastern tropical Pacific cooling seen in SOM-BC does not arise in FCM-BC, despite identical boundary conditions (compare Fig. 3.4b and 3.2b). Instead, FCM-BC shows strong Southern Ocean warming, which then by the same atmospheric teleconnections discussed above acts to warm the eastern tropical Pacific, resulting in a strong loss of subtropical low-cloud cover and an amplification of the global warming response. FCM-BC shows only a small northward shift of the ITCZ (Supplementary Fig. 3.12) – in part due to a weak hemispheric warming contrast given strong Southern Ocean warming, and in part due to anomalous southward cross-equatorial ocean heat transport reducing the need for the ITCZ to move northward from energy balance arguments (e.g., Green and Marshall, 2017). Altogether, these differences result in much

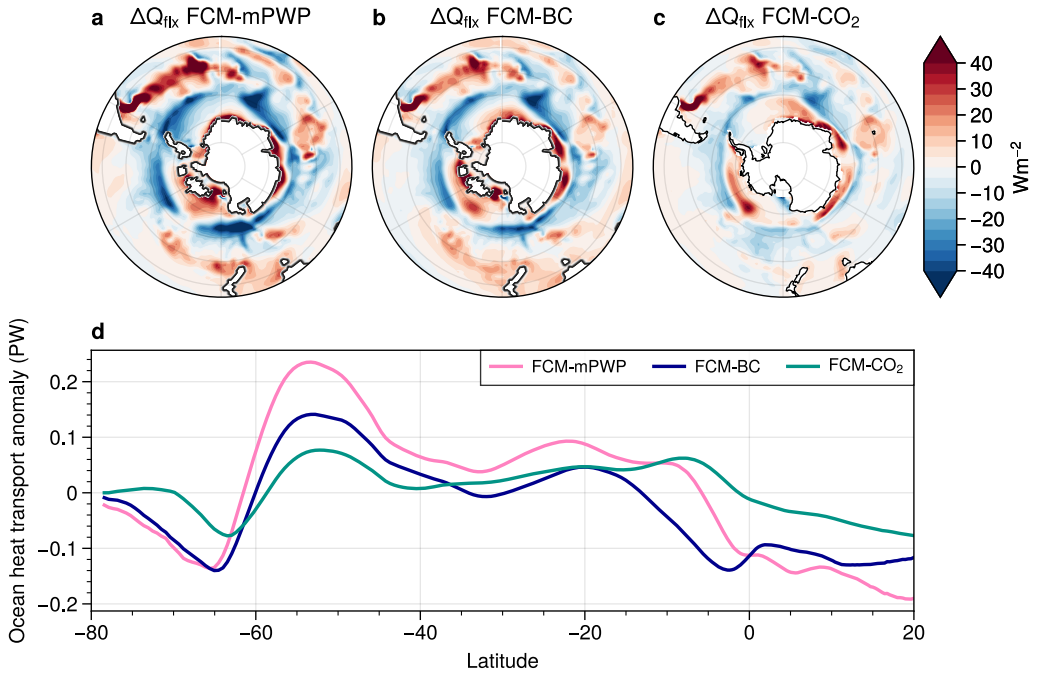

Figure 3.6: Southern Ocean heat flux convergence (Qflx) anomalies calculated from fully coupled simulations as the sum of the total surface heat flux and the internal latent heat of ice formation/melt into the mixed layer (a-c); zonal-average ocean heat transport anomalies from the same simulations (positive is northward) (d).

stronger warming of the eastern tropical Pacific in FCM-BC relative to SOM-BC.

Similar widespread warming of the Southern Ocean and tropical Pacific was also found by Steig et al. (2015) when using fully coupled models in which ocean circulation was allowed to adjust in response to a lowering of the West Antarctic ice sheet. Steig et al. (2015) speculated that the relevant changes in Southern Ocean circulation could be a result of enhanced Ekman upwelling of relatively warm water associated with the cyclonic wind anomalies present over the eastern Pacific Southern Ocean. However, we find that the mPWP and boundary condition simulations do not show an increase in wind stress curl around Antarctica poleward of the Antarctic Circumpolar Current, as would be expected for enhanced upwelling (Supplementary Fig. 3.13).

Yet, we do find a strong increase in poleward ocean heat transport south of 65°S on the order of 0.1 PW in FCM-BC and FCM-mPWP (Fig. 3.6a), consistent with an increase

in ocean heat flux convergence in the West Antarctic, particularly at very high latitudes (Fig. 3.6b). Note that 0.1 PW corresponds to heat flux convergence of around 4 Wm^{-2} averaged over the polar cap poleward of 65°S, which is larger than the average mPWP ERF values in this region (Fig. 3.3), illustrating why these ocean heat transport changes are such a substantial driver of southern high latitude warming and, in turn, on tropical and global warming through low-cloud feedbacks.

Enhanced Southern Ocean warming in FCM-mPWP was found to be common across models participating in PlioMIP2 (Weiffenbach et al., 2023), and was associated with dramatic sea ice loss and a decline in abyssal Southern Ocean overturning due to enhanced stratification. We also find significant warming of the water column in FCM-mPWP (Supplementary Fig. 3.14), and a decline in sea ice extent that is much more marked in FCM-mPWP and FCM-BC than FCM-CO_2 (Fig. 3.5g-i), indicating a smaller role for CO_2 in driving sea ice loss and surface warming during the mPWP. The change in sign from cooling to warming in the eastern tropical Pacific in FCM-BC relative to SOM-BC provides evidence that the negative SW ERF there (Fig. 3.3b,h) is not sufficient to drive tropical Pacific cooling in the presence of Southern Ocean warming.

To better isolate the climatic effect of Southern Ocean warming, we perform an additional slab ocean simulation in which we modify the Qflx field in the Southern Ocean south of 65°S to reproduce FCM-BC ocean heat transport changes in only this region. Specifically, all ocean grid cells south of this latitude were prescribed to match the ocean heat flux convergence and mixed layer depth simulated in the last 50 year average of FCM-BC; PI Qflx is retained elsewhere. The results show strong Southern Ocean warming that extends to the tropics in all ocean basins, resulting in a reduction in subtropical low-cloud cover and larger global warming, broadly consistent with FCM-BC (Supplementary Fig. 3.15). This indicates that Southern Ocean heat transport changes (Supplementary Fig. 3.16) alone are sufficient to produce the differences between fully coupled model and slab ocean model responses to mPWP boundary condition forcing, and are the main reason for the larger global warming response in FCM-BC compared to SOM-mPWP. We note that a similarly important role for ocean dynamics in changing Southern Ocean and equatorial SSTs has been found in LGM simulations (Zhu and Poulsen, 2021).

An evaluation of the slab ocean model biases (Supplementary Fig. 3.17) in both the PI and mPWP simulations suggests that up to 2°C of Southern Ocean temperature increases in the slab ocean simulations may be due to a methodological bias in this model set-up (e.g., resulting from using annual-mean mixed layer depths in the SOM versus seasonally-varying mixed layer depths in the FCM). However, this is a relatively small fraction (less than 10%) of the regional warming simulated in FCM-mPWP relative to SOM-mPWP, meaning that the Southern Ocean warming response in the fully coupled model can be attributed to ocean heat transport changes.

To what degree do ice sheet changes drive the Southern Ocean warming of the mPWP, relative to all other boundary conditions? To answer this, we examine an existing fully coupled CESM2 simulation that uses mPWP continental topography and ocean bathymetry, including a closed Bering Strait and exposed Sunda and Sahul shelves, but PI control ice sheet extent, vegetation, and CO_2-levels (including PI topography in Antarctica) (Eo280 in Feng et al., 2022; here referred to as FCM-Oro). We find that this simulation shows no Southern Ocean warming (Supplementary Fig. 3.18) and a global temperature anomaly of -0.6°C relative to the PI. These results suggest a leading role for West Antarctic ice sheet loss in driving Southern Ocean warming, in turn resulting in eastern tropical Pacific warming, a reduction in subtropical low-cloud cover, and an amplification of the global temperature response to mPWP forcings. Further work would be needed to unambiguously attribute Southern Ocean heat transport and temperature changes to West Antarctic ice sheet loss, rather than to other boundary condition changes that could remotely affect the region (namely changes in northern hemisphere vegetation and the Greenland ice sheet).

3.5 mPWP radiative feedbacks

Thus far we have found that boundary conditions – primarily associated with ice sheet loss – have an outsized influence on global temperature response of the mPWP. Here, we use our values of ERF and equation (3.1) to quantify the global radiative feedback, λ, for each slab ocean and fully coupled simulation described above (Table 3.3). We also apply equation (3.1) to all-sky and clear-sky radiation fields separately to estimate the respective role of cloud feedbacks – here approximated by the Cloud Radiative Effect (CRE) per degree of

warming. We note that a more sophisticated method using radiative kernels or perturbations would be necessary to account for effects such as cloud masking of water vapor, lapse rate, and surface albedo changes in the calculation of a cloud feedback (Soden et al., 2004); it is, however, a good approximation where surface albedo changes are small (over open ocean).

As expected, we find that the global feedback associated with mPWP boundary conditions differs from that associated with CO_2 within both slab ocean and fully coupled simulations. Within the former, boundary conditions drive a far more negative feedback ($\lambda_{BC} = -1.42$ $Wm^{-2}K^{-1}$ in SOM-BC) than does CO_2 ($\lambda_{CO_2} = -0.80$ $Wm^{-2}K^{-1}$ in SOM-CO_2), consistent with boundary conditions inducing a subtropical cooling and low-cloud cover increase not seen under CO_2 forcing. However, we find the opposite behavior within the fully coupled model: boundary conditions drive a far less negative feedback ($\lambda_{BC} = -0.59$ $Wm^{-2}K^{-1}$ in FCM-BC) than does CO_2 ($\lambda_{CO_2} = -1.01$ $Wm^{-2}K^{-1}$ in FCM-CO_2), consistent with increased poleward ocean heat transport to the southern high latitudes resulting in Southern Ocean warming and a subsequent decrease in subtropical cloud cover.

Table 3.3: Global radiative feedbacks calculated as in equation (3.1). The period of analysis, ΔN, and ΔT values for each simulation are as noted in Table 3.1.

	ΔN (Wm^{-2})	ΔF (Wm^{-2})	ΔT (K)	λ ($Wm^{-2}K^{-1}$)
FCM-mPWP	0.25	3.83	5.10	−0.70
FCM-BC	0.03	1.65	2.85	−0.59
FCM-CO_2	0.14	2.17	2.01	−1.01
FCM-2xCO_2	0*	4.53	4.07*	−1.12*
SOM-mPWP	0.08	3.83	4.46	−0.84
SOM-BC	0.02	1.65	1.15	−1.42
SOM-CO_2	−0.03	2.17	2.41	−0.91
SOM-2xCO_2	0.09	4.53	5.56	−0.80

*corresponds to a regression of ΔN on ΔT over years 100-300, with the equilibrium temperature extrapolated to $\Delta N = 0$ Wm^{-2}.

The spatial patterns of radiative feedbacks (defined as the local top-of-atmosphere radiative response per degree of global surface temperature change), help to explain why the boundary conditions drive a small global temperature response in the slab ocean model: a strong negative cloud feedback over areas of surface cooling in the eastern subtropical Pacific – a pattern that is reversed in the fully coupled model (Fig. 3.7b,e,h). Note that in all simulations, the subtropical Pacific cloud feedback is locally positive (amplifying local surface temperature changes); therefore, when quantified in terms of a global temperature change, the change in sign between model configurations (Figs. 3.7 and 3.8) stems from the subtropical Pacific cooling in SOM-BC resulting in a local increase in low-cloud cover despite global warming, and from the subtropical Pacific warming in FCM-BC resulting in a local decrease in low-cloud cover with global warming. Furthermore, relatively larger warming in the Southern Ocean, subtropical Pacific Ocean, and North Atlantic Ocean in FCM-BC and FCM-mPWP corresponds to a more-positive cloud feedback in these regions, resulting in an overall feedback that is less negative under boundary conditions than CO_2.

The global feedback of the mPWP (λ_{mPWP}) can be understood as a weighted sum of λ_{BC} and $\lambda_{\mathrm{CO_2}}$ separately. This can be seen by applying equation (3.1) to each simulation separately and allowing for different feedbacks; at equilibrium this gives $\Delta T_{\mathrm{mPWP}} = -\Delta F_{\mathrm{mPWP}}/\lambda_{\mathrm{mPWP}}$, $\Delta T_{\mathrm{CO_2}} = -\Delta F_{\mathrm{CO_2}}/\lambda_{\mathrm{CO_2}}$, and $\Delta T_{\mathrm{BC}} = -\Delta F_{\mathrm{BC}}/\lambda_{\mathrm{BC}}$. Assuming global temperature response (and ERF) sums linearly for these simulations – a good approximation for the fully coupled model – we can approximate $\Delta T_{\mathrm{mPWP}} = \Delta T_{\mathrm{CO_2}} + \Delta T_{\mathrm{BC}}$ and $\Delta F_{\mathrm{mPWP}} = \Delta F_{\mathrm{CO_2}} + \Delta F_{\mathrm{BC}}$. From equation (3.1) applied at equilibrium, the global feedback under full mPWP forcing can then be written as

$$\begin{aligned} \lambda_{\mathrm{mPWP}} &= -\frac{\Delta F_{\mathrm{mPWP}}}{\Delta T_{\mathrm{mPWP}}}, \\ &\approx \lambda_{\mathrm{CO_2}} \frac{\Delta T_{\mathrm{CO_2}}}{\Delta T_{\mathrm{mPWP}}} + \lambda_{\mathrm{BC}} \frac{\Delta T_{\mathrm{BC}}}{\Delta T_{\mathrm{mPWP}}}. \end{aligned} \tag{3.3}$$

That is, the mPWP feedback is the sum of the feedbacks under CO_2 alone and boundary conditions alone, weighted by the respective fractional contributions of those scenarios to total mPWP warming. From values in Table 3.2, equation (3.3) provides an estimate $\lambda_{\mathrm{mPWP}} \approx -0.73$ $\mathrm{Wm^{-2}K^{-1}}$, in good agreement with the actual value of $\lambda_{\mathrm{mPWP}} = -0.70$ $\mathrm{Wm^{-2}K^{-1}}$ derived from equation (3.1) applied to the fully coupled mPWP simulation.

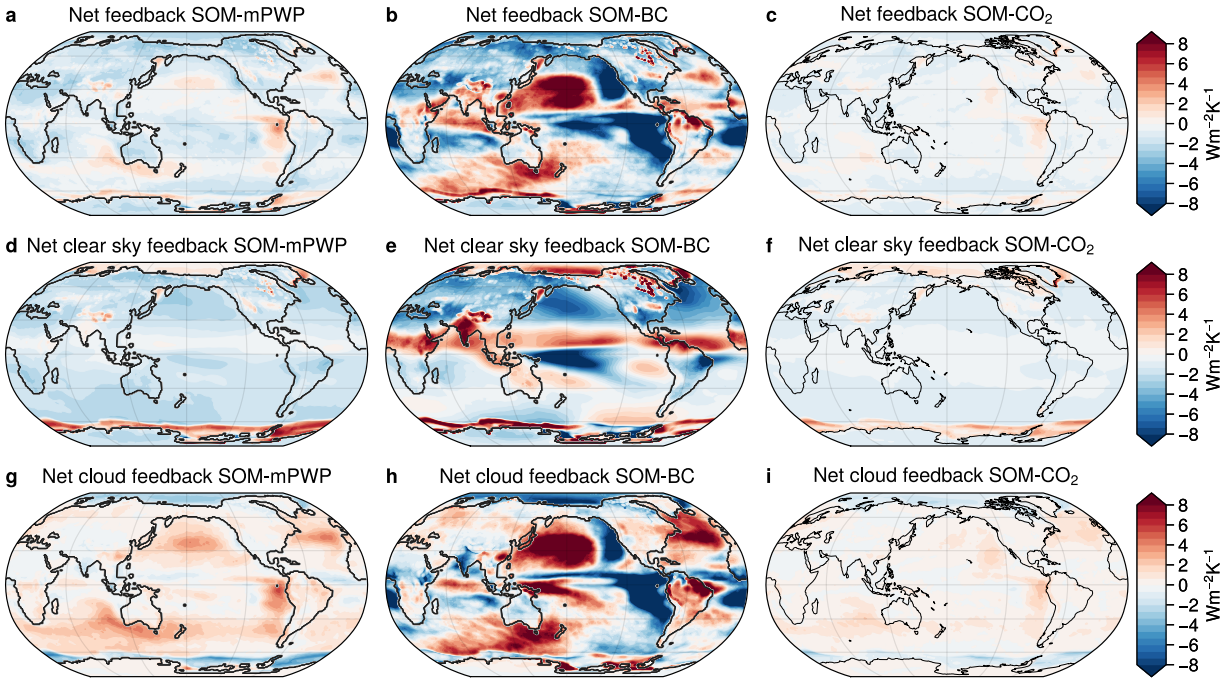

Figure 3.7: Net (a-c), clear sky (d-f), and cloud (g-i) radiative feedbacks from slab ocean simulations, calculated using equation (3.1) and normalized by the global mean surface air temperature response. The cloud feedback is calculated using the difference between all-sky and clear-sky TOA radiative imbalance anomalies (CRE per degree of warming).

equation (3.3) shows why the value of λ_{mPWP} must be between the values of $\lambda_{\mathrm{CO_2}}$ and λ_{BC}, and why λ_{mPWP} is closer to λ_{BC} in the fully coupled model (because ΔT_{BC} is larger than $\Delta T_{\mathrm{CO_2}}$). Equation (3.3) does not provide an accurate estimate of λ_{mPWP} in the slab ocean model, where the assumption of linearity does not hold, but it still provides qualitative reasoning for why λ_{mPWP} is close to $\lambda_{\mathrm{CO_2}}$ in the slab ocean model (because $\Delta T_{\mathrm{CO_2}}$ is much larger than ΔT_{BC}).

To what extent do feedbacks operating during the mPWP represent a good analog to those operating under greenhouse gas forcing today? Some mPWP-like boundary conditions (e.g., ice sheet and vegetation changes) can be expected to occur slowly over the coming centuries, while other mPWP-like boundary conditions (e.g., changes in land topography and ocean bathymetry) are not expected to occur in the same way even in the distant

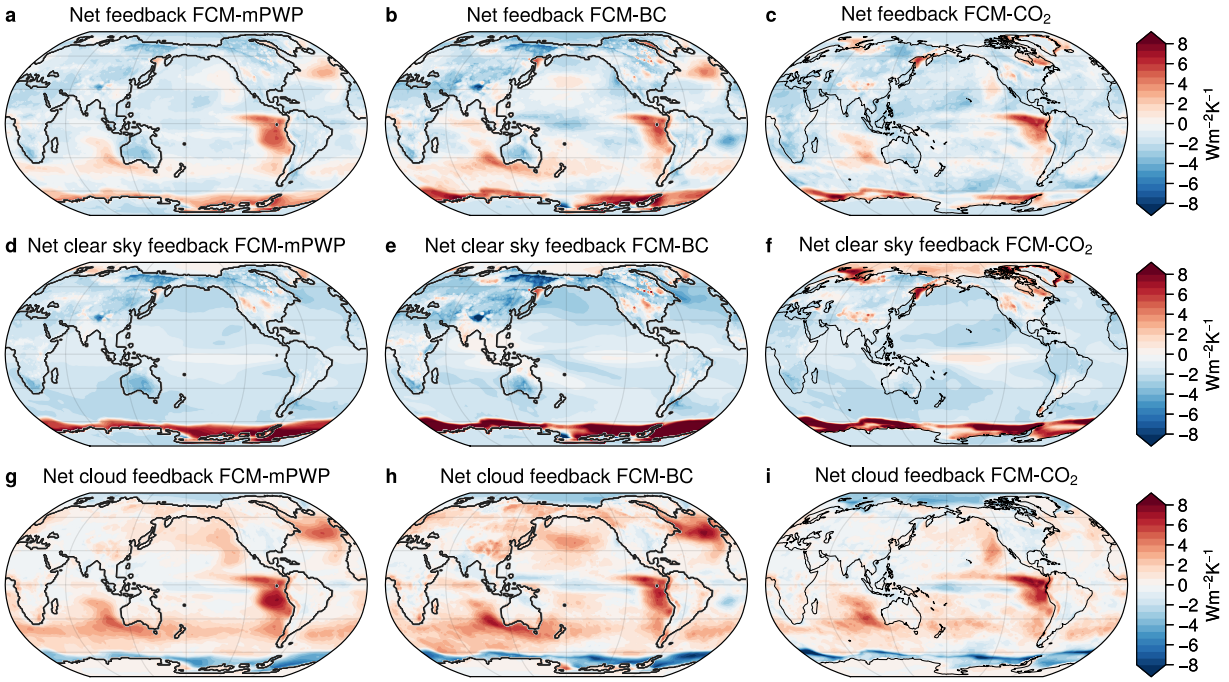

Figure 3.8: As in Fig. 3.7, but for fully coupled simulations.

future. It is therefore important to quantify the extent to which λ_{mPWP} differs from the feedback governing near-term warming in the absence of these boundary conditions. To do so, we calculate the difference between λ_{mPWP} and an estimate of the global feedback under abrupt CO_2 doubling (Tables 3.1 and 3.3), $\lambda_{2\mathrm{xCO_2}}$, as:

$$\Delta\lambda = \lambda_{2\mathrm{xCO_2}} - \lambda_{\mathrm{mPWP}}. \tag{3.4}$$

We interpret $\Delta\lambda$ as primarily reflecting different patterns of surface warming induced by the unique boundary conditions of the mPWP (which are not expected to occur in the near-term future) and induced by modern-day CO_2 forcing. We can then infer that $\Delta\lambda$ represents a paleoclimate 'pattern effect', following other recent studies (e.g., Cooper et al. 2024). $\Delta\lambda$ has been widely estimated for the historical record, during which greater warming has been observed in the western tropical Pacific than the eastern tropical Pacific, enhancing deep convection and increasing tropospheric stability, and thus producing more negative (stabilizing) cloud feedbacks (Dong et al., 2019; Andrews et al., 2018, 2022) – an

SST pattern that is expected to reverse with greenhouse-gas driven future warming, driving less-negative feedbacks (Ceppi and Gregory, 2017; Dong et al., 2019; Forster et al., 2021). Equation (3.4) provides a quantification of this SST pattern effect for the mPWP.

We compare the global feedback under mPWP forcing to the feedback under an abrupt CO_2 doubling, which defines ECS when equilibrium warming is reached. ECS has been found to be highly correlated with warming over the 21st century within climate models (e.g., Sherwood et al., 2020). Although we have extended fully coupled CESM2's abrupt CO_2 doubling simulation (FCM-2xCO_2) to a length of 300 years, it is still far from equilibrium at the end of runtime. We therefore calculate ECS as the equilibrium temperature change extrapolated from a Gregory regression following Gregory et al., 2004 (producing an ECS of approximately 4.1°C; see Table 3.3 and footnote therein; Supplementary Fig. 3.19). We then calculate $\lambda_{2\text{x}CO_2} = -F_{2\text{x}CO_2}/\text{ECS}$, where $F_{2\text{x}CO_2}$ is the ERF quantified using a fixed-SST simulation as described in Section 3.3 (Table 3.3). For the slab ocean model, we perform a CO_2 doubling simulation (SOM-2xCO_2) that reaches equilibrium, allowing us to quantify ECS directly as the global average temperature anomaly (producing an ECS of approximately 5.6°C; Tables 3.1 and 3.3).

The difference between ECS values in slab ocean and fully coupled versions of CESM2 may reflect differences in ocean heat transport between the two configurations. Our estimate of ECS in the slab ocean version of CESM2 (5.6°C) is slightly higher than the widely-cited estimate of 5.1-5.3°C, which has been derived from previous 2xCO_2 SOM simulations (Danabasoglu et al., 2020; Gettelman et al., 2019; Zelinka et al., 2020), but identical to the most recent estimate using the same model configuration (Zhu et al., 2021). On the other hand, our estimate of ECS in the fully coupled CESM2 (4.1°C) is substantially lower than widely-cited estimates of ECS estimated from abrupt CO_2 quadrupling simulations with CESM2 (> 5°C) but higher than estimates based on regression over the previously-available 150 years of abrupt CO_2 doubling (e.g., 3.4°C in Poletti et al., 2024). Our 2xCO_2 ERF estimate of 4.5 Wm^{-2} is greater than 1/2 the value of published estimates of 4xCO_2 ERF (6.7 Wm^{-2}, Poletti et al., 2024; 8.9 Wm^{-2}, Smith et al., 2020). We can therefore infer that the difference we find in ECS is associated with greater sensitivity of CESM2 at higher global warming levels, rather than non-logarithmic behavior of CO_2 forcing with

concentration (Poletti et al., 2024; Rugenstein and Armour, 2021; Bloch-Johnson et al., 2021). Our estimate of ECS of 4.1°C, based on a 300 year-long simulation of CO_2 doubling, is consistent with the 900 year FCM-CO_2 simulation scaled logarithmically to a higher CO_2 level (4.1°C), and likely represents the current most accurate estimate of ECS for CESM2.

We calculate a pattern effect, $\Delta\lambda$, equal to -0.07 $\mathrm{Wm^{-2}K^{-1}}$ in our slab ocean model, but -0.4 $\mathrm{Wm^{-2}K^{-1}}$ in the fully coupled. That is, feedbacks induced by mPWP forcings are substantially less negative than feedbacks induced by CO_2 doubling alone in the fully coupled model. This large value of $\Delta\lambda$ in the fully coupled model reflects the fact that mPWP boundary conditions, hypothesized here to be associated with the response of ocean circulation to ice sheet loss, induce less-negative feedbacks primarily via the cloud changes described above (Fig. 3.8). That we find such an important role for subtropical cloud cover in the warming of the mPWP is consistent with previous work identifying, through energy balance analysis, a decrease in cloud albedo in the Southern Hemisphere subtropics across the PlioMIP2 ensemble (Burton et al., 2023); it is also supported by research demonstrating that subtropical cloud albedo reductions alone can enhance regional surface temperatures sufficient to reproduce reconstructed tropical Pacific SSTs of the mPWP (Burls and Fedorov, 2014). In the following section, we discuss the implications of these findings for estimates of the modern-day ECS based on mPWP reconstructions.

3.6 Discussion

Efforts to constrain ECS and future warming from paleoclimate records often make the implicit assumption that the climate response to paleoclimate forcing is analogous to that associated with today's greenhouse gas forcing. Recent research leveraging both models (Zhu and Poulsen, 2021) and data assimilation approaches (Cooper et al., 2024) suggests that this may not be a good assumption for the LGM. In particular, the response to LGM ice sheet forcing was found to be characterized by less-negative radiative feedbacks than the response to CO_2 forcing due to the distinct spatial patterns of temperature change they induce, referred to in the literature as the "pattern effect". The implication is that more of the LGM cooling may have come from ice sheet forcing, rather than CO_2, than previously recognized. Thus, high values of ECS (measuring global temperature response to CO_2

forcing alone) are inconsistent with reconstructed LGM cooling (Cooper et al., 2024).

Motivated by these findings, we evaluated the potential for mPWP boundary condition forcing to produce a different climate response than CO_2 forcing. By performing novel fixed-SST simulations with CESM2, we quantified the ERF of mPWP boundary condition and CO_2 changes. Our estimates can be compared to the mPWP forcing estimates used in the community ECS assessment of Sherwood et al. (2020) (hereafter SW20). Here, total greenhouse gas (including methane and nitrous oxide) forcing was found to be 2.2 Wm^{-2} – identical to our mPWP CO_2 ERF estimate of 2.2 Wm^{-2}. As in Haywood et al. (2016), we interpret our CO_2 forcing (corresponding to 400 ppm rather than 375 ppm as in SW20) as representative of the total greenhouse gas forcing of the mPWP. SW20 represented boundary condition forcing by applying an additional inflation factor to the greenhouse gas forcing to arrive at a central estimate of total mPWP of 3.3 Wm^{-2}, or 0.5 Wm^{-2} smaller than our estimate of 3.8 Wm^{-2}. Because the greenhouse gas forcing estimates are nearly identical, the difference in total mPWP forcing comes from our value of boundary condition ERF being 0.5 Wm^{-2} larger than the central estimate implied in SW20.

Our higher value of mPWP boundary condition forcing may reflect our use of a single climate model (CESM2), or our use of the modern ERF definition, which allows for rapid atmospheric adjustment to forcing (increasing ERF relative to instantaneous radiative forcing, for example). We note that it is unclear how corrections to ERF (to remove the effect of land surface temperature changes on top-of-atmosphere radiation) should be applied for non-CO_2 forcings, such as ice sheet or vegetation changes, that are localized over land and induce significant local temperature change. Here we have simply followed common practice (Andrews et al., 2021) via equation (3.2), which results in a slight increase in our estimate of ERF. Not adjusting for this surface temperature change would decrease our estimate of total forcing by about 0.3 Wm^{-2}, bringing it closer to the SW20 forcing estimate but also increasing our pattern effect estimate from $-0.4 Wm^{-2}K^{-1}$ to $-0.5 Wm^{-2}K^{-1}$. Use of the adjusted ERF therefore provides a slightly more conservative estimate of the mPWP pattern effect in CESM2.

It would be valuable to perform similar 30-year simulations with fixed-SSTs in other atmospheric models to inform future mPWP forcing estimates, and to quantify each of

the various forcings individually. Inclusion of fixed-SST simulations in the next PlioMIP, for example, would allow for an estimation of intermodel spread in mPWP forcings and feedbacks.

3.6.1 Implications for estimating ECS

To the extent that mPWP-like boundary condition (i.e., ice sheet and vegetation) changes will occur in response to modern greenhouse gas warming, they will do so slowly. We can therefore expect them to have little impact on the climate in the near-term (i.e., over this century), but a potentially large impact on timescales of multiple centuries to millennia (PALEOSENS, 2012; Knutti and Rugenstein, 2015) And while there is no strict separation of timescales allowing one to disregard these slower feedbacks, they are not typically included in estimates of modern-day ECS. In Section 3.5, we found the difference between the global feedback relevant to future warming ($\lambda_{2x\mathrm{CO}_2}$) and to the mPWP ($\lambda_{\mathrm{mPWP}}$) to be -0.4 $\mathrm{Wm}^{-2}\mathrm{K}^{-1}$ within CESM2, due to differences in the spatial pattern of warming resulting in a less-negative feedback under full mPWP forcing. The common assumption that the feedbacks at the mPWP are similar to those under greenhouse gas forcing today ($\lambda_{2\mathrm{xCO}_2} \approx \lambda_{\mathrm{mPWP}}$, or $\Delta\lambda = 0$) would therefore bias estimates of ECS upward (toward a too-sensitive climate). However, this can be corrected for by accounting for these feedback differences (Cooper et al., 2024).

To illustrate this principle, we consider the mPWP-constrained likelihood of ECS following the methods of SW20. In particular, to infer the modern-day ECS from mPWP evidence, we have

$$\begin{aligned} \mathrm{ECS} &= -\frac{\Delta F_{2\mathrm{xCO}_2}}{\lambda_{2\mathrm{xCO}_2}}, \\ &= -\frac{\Delta F_{2\mathrm{xCO}_2}}{\lambda^*_{\mathrm{mPWP}} + \Delta\lambda}, \end{aligned} \tag{3.5}$$

where $\lambda^*_{\mathrm{mPWP}}$ is the estimate of the mPWP feedback determined using equation (3.1) applied to the mPWP at equilibrium. That is,

$$\lambda^*_{\mathrm{mPWP}} = -\frac{\Delta F^*_{\mathrm{mPWP}}}{\Delta T^*_{\mathrm{mPWP}}}, \tag{3.6}$$

where $\Delta F^*_{\mathrm{mPWP}}$ is an estimate of mPWP forcing and $\Delta T^*_{\mathrm{mPWP}}$ is the mPWP global temperature change from proxy reconstructions. If we take $\Delta F^*_{\mathrm{mPWP}}$ and $\Delta T^*_{\mathrm{mPWP}}$ from SW20

(Supplementary Information) and set $\Delta\lambda = 0$, then the likelihood for ECS reproduces that in SW20 with a maximum likelihood of 3.2 K and a long tail toward high values (Fig. 3.9). Updating the SW20 likelihood function to match the latest proxy-based assessment of $\Delta T^*_{\mathrm{mPWP}} = 3.9$ K ± 1.1 K (one sigma; Annan et al. 2024) increases this estimate of ECS to 4.2 K (solid black line in Fig. 3.9).

Next, we illustrate the effect of also updating the mPWP forcing to match the values estimated using the ERF in this study. Our results suggest a value of ΔF_{mPWP} that is about 0.5 Wm^{-2} larger than the central value of $\Delta F^*_{\mathrm{mPWP}}$ used in SW20 (Section 3.3) due to a different estimate of mPWP boundary condition forcing. Although our estimate of ΔF_{mPWP} is from a single model (CESM2), it represents the first quantification of the ERF for the mPWP. To illustrate the impact of the larger forcing, we maintain the uncertainty in the original SW20 value of $\Delta F^*_{\mathrm{mPWP}}$, but increase its median value by 0.5 Wm^{-2}. This change produces a maximum likelihood for ECS that is slightly lower than the updated SW20 estimate (green line in Fig. 3.9).

Finally, we revise $\Delta F^*_{\mathrm{mPWP}}$ to match our CESM2 value while also accounting for our CESM2-estimated value of $\Delta\lambda$ (equation 3.5). This produces a maximum likelihood of 2.8K with much smaller likelihood of high values (purple curve in Fig. 3.9). This illustrates how accounting for feedback differences between the mPWP and modern-day CO_2-induced warming, in the absence of slow boundary condition changes, has the potential to produce estimates of ECS from mPWP evidence that are substantially lower and better constrained.

3.6.2 Implications for estimating ESS

Our results also have consequences for the estimation of Earth System Sensitivity (ESS), which captures the long-term (multi-centennial to multi-millenial) climate response to a doubling of CO_2. In this framing, large-scale ice sheet and vegetation changes are treated as additional feedbacks on warming in response to CO_2 forcing. Given the small impact that non-ice sheet related orographic changes (such as ocean gateway closures) and ocean bathymetric changes were found to have on the modeled mPWP climate in CESM simulations (Feng et al., 2017), the response to boundary condition forcing of the mPWP can be

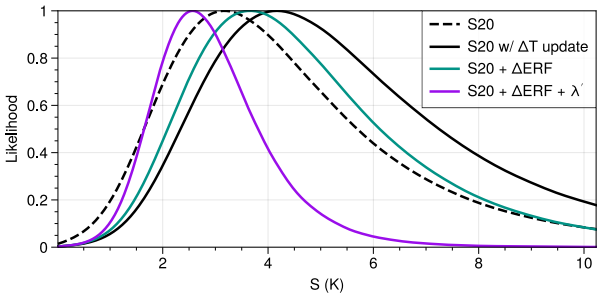

Figure 3.9: Inference of modern-day climate sensitivity from the mPWP, reproduced from Sherwood et al. (2020) (dashed black line), updated based on latest-available proxy evidence (Annan et al., 2024) (solid black line), and then adjusted to account for enhanced boundary condition forcing found in this study (green line), as well as the mPWP pattern effect (purple line).

thought of as representing plausible changes that we may eventually see under modern-day greenhouse forcing (e.g., Haywood et al., 2013), with relevance to future climate on very long timescales.

From climate model simulations of mPWP warming, ESS can be estimated as ESS $\approx \Delta T_{\mathrm{mPWP}} \cdot F_{2\mathrm{xCO_2}}/F_{\mathrm{CO_2}}$, where ΔT_{mPWP} is the warming from the full mPWP forcing and the factor $F_{2\mathrm{xCO_2}}/F_{\mathrm{CO_2}}$ is needed to convert to a warming from CO_2 doubling given that mPWP warming arose from a lower CO_2 level (e.g., Haywood et al., 2013). Thus, the ratio of ESS to ECS can be expressed as:

$$\frac{\mathrm{ESS}}{\mathrm{ECS}} \approx \frac{\Delta T_{\mathrm{mPWP}}}{\mathrm{ECS}} \cdot \frac{\Delta F_{2\mathrm{xCO_2}}}{\Delta F_{\mathrm{CO_2}}} \tag{3.7}$$

which for fully coupled CESM2 gives a value of ESS/ECS = 2.6 (from values in Table 3.3). That is, as estimated by CESM2, the long-term warming from CO_2 doubling would be amplified by a factor of 2.6 due to boundary conditions, relative to ECS. For example, given our mPWP-informed central estimate of 2.8 K (Fig. 3.9), this implies an ESS of 7.3 K – occurring on the timescale over which ice sheets and vegetation fully respond to and, in turn, amplify the warming. While this amplification factor is substantially higher than previous estimates of 1-2 (Haywood et al., 2013; Lunt et al., 2010, 2012), it is still within the bounds of the multi-model ensemble of PlioMIP2 (1.1-2.9) (Haywood et al., 2020).

What explains the high ESS/ECS ratio in CESM2? Using $\lambda_{2xCO_2} \approx \lambda_{CO_2}$ and $\Delta T_{mPWP} \approx \Delta T_{CO_2} + \Delta T_{BC}$ (good approximations for CESM2), equation (3.7) can be rewritten as:

$$\frac{ESS}{ECS} \approx 1 + \frac{\Delta F_{BC}}{\Delta F_{CO_2}} \cdot \frac{\lambda_{CO_2}}{\lambda_{BC}} \tag{3.8}$$

which gives a value of ESS/ECS = 2.3 – a decent approximation to the factor calculated directly from equation (3.7). When written this way, we can now interpret the ratio ESS/ECS in terms of two factors. The first ($\Delta F_{BC}/\Delta F_{CO_2}$) represents the ratio of boundary condition ERF to CO_2 ERF. If ΔF_{BC} were zero, then ESS would be equal to ECS. However, as we saw above, boundary condition ERF for the mPWP in CESM2 is larger than previous estimates (SW20). If we only consider this contribution by setting $\lambda_{CO_2} = \lambda_{BC}$ in equation (3.8), then ESS/ECS would be equal to only 1.8 – substantially smaller than the actual value of ESS/ECS, and in good agreement with previous estimates that assume a constant feedback across mPWP forcings (Haywood et al., 2013; Lunt et al., 2010). CESM2's large value of ESS/ECS comes from the fact that a large ΔF_{BC} also induces a less-negative radiative feedback than does ΔF_{CO_2} such that the second factor ($\lambda_{CO_2}/\lambda_{BC}$) is large, altogether resulting in ESS/ECS well above 2.

It is possible that studies arriving at much lower values of ESS/ECS could have done so by overestimating ECS by neglecting to account for the pattern effect on radiative feedbacks (Hansen et al., 2023) or by relying on estimates using high CO_2 (e.g., quadrupling) simulations (e.g., Haywood et al., 2020 and citations therein). Generally speaking, where high latitude forcing results in high latitude temperature change (often referred to as a reduced meridional temperature gradient in the paleoclimate record (Forster et al., 2021)), less-negative feedbacks result; correcting for this implies a lower modern ECS when ice sheet forcing is small.

3.7 Conclusions

In this study, we found that mPWP boundary conditions were responsible for over half of the mPWP warming despite amounting to less than half of the mPWP ERF (Table 3.3). This implies that mPWP boundary conditions induce less-negative radiative feedbacks than does CO_2 (Table 3.3), consistent with their distinct spatial patterns of temperature and low-cloud

responses (Fig. 3.2). We proposed that a primary reason for the less-negative cloud feedback under mPWP boundary condition forcing is increased poleward ocean heat transport in the Southern Ocean, resulting from a loss of the West Antarctic ice sheet. Warming of the Southern Ocean then enhances warming of the eastern tropical Pacific Ocean through an atmospheric teleconnection pathway that ultimately results in a reduction in subtropical low clouds, and thus a less-negative global feedback under boundary condition forcing.

It is possible that CESM2 overestimates the climate response to mPWP boundary conditions. This model is known to have a large subtropical cloud feedback, which strengthens the teleconnection between Southern Ocean warming and tropical Pacific warming (Kang et al., 2023a). However, CESM2 has been found to compare better than other climate models to observations of subtropical cloud properties (Kang et al., 2023b; Davis and Medeiros, 2024). While the results shown here are surely model-dependent, they highlight a need to quantify the mPWP ERF within additional atmosphere-only models and to produce more robust estimates of ERF and $\Delta\lambda$ for the mPWP using both additional climate models and proxy-constrained data assimilation methods.

The results presented here have two important implications for future climate prediction. On the one hand, that so much of the mPWP warming may have come from non-CO_2 boundary conditions (inducing less-negative feedbacks via an SST pattern effect) suggests that near-term warming in the absence of these changes may be smaller than commonly reported. There exist opportunities to constrain mPWP warming patterns and feedbacks using proxy data assimilation, for example following similar methods to Cooper et al. (2024). Our results suggest that those efforts could lead to stronger constraints on the high end of ECS. On the other hand, they raise the possibility that ESS may be larger than commonly estimated, implying substantially higher global warming in the long term response to CO_2 as slow feedbacks (i.e., vegetation and ice sheet changes) materialize. Our results demonstrate the importance of incorporating these processes in projections of climate change.

3.8 Supplementary Information

This section contains the following supplementary information:

1. Spatial maps of the preindustrial (PI) sea surface temperature (SST) and sea ice fields prescribed in all atmosphere-only model simulations (Fig. 3.10); and the PI ocean heat flux convergence (Qflx) and mixed-layer depth fields prescribed in slab ocean model simulations (Figs. 3.11 and 3.12).

2. Precipitation anomalies relative to the PI for all slab ocean and fully coupled simulations (Fig. 3.12).

3. Wind stress curl anomalies relative to the PI over the Southern Hemisphere south of 40°S in slab ocean and fully coupled simulations (Fig. 3.13).

4. Depth profiles of Southern Ocean potential temperatures (Fig. 3.14)

5. A sensitivity experiment isolating the effect of Southern Ocean Qflx changes on the global temperature response (Fig. 3.15), with the prescribed Qflx and mixed layer depths shown as anomalies from the preindustrial (Fig. 3.16). Slab ocean biases relative to the fully coupled model when using Qflx and mixed layer depths derived from the mPWP coupled model within the slab ocean model (Fig. 3.17). A sensitivity test isolating the influence of mPWP ice sheets and vegetation from Feng et al. (2022), shown here as the difference between all mPWP non-CO_2 boundary conditions and mPWP orography (FCM-Oro) (Fig. 3.18). FCM-Oro includes the topographic changes associated with a closed Bering Strait and Canadian Arctic Archipelago, above-sea-level height of the Sunda and Sahul shelves of Indonesia, and all other topographic anomalies unrelated to ice sheet changes.

6. Gregory regression of surface temperature with TOA radiative imbalance used to estimate ECS in the 2xCO_2 simulation (Fig. 3.19) Overview of method for estimating the sensitivity likelihood from the mPWP.

To generate the sensitivity likelihood functions shown in Fig. 3.9 of the main text, we follow the Bayesian approach outlined in SW20, where λ is constrained to best reproduce

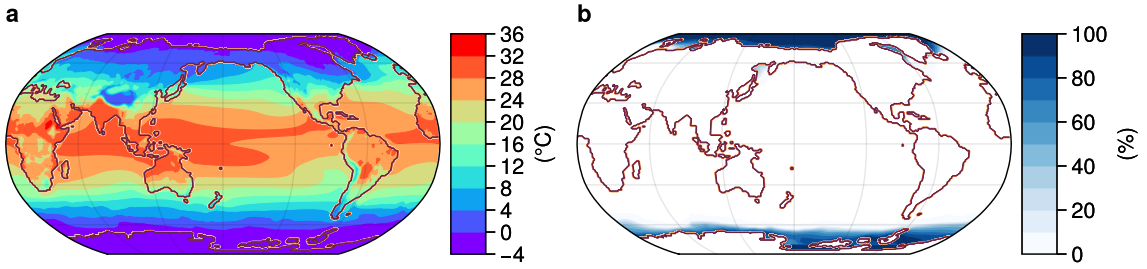

Figure 3.10: Preindustrial sea surface temperature (a) and sea ice concentration (b) fields used in all fixed SST simulations (ATM-mPWP, ATM-BC, ATM-CO_2).

observational estimates of the surface temperature change of the mPWP (ΔT), which is given by

$$\Delta T = \frac{-\Delta F_{\mathrm{CO2}}(1 + f_{\mathrm{CH4}})(1 + f_{ESS})}{\frac{\lambda}{1+\zeta}} \tag{3.9}$$

where f_{CH4} and f_{ESS} are inflation factors representing the additional forcing from methane and N_2O, and ice sheets and vegetation, respectively, and $1 + \zeta$ represents the transfer between quasi-equilibrium and regression estimates of the feedback.

Our estimate of mPWP forcing (the numerator in equation 3.9) is updated to match the ERF found in this study (Table 3.2 in the main text), while retaining the same uncertainty distributions used in SW20.

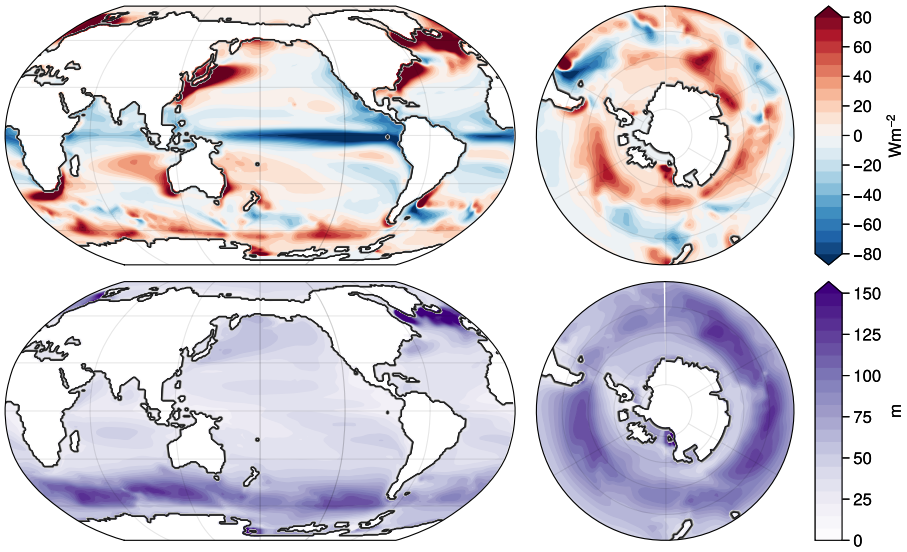

Figure 3.11: Preindustrial ocean heat flux convergence (top row) and mixed layer depth (bottom row) prescribed in all slab ocean simulations (SOM-mPWP, SOM-BC, SOM-CO_2).

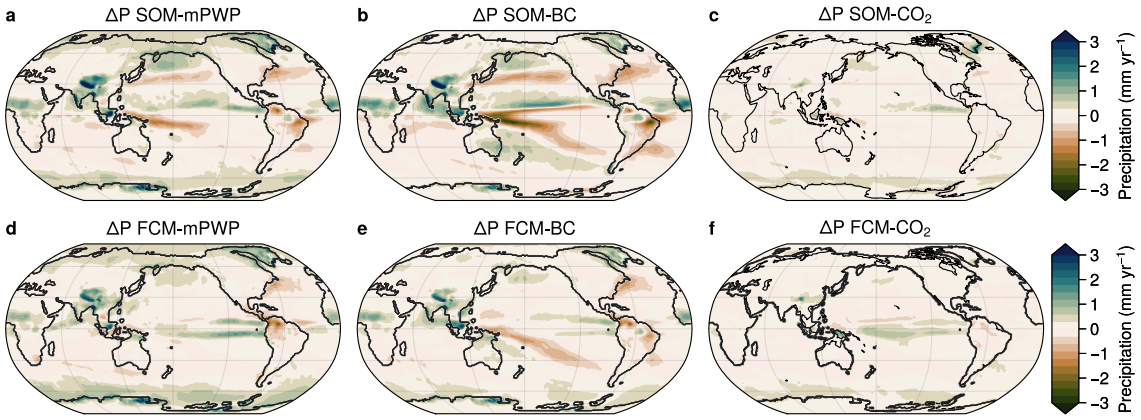

Figure 3.12: Large-scale convective precipitation rate anomalies for all slab ocean (a-c) and fully coupled (d-f) simulations.

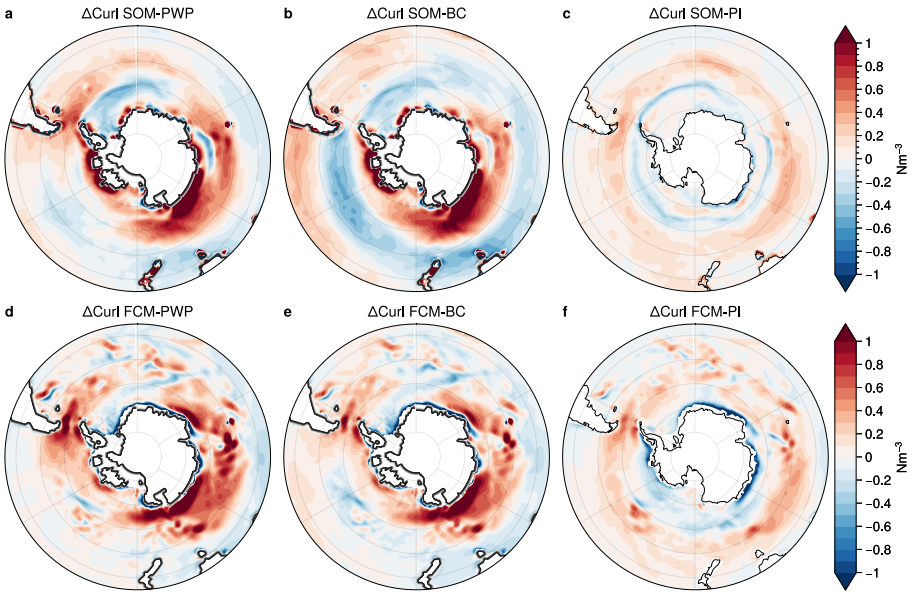

Figure 3.13: Anomalous wind stress curl over the Southern Ocean, calculated from atmospheric and ocean model outputs for slab ocean model (a-c) and fully coupled simulations (d-f) respectively (negative values indicate an increase in wind stress curl in the Southern Hemisphere).

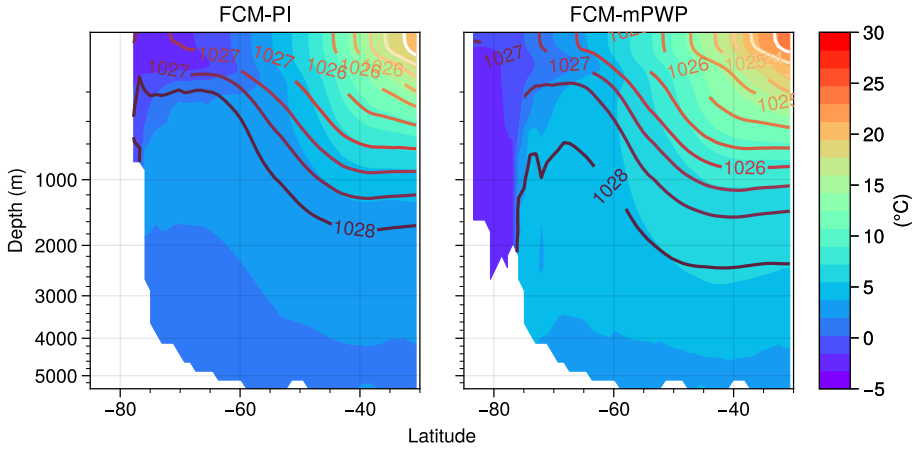

Figure 3.14: Zonal mean Southern Ocean potential temperature as a function of depth for fully coupled PI and mPWP simulations. Potential density is shown as colored contour lines (units of kgm^{-3}).

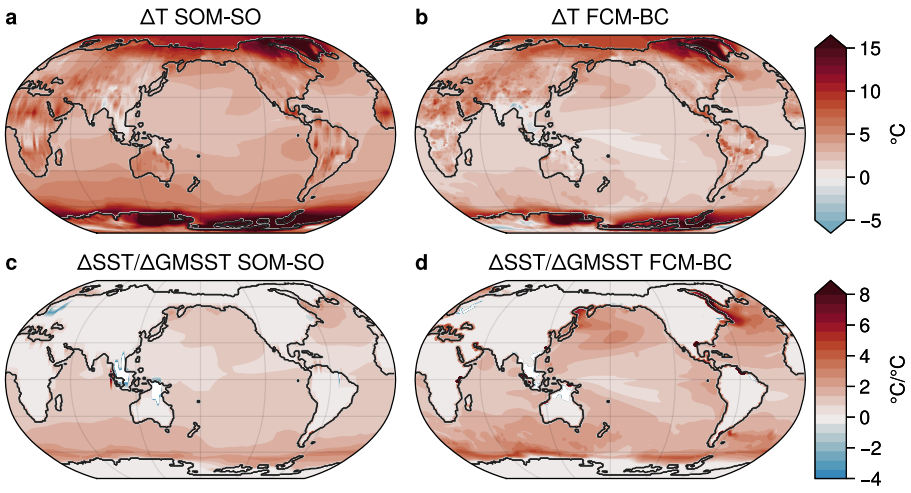

Figure 3.15: Effect of Southern Ocean circulation adjustments in response to boundary conditions on global temperature in the slab ocean model (SOM-SO). Surface temperature and normalized SST anomalies for SOM-SO relative to SOM-PI (a,c), and FCM-BC relative to FCM-PI (b,d) for comparison.

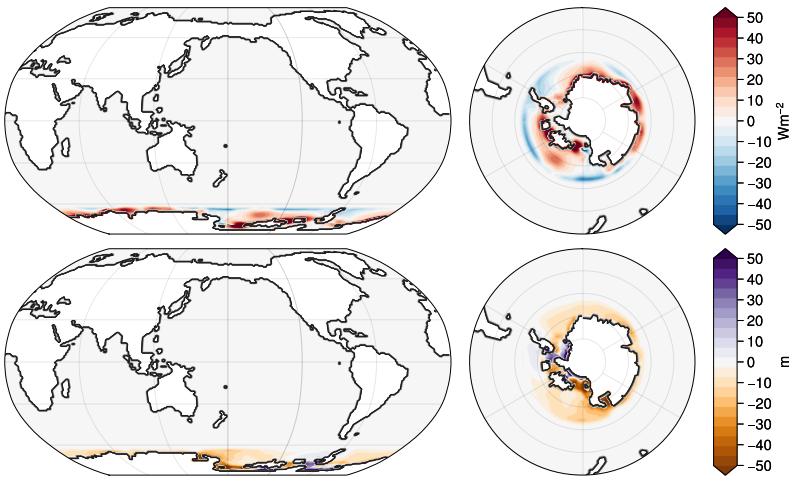

Figure 3.16: Qflx (top row) and mixed layer depth (bottom row) anomalies relative to the preindustrial (Fig. 3.11) prescribed in SOM-SO.

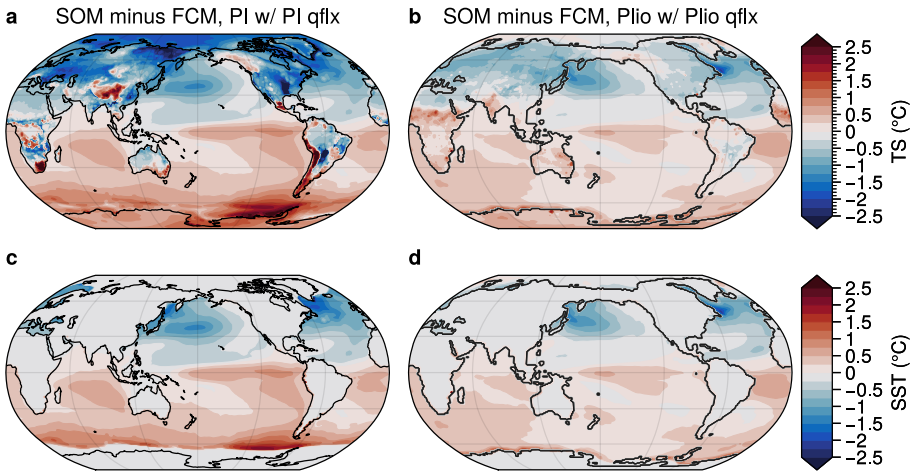

Figure 3.17: Slab ocean model biases relative to fully coupled simulations. Preindustrial (a,c) and mPWP (b,d) surface temperature and SST anomalies simulated in slab ocean simulations where Qflx and mixed layer depth are prescribed from the corresponding fully coupled simulations.

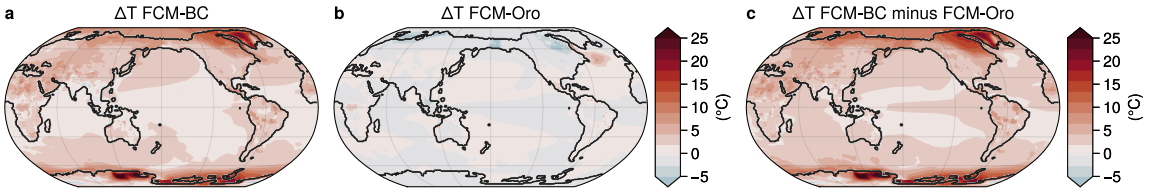

Figure 3.18: Sensitivity simulations reproduced from Feng et al. (2022). Subtracting the influence of mPWP orography (FCM-Oro) from FCM-BC allows for an examination of the effect of mPWP ice sheets and vegetation in isolation. Surface temperature anomalies for FCM-mPWP and FCM-Oro (a,b) and their difference (c).

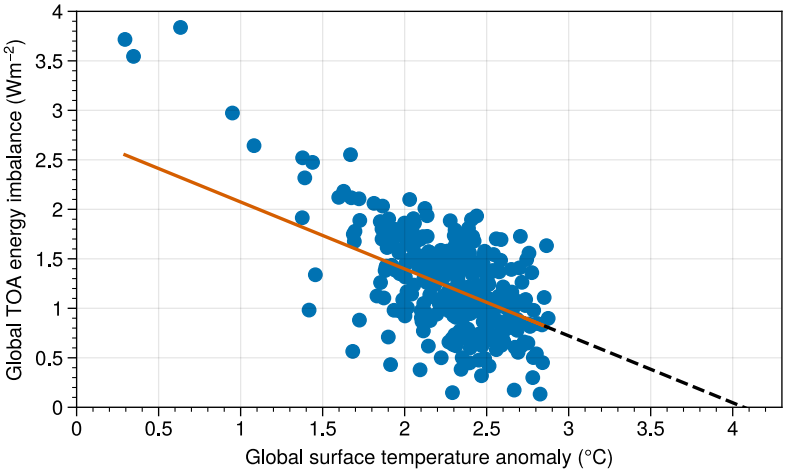

Figure 3.19: Gregory regression of surface temperature anomalies on the TOA radiative imbalance for the abrupt CO_2 doubling experiment (FCM-2xCO_2), after extending the simulation to 300 years. A regression line for the last 200 years is shown in orange. ECS is the surface temperature extrapolated to where N = 0 (4.1K).

Chapter 4

ISOLATING THE CLIMATE RESPONSE TO WEST ANTARCTIC ICE SHEET LOSS AND NORTHERN HEMISPHERE VEGETATION CHANGES OF THE MID-PLIOCENE

Abstract

The large marine-grounded West Antarctic Ice Sheet (WAIS) is sensitive to climate changes, and was thought to have been completely diminished during the mid-Pliocene Warm Period (mPWP, ∼3.3Mya). Observational evidence suggests that the ice sheet may fully retreat over the next several centuries to a millenium, making its absence in the mPWP one of the more relevant features of this paleoclimate for studies of future warming. Modeling work suggests that the oceanization of West Antarctica – the inundation of ocean into the highest southern latitudes of this region – may have amplified the overall global warming of the mPWP, and hence its overall sensitivity. Here, we test this hypothesis through single forcing experiments in a state-of-the-art global climate model, and find that increasing high latitude ocean heat transport results in gradual Southern Ocean warming in response to a loss of WAIS – an effect not captured through atmospheric processes alone. Sensitivity tests with other boundary conditions of the mPWP provide further evidence that this ocean adjustment drove substantial warming in the mPWP, revealing a potential for enhanced global warming on very long timescales.

4.1 Introduction

The West Antarctic Ice Sheet (WAIS) is rapidly losing mass, with recent estimates suggesting that the loss of the large Pine Island and Thwaites Glaciers could occur over the next couple of centuries (Alley et al., 2015; Rignot et al., 2014; van den Akker et al., 2024; Joughin et al., 2011). Meanwhile, it remains possible that marine ice cliff and ice sheet instabilities could trigger the complete loss of WAIS over multiple centuries to a millennium, even with substantial reductions in greenhouse gas emissions (Forster et al., 2021; Reese

et al., 2023; Rignot et al., 2014). In contrast, the East Antarctic Ice Sheet is expected to persist for much longer (Forster et al., 2021). Many studies have investigated the atmospheric and oceanic drivers of historical WAIS mass loss, with observational and modeling evidence suggesting that much of the observed loss has been driven by wind trends resulting in warmer subsurface waters reaching the base of its ice shelves (e.g., Schmidtko et al., 2014; Pritchard et al., 2012; Alley et al., 2015; O'Connor et al., 2024).

The opposite line of investigation – what the effect the retreat of WAIS would have on the atmosphere, ocean, and global climate – has received much less attention. Research on past warm climate states, for which the absence of WAIS is a prominent feature, can partially address this unknown. Indeed, several studies have investigated the climate response to a retreat of WAIS within the context of the mid-Pliocene Warm Period (mPWP) (Weiffenbach et al., 2023; Dvorak et al., 2025), or the Last Interglacial (Steig et al., 2015; Holloway et al., 2016), periods during which paleoclimate reconstructions of sea level indicate an absence of WAIS at global temperatures only a few degrees above the preindustrial (Dowsett et al., 2016; Tierney et al., 2025; Lunt et al., 2013). However, studies on the climate response to a loss of WAIS have been complicated by the presence of other paleoenvironmental boundary conditions. In the case of the mPWP, these are: the absence of portions of the Greenland Ice Sheet, differences in orography and ocean bathymetry, changes in vegetation over Northern Hemisphere (NH) land masses, and changes in the East Antarctic Ice Sheet (Dowsett et al., 2016). Other modeling efforts have been limited to studying the fast atmospheric response to an idealized topographic lowering of WAIS (Steig et al., 2015; Pauling et al., 2023; Lunt et al., 2013; Justino et al., 2015). However, a complete loss of the marine-grounded ice sheet would result in the inundation and exposure of ocean (Pritchard et al., 2025; Seroussi et al., 2024), with potential consequences for Southern Ocean circulation and climate beyond what can be inferred from the atmospheric response to topographic changes alone.

The mPWP has been shown to be an imperfect analogue for near-term, greenhouse gas-driven climate change because a large fraction (over half) of its global warming, relative to preindustrial, is thought to have been driven by changes in its paleoenvironmental boundary conditions (e.g., changes in vegetation and ice sheet extent) that are not expected to occur this century (Chapter 3). However, the mPWP may become more relevant to climate change

on longer timescales (multiple centuries to millennia), insofar as these boundary condition changes emerge as slow feedbacks on greenhouse gas warming. And if such changes do occur in the future, they will each do so on their own timescale, with their own unique impacts on global climate. This motivates the need to study the climate response to each of the mPWP boundary condition changes separately. With relevance to predicting long-term global climate, we ask, what features of the mPWP climate were driven by a loss of WAIS versus other paleoenvironmental features, such as those associated with changes in NH vegetation or the Greenland Ice Sheet?

The Pliocene Model Intercomparison Project (PlioMIP; Haywood et al., 2013, 2016, 2024) is a large-scale, collaborative modeling effort that has enabled the study of the climate's sensitivity to mPWP paleoenvironmental boundary conditions, treated separately from its sensitivity to CO_2 (e.g., Dvorak et al. 2025; Weiffenbach et al. 2023; Burton et al. 2023; Feng et al. 2022). However, no PlioMIP experiments separate the effect of the loss of the WAIS from that of NH vegetation and ice sheet changes. Moreover, changing the extent of the WAIS requires an adjustment to the land-sea mask and local bathymetry in the ocean model, which was done in concert with all other land-sea mask adjustments in PlioMIP simulations. Another consideration is that some PlioMIP simulations were initialized with warm ocean conditions in order to reduce the time to equilibrium (e.g., as in Feng et al., 2020), making it challenging to study causal mechanisms that may become more apparent in the transient response to paleoenvironmental boundary condition changes.

To overcome these limitations, we design and perform a set of simulations with a state-of-the-art global climate model using a novel set of boundary conditions that allow us to separate the transient response to the loss of WAIS (including the associated inundation and exposure of ocean) from the response to changes in NH vegetation and ice sheets. In one set of simulations, we alter only the height and extent of WAIS (including oceanized West Antarctica), while holding all other forcings fixed at preindustrial levels; in another set of simulations, we alter only NH vegetation and Greenland Ice Sheet changes. We further separate the atmospheric and oceanic responses to each of these boundary conditions by incorporating them in both fully coupled and mixed layer (slab) ocean models (Table 4.1), following the methods of Chapter 3. The results presented here shed further light on the

drivers of mPWP warming, as well as on the particular dynamics of this paleoclimate state that may occur as anthropogenic global warming continues to unfold.

4.2 Methods

We carry out a suite of simulations using the state-of-the-art Community Earth System Model 2 (CESM2; Danabasoglu et al., 2020) in fully coupled and slab ocean configurations, where all components (atmosphere, land, ocean and sea ice) are as described in Chapter 3, Section 3.2. We conduct three sets of simulations: a fully coupled preindustrial control (PI) simulation (FCM-PI); fully coupled and slab ocean simulations where only the WAIS is changed to match the mPWP state (FCM-WAIS and SOM-WAIS, respectively); and fully coupled and slab ocean simulations with only vegetation cover and Northern Hemisphere (Greenland) ice sheet extent changed to match the mPWP state (FCM-NH and SOM-NH, respectively) (Table 4.1). As in Chapter 3, we expand the curvilinear ocean grid mesh in each WAIS simulation to 394 x 320 to resolve dynamic processes in the oceanized West Antarctic, following Feng et al. (2020).

In all fully coupled simulations, we initialize the ocean model from rest on January 1st with full-depth temperature and salinity values derived from the average over all December months of the last 100 years of a 1200-year preindustrial control simulation (CMIP6; Eyring et al., 2016). We also perform a new, 100-year preindustrial control simulation (FCM-PI) that is initialized from rest on January 1st with this same temperature and salinity field, and run with preindustrial greenhouse gas levels and boundary conditions. All anomalies in FCM-WAIS and FCM-NH are calculated with respect to FCM-PI to account for any drift that occurs due to model initialization. In regions of new Antarctic ocean grid cells in FCM-WAIS, temperatures and salinity values at all depths are extrapolated from the zonal average of the southernmost surface values of the PI (approximately -1.6°C and 33.9 psu, respectively), following Feng et al. (2020), with a nine-point horizontal smoothing function then applied at each depth level.

In FCM-WAIS, we simulate an absence of WAIS by replacing the PI topography and ocean bathymetry from 90S to 65S and 278E to 325E with that of the mPWP dataset used in PlioMIP2 experiments, PRISM4 (Fig. 4.1; Dowsett et al., 2016; Feng et al., 2020).

While the mPWP East Antarctic Ice Sheet is slightly reduced compared to the modern in the PRISM4 dataset, we choose not to include this change because (1) previous work points to a more significant influence of WAIS changes on climate (Weiffenbach et al., 2023; Dvorak et al., 2025) and (2) this portion of the ice sheet is thought to be more resistant to global warming based on geological evidence (Kaplan et al., 2017; Forster et al., 2021), and thus may reduce the relevancy of the simulation to future projections. Due to uncertainty in proxy reconstructions, East Antarctic ice sheet changes, along with the above-sea-level topography changes of PRISM4, have also not been incorporated in some simulations recommended in the latest phase of PlioMIP (PlioMIP3, Haywood et al., 2024).

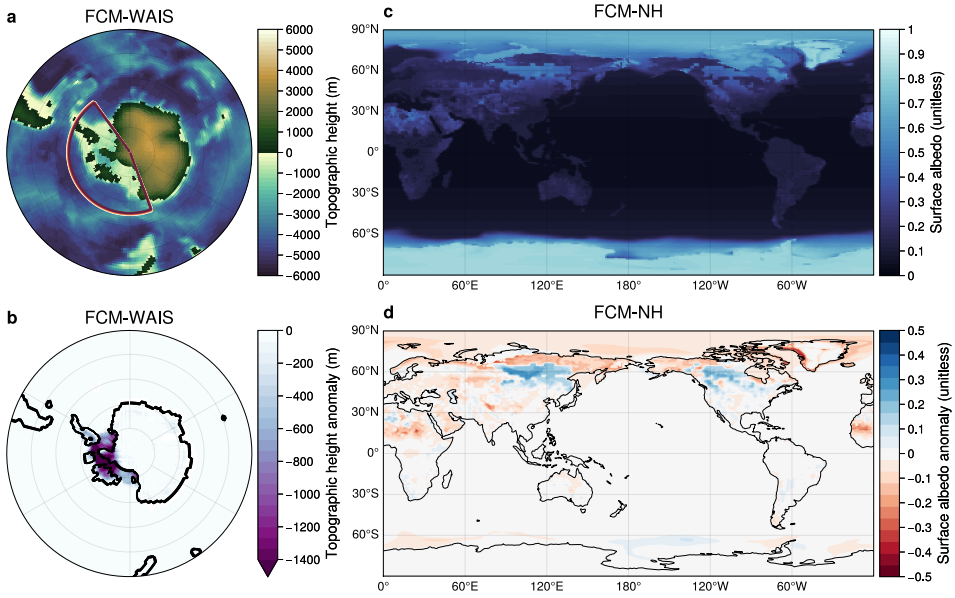

Figure 4.1: Topographic height prescribed as boundary conditions in FCM-WAIS (a) and its anomaly with respect to the boundary conditions of FCM-PI (b). Modeled surface albedo in response to prescribed vegetation and Greenland ice sheet changes in FCM-NH (c) and its anomaly with respect to FCM-PI (d). Note that snow cover can compensate albedo changes in areas of ice sheet retreat.

The land-sea mask used here is then remapped to the 1×1 degree grid of the atmosphere and land models. With the exception of the removal of land ice from the remaining land surface of WAIS, all land surface features (vegetation type and extent, soil properties,

etc.) of FCM-WAIS are identical to the PI. Greenhouse gas concentrations, atmospheric composition, and orbital parameters are also identical to the PI. We run the simulation for 300 years, and calculate anomalies over the first 100 years with respect to the same set of years in FCM-PI; all anomalies thereafter are calculated with respect to the last 30 years of FCM-PI (years 70-100) because drifts have diminished by that point in all variables considered.

In FCM-NH, we modify the land surface boundary conditions to simulate mPWP vegetation and Northern Hemisphere ice sheet changes by replacing the PI land surface dataset with that of the mPWP PRISM4 dataset north of 60°S (Feng et al., 2020; Dowsett et al., 2016) (note that mPWP vegetation and ice sheet changes between 0°N and 60°S are minimal in the dataset – hence 'NH', for short; Fig. 4.1). The modern-day land-sea mask is retained, and the land surface type and ice sheet extent of Antarctica is identical to the PI. As above, greenhouse gas concentrations, atmospheric composition, and orbital parameters are also identical to the PI. We therefore simulate mPWP vegetation and ice cover changes only where they occur on modern-day land, thus excluding vegetation features of the above-sea-level Bering Strait and Canadian Arctic archipelago in PRISM4. (Fig. 4.1c-d). The simulation is run for 100 years, and anomalies are calculated with respect to the same set of years in FCM-PI.

We also perform CAM6 slab ocean simulations that employ the same respective topographic and vegetation boundary conditions as described for FCM-WAIS and FCM-NH; however, ocean heat transport (OHT) is held constant in each simulation by prescribing mixed layer ocean heat flux convergence (Qflx) from the (CMIP6) fully coupled PI control climatology. Following Chapter 3, Section 3.4, ocean heat flux convergence is set to zero in the region of new ocean grid cells of West Antarctica in SOM-WAIS. A nine-point smoothing function is again used to smooth the transition from zero Qflx to PI control values, and a small residual is distributed across all grid cells to ensure a globally-integrated Qflx of zero. We run each slab ocean simulation for 50 years, and anomalies are calculated over an average of the last 30 years with respect to the preindustrial slab ocean simulation (SOM-PI) completed in Chapter 3 (84 years, with the last 50 used for analysis; Table 4.1).

Fully coupled and slab ocean simulations incorporating the full suite of mPWP non-CO_2

boundary conditions (FCM-BC and SOM-BC) are reproduced from previous work (Chapter 3; Feng et al., 2020; Table 4.1). Relative to our WAIS and NH experiments, FCM-BC and SOM-BC include additional changes in orography due to above-sea-level continental shelves and a reduction in the extent of the East Antarctic Ice Sheet. But because the former features have been shown to have a minimal impact on global climate (Feng et al., 2022), we expect the linear combination of WAIS and NH experiments to capture most of the warming in the BC simulations.

Table 4.1: Description of simulations used in this study.

Simulation description	**Model type (CESM2)**	**Simulation short name**	**Run-time (years)**	**Citation**
WAIS loss only	Fully coupled	FCM-WAIS	300	
	Slab ocean	SOM-WAS	50	
NH vegetation and ice sheet changes only	Fully coupled	FCM-NH	100	
	Slab ocean	SOM-NH	50	
Preindustrial	Fully coupled	FCM-PI	100	
	Slab ocean	SOM-PI	84	Dvorak et al. (2025)
All mPWP boundary conditions, at preindustrial CO_2 levels	Fully coupled	FCM-BC	400 (with warm ocean init.)	Feng et al. (2020)
	Slab ocean	SOM-BC	74	Dvorak et al. (2025)
	Slab ocean	SOM-BC-OHT*	64	Dvorak et al. (2025)

*anomalous OHT is prescribed from the corresponding fully-coupled simulation (FCM-BC) everywhere south of 60°S.

4.3 Results and Discussion

4.3.1 Climate response to isolated mPWP boundary conditions

Boundary condition changes of the mPWP elicit different climate responses between fully coupled and slab ocean modes of CESM2 (Fig. 4.2; see also Chapter 3). FCM-BC shows global warming everywhere, enhanced high latitude warming, and a reduced zonal SST gradient in the tropical Pacific. Conversely, SOM-BC features an eastern-equatorial, subtropical, and Pacific-sector Southern Ocean cooling response, with warming localized to the western ocean basins and very high latitudes. Global temperatures are significantly lower in SOM-BC relative to FCM-BC (1.1 vs. 2.9°C; Fig. 4.2). To explain this difference, we examine the climate response to the loss of WAIS, hypothesized in Chapter 3 to be a key driver of Southern Ocean and subtropical warming in FCM-BC. We then consider the response to NH vegetation and ice sheet changes (SOM-NH and FCM-NH simulations).

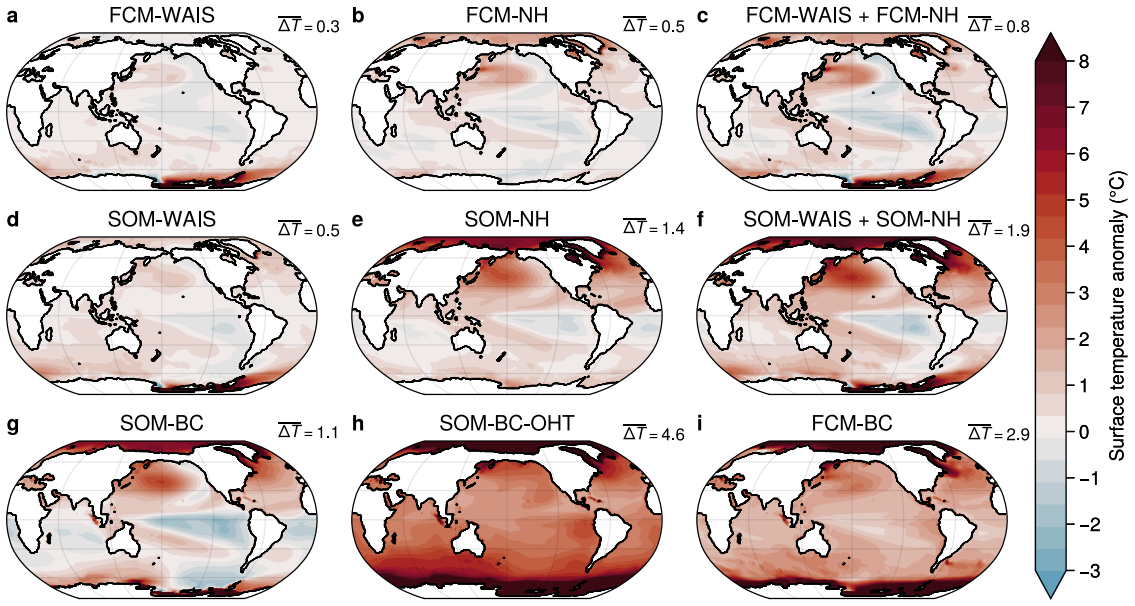

Figure 4.2: Fully-coupled (a-c), and slab ocean (d-f) surface temperature anomalies for WAIS and NH simulations, and their sums. SOM-BC, SOM-BC-OHT and FCM-BC anomalies reproduced from Dvorak et al. (2025) (g-i). Global average surface temperatures are indicated.

A complete loss of WAIS in both fully coupled and slab ocean models (FCM- and SOM-WAIS) results in significant, localized surface warming over areas of reduced topographic height; sea surface warming of the Atlantic and Indian sectors of the Southern Ocean; and broad, weak cooling in the equatorial and subtropical Pacific (Fig. 4.2a). This SST pattern can be attributed to changes in atmospheric circulation. The lowered topography creates a local cyclonic wind anomaly (Steig et al., 2015), which results in enhanced advection of warmer air through the Weddell Sea, and southwestward into the western portion of the Ross Sea (Fig. 4.3c-f). It also creates a broad anticyclonic circulation over the unchanged East Antarctic ice sheet, leading to an easterly wind anomaly (a decrease in climatological westerlies), and cooling off-shore of the continent. Similar atmospheric circulation changes have been shown in previous work isolating the topographic effect of the ice sheet (Steig et al., 2015; Otto-Bliesner et al., 2013). Surface warming leads to sea ice reduction, which further enhances Southern Ocean warming; indeed, the pattern and magnitude of warming in the first 30 years is closely tied to that of sea ice extent (Fig. 4.3c-d).

Further equatorward, strengthening of the climatological westerly winds (Supplementary Fig. 4.6) is simulated in the subtropical Pacific Ocean, consistent with previous work (Justino et al., 2015), causing cooling via enhanced evaporation. Westward-propagating atmospheric Rossby waves in the northern and southern extratropics are excited by the enhanced winds and deflected north and south, respectively, leading to a persistent negative IPO-like pattern of SSTs in the Pacific (Fig. 4.2a; Supp. Figs. 4.6 and 4.7).

FCM-NH shows a similar IPO-like pattern of SSTs, with cooling of the equatorial and eastern subtropical Pacific, and warming in the western basins (Fig. 4.2b). We surmise that different mechanisms are responsible for this tropical SST pattern in FCM-WAIS and FCM-NH. It is widely appreciated in the literature that extratropical forcing can exert an influence on equatorial temperatures by way of the positioning of the Intertropical Convergence Zone (ITCZ), and therefore surface winds (Kang et al., 2008; Pausata et al., 2015; Tseng and Hwang, 2024), or via surface buoyancy changes that affect the strength of the subtropical overturning cells in the ocean (Luongo et al., 2022).

In the case of positive forcing confined to the NH (as in FCM-NH), a top-of-atmosphere energy surplus in the NH requires net cross-equatorial southward atmospheric energy trans-

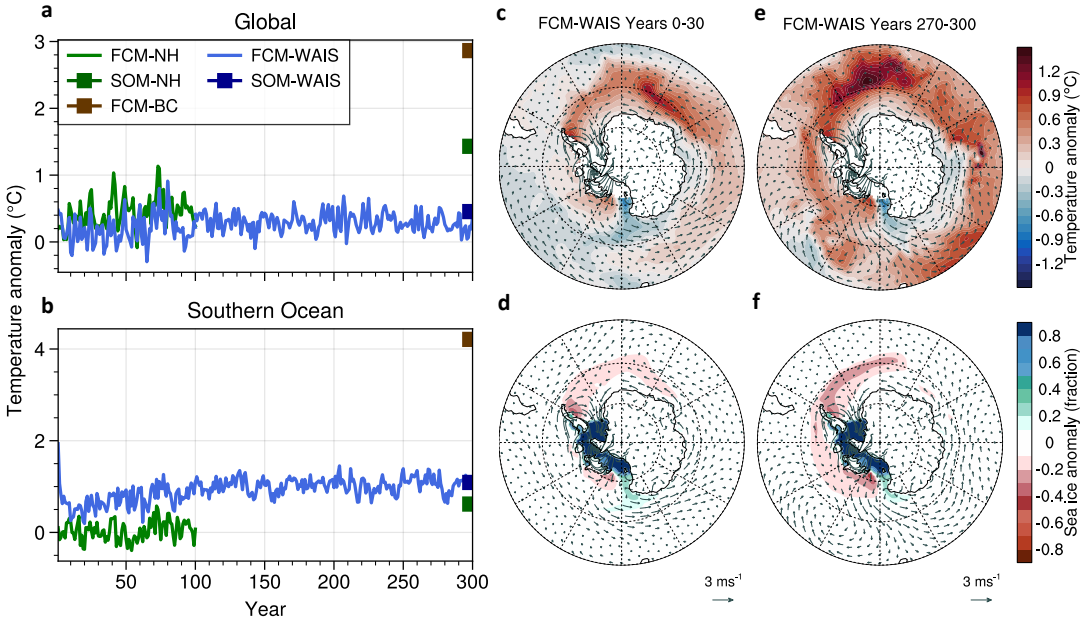

Figure 4.3: Global average surface air temperature anomaly (a) and Southern Ocean (90°S to 40°S) spatial average surface air temperature anomaly (b) taken with respect to FCM-PI (Methods) for FCM-WAIS (blue), FCM-NH (green), and the average over the last 100 years of FCM-BC (Feng et al., 2020) (purple squares). Averages of the last 30 years of SOM-WAIS and SOM-NH are also shown (blue and green squares, respectively). Southern Ocean SST and sea ice extent anomalies in the first 30 years (c,d) and the last 30 years (e,f) of FCM-WAIS. Wind anomalies are shown as vectors.

port, which is satisfied by an increase in energy flux at the equator in the upper (diverging) branch of the Hadley Cells. Because meridional and zonal winds are stronger south of the equator in the climatological mean, the resulting northward shift of the ITCZ also increases wind strength at the equator (Supp. Fig. 4.8; Pausata et al., 2015; Tseng and Hwang, 2024), leading to evaporative cooling, which is then enhanced via the Bjerknes feedback. In the subtropical Pacific, the joint cloud-WES feedback also acts to enhance cooling. That the same magnitude of cooling in these regions is captured in SOM-NH relative to FCM-NH supports the theory that atmospheric processes are sufficient to explain this pattern.

We find that our slab ocean simulations, SOM-WAIS and SOM-NH, together reproduce the SST pattern of SOM-BC (Fig. 4.2c,h), and sum to a global average sea surface tempera-

ture anomaly of 1.9°C compared to 1.1°C in SOM-BC. A similar SST pattern is found in the linear addition of FCM-WAIS (0.3°C globally, years 270-300) and FCM-NH (0.5°C globally, years 70-100) simulations; however, because those simulations are still far from equilibrium, the global temperature response is not close to that of the equilibrated FCM-BC (2.9°C), which shows significantly more tropical, extratropical and Southern Ocean warming.

Southern Ocean SSTs steadily increase over the duration of the FCM-WAIS simulation, with significant warming in all sectors, including the Pacific (Fig. 4.3b,e). While SOM-WAIS shows cooling in the Pacific sector of the Southern Ocean (Fig. 4.2a, Supp. Fig. 4.7), the last 30 years of FCM-WAIS are warmer here. Because the thermodynamic sea-ice albedo feedback is active in both simulations, the enhanced Pacific sector Southern Ocean warming in FCM-WAIS is attributable to dynamical changes in OHT. Furthermore, the global average SST in FCM-WAIS being nearly equal to that of SOM-WAIS (0.4°C) despite the deep ocean being far from equilibrium with the atmosphere – combined with the warming trend in the Southern Ocean – suggests that FCM-WAIS will continue to warm as OHT evolves and the simulation continues to equilibrate.

4.3.2 Ocean heat transport changes

One important feature of FCM-BC noted in Chapter 3 was its anomalous Southern Ocean heat transport, with an additional ∼0.15 PW (relative to the PI) transported southward near 65°S and an additional ∼0.15 PW transported northward near 55°S (brown line in Fig. 4.4d). While FCM-WAIS does not produce a similar magnitude of heat transport north and south of 60°S, its Southern Ocean heat transport anomalies are near zero for the first few decades and become more similar to those of FCM-BC by the end of run-time (Fig. 4.4d), although it is difficult to know if the same magnitude of OHT will be realized without running FCM-WAIS to equilibrium (which could take several millenia).

While the OHT anomalies are still relatively small in FCM-WAIS, we noted in Chapter 3 that the addition of ∼0.1 PW of southward OHT near 65°S (as in FCM-BC) amounts to ∼4 Wm^{-2} when averaged over the polar cap south of that latitude – a radiative forcing sufficient to drive significant Southern high latitude warming. This effect can also be seen

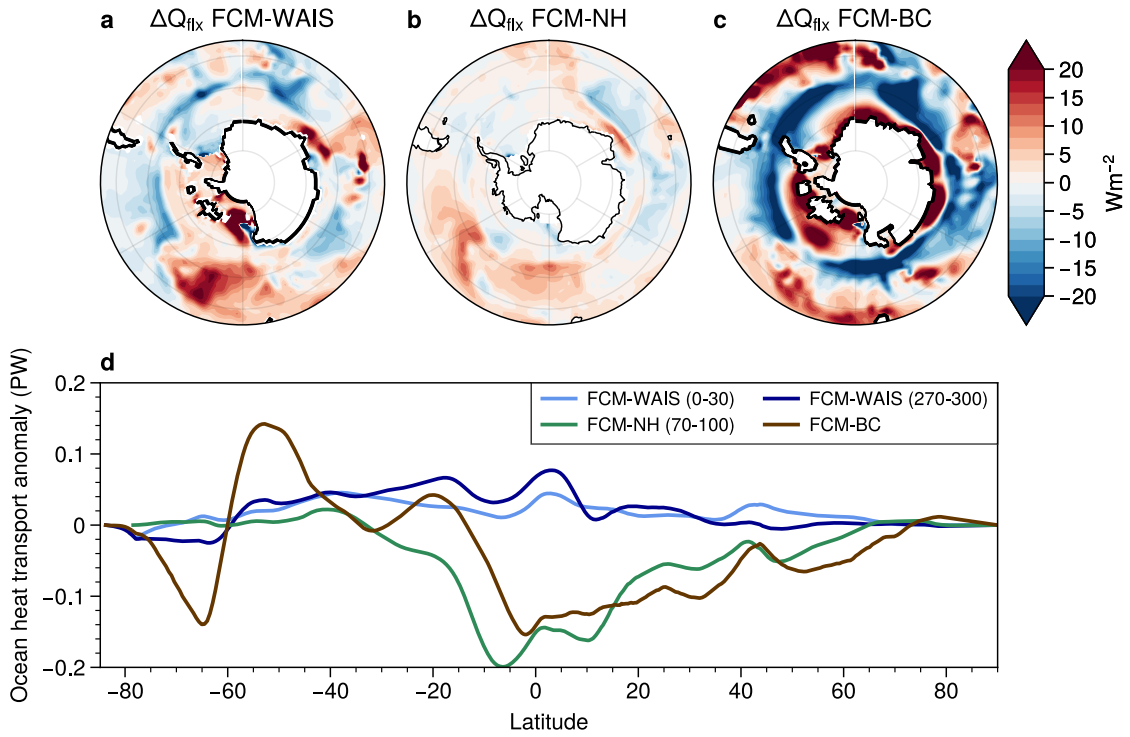

Figure 4.4: Southern Ocean net surface heat flux (Qflx) anomalies for FCM-WAIS and FCM-NH relative to FCM-PI (a,b), and for FCM-BC relative to the last 100 years of the CMIP6 preindustrial control from which FCM-PI is initialized (c) (positive out of the ocean); zonal-average OHT anomalies from the same simulations, where both the first 30 years (light blue) and the last 30 years (dark blue) of FCM-WAIS are shown (d).

in the surface heat budget (Fig. 4.4a-c). The ocean is a significant source of anomalous heat to the atmosphere in the Pacific sector of the Southern Ocean, and especially in the region of new ocean grid cells between 75 and 85°S, where the retreat of the ice sheet permits heat transport into the very highest southern latitudes (Fig. 4.4a).

FCM-NH shows no significant change in OHT south of 30°S, nor significant heat flux convergence in the Southern Ocean (Fig. 4.4b), suggesting that the NH changes do not contribute to the Southern Ocean heat transport or warming anomalies in FCM-BC (Fig. 4.2i). However, the NH forcing results in a significant increase in cross-equatorial southward heat transport, consistent with FCM-BC (Fig. 4.4d). Indeed, FCM-NH approximately reproduces the pattern of reduced northward OHT simulated in FCM-BC everywhere north of

the equator.

To determine if the Southern Ocean heat transport changes alone can explain the large magnitude of global warming simulated in FCM-BC relative to SOM-BC, we reproduce here a secondary CESM2 slab ocean simulation where the heat transport anomaly south of 60°S in FCM-BC was prescribed in a slab ocean model forced only with the boundary conditions of the Pliocene, but with OHT everywhere else equal to the preindustrial (SOM-BC-OHT, Fig. 4.2h; Table 4.1; Chapter 3). This produces broad Southern Hemisphere warming, with an SST pattern that much more closely resembles FCM-BC than SOM-BC, while mean global temperature is greater than in either simulation (4.4°C). The warming simulated in SOM-BC-OHT indicates that the OHT change (i.e., a redistribution with no global average energy input), which FCM-WAIS suggests is initiated by the loss of WAIS, is sufficient to overwhelm the atmospheric cooling in the subtropical and equatorial Pacific; this leads to more Southern Ocean and global warming on long timescales.

4.3.3 Mechanisms for ocean heat transport changes in response to a loss of WAIS

We find that Southern Ocean surface warming simulated in FCM-WAIS, amplified by the sea-ice albedo feedback, eventually penetrates to the depth of the thermocline (filled contours in Fig. 4.5a). This subsurface ocean temperature change largely explains the changes in OHT seen in the simulation. The climatological overturning circulation, acting on the anomalous temperature field, produces anomalous northward OHT near 55°S through the northward transport of anomalously warm waters near the surface and southward transport of anomalously cold waters at depth (Fig. 4.5a). This is driven by the large contribution of the Eulerian mean circulation to the northward heat transport anomaly (Supp. Fig. 4.9). However, at 65°S the climatological counter-clockwise circulation (not shown) acts to bring anomalously warm waters upward and southward along tilted isopycnals and anomalously cold waters northward at depth, producing an anomalous southward OHT. The resulting southward OHT anomaly associated with this Eulerian mean circulation is further increased by changes in eddy OHT at 65°S (Supp. Fig. 4.9).

We posit that cooling and salinification of the water column closest to the shelf (Fig. 4.5a)

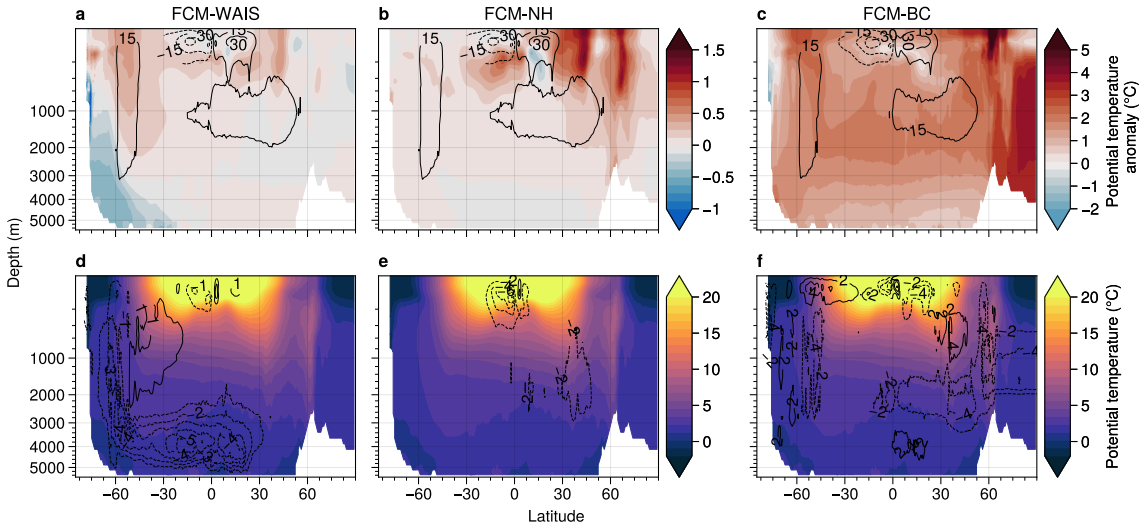

Figure 4.5: Southern Ocean depth profiles of potential temperature for the first and last 30 years of FCM-WAIS (a-b), and FCM-BC (c), with the preindustrial meridional overturning streamfunction shown as contours (MOC). (d-f) as in (a-c), but with preindustrial potential temperatures as filled contours and anomalous MOC as contour lines.

is a result of buoyancy loss from surface heat flux to the atmosphere (Fig. 4.4a) and brine rejection in the region of new sea ice formation (Fig. 4.3f). This may be responsible for the invigoration of the abyssal overturning cell (counterclockwise streamlines in Fig. 4.5d, Supp. Fig. 4.10), which would also enhance the southward heat transport anomaly around 65°S, given warmer subsurface waters at very high southern latitudes in the climatological mean (Fig. 4.5d-f)

In FCM-NH, a reduction in the strength of the Atlantic Meridional Overturning Circulation (AMOC) (Fig. 4.5e) is consistent with the decline in cross-equatorial northward heat transport described previously (section 4.3.1). While FCM-BC also shows a reduction in AMOC strength at depth, an increase nearer the surface is indicative of a shoaling of the circulation (Fig. 4.5f, Supp. Fig. 4.11; Feng et al., 2020). Therefore, the decline in AMOC strength in FCM-NH is likely a transient climate response; an eventual recovery of AMOC, and thus more enhanced high northern latitude warming, may be expected with longer simulation time. This could also explain the difference in cross-equatorial north-

ward heat transport observed between FCM-NH and FCM-BC; however, it is also possible that the topography differences of FCM-BC that are not captured here – specifically an above-sea-level Bering Strait and Arctic Archipelago – may exert an influence on AMOC, and therefore OHT, through changes in sea surface salinity (Weiffenbach et al., 2023; Feng et al., 2017; Otto-Bliesner et al., 2016).

The linear sum of FCM-WAIS and FCM-NH does not approximate FCM-BC because the former simulations are far from equilibrium; indeed, our slab ocean simulations *are* equilibrated, and we can see a similarity in SST patterns between SOM-WAIS + SOM-NH and SOM-BC (Fig. 4.2). But FCM-BC is far warmer, both globally and in the Southern Ocean, than either of those sets of slab ocean simulations (compare time-averaged squares in Fig. 4.3a-b). This suggests that changes in Southern Ocean heat transport are key to producing the very warm Southern Ocean temperatures found in FCM-BC. In addition, a warmer Southern Ocean would lead to warming of the subtropical and equatorial Pacific via atmospheric teleconnections and locally positive cloud feedbacks, enhancing global temperature (Dong et al., 2020, 2022; Chapter 3). Our reasoning that the slow Southern Ocean heat transport adjustment and warming can reproduce the full magnitude of global warming of the equilibrated FCM-BC is supported by the trend in OHT change shown in FCM-WAIS, the large magnitude of global warming simulated in SOM-BC-OHT, and the small effect that other topographical changes of the mPWP have been shown to have on the global climate in previous work (global mean surface temperature anomaly of ~ -0.5°C; see Supp. Fig. 4.12; Feng et al. 2022). A recovery of AMOC in response to the NH changes modeled here would further enhance global temperature through greater high northern latitude warming.

4.4 Conclusions

Here, we isolated the climate response to a loss of WAIS, including an oceanization of West Antarctica, in a state-of-the-art fully coupled climate model. In so doing, we have found that, while rapid changes in atmospheric circulation alone produce a small global temperature change (with cooling in the equatorial and subtropical Pacific Ocean), a slow ocean adjustment results in gradual Southern Ocean and global warming through changes

in OHT on timescales of hundreds to thousands of years. While we have modeled an abrupt removal here, a full retreat of the ice sheet would occur much more slowly, possibly on the same timescale as that of the OHT changes simulated here. Additional forcing through freshwater melt may be expected to complicate the response by acting to cool the Southern Ocean surface (e.g., Li et al., 2024; Golledge et al., 2019; Bronselaer et al., 2018), however this would be a transient effect; on long timescales, we still expect that the loss of WAIS and associated OHT changes would result in Southern Ocean and global warming.

Our results are consistent with Chapter 3, where we highlighted the role of OHT changes in driving the warming of the mPWP, absent CO_2 changes; and while we do not see a similar magnitude of warming from our combined WAIS and NH simulations, we are able to qualitatively reproduce the pattern of high-latitude heat transport changes, supporting the hypothesis that a slow ocean dynamical adjustment to the loss of WAIS is able to produce warming beyond what can be expected through atmospheric processes alone.

4.5 Supplementary Information

This section contains the following supplementary information:

1. A comparison of sea surface temperature and wind anomalies between the first 30 years and the last 30 years of FCM-WAIS (Fig. 4.6), and of normalized sea surface temperature anomalies across all simulations (Fig. 4.7).

2. Tropical precipitation and wind anomalies in both FCM-WAIS and FCM-NH, showing a northward shift of the ITCZ in the latter (Fig. 4.8).

3. A decomposition of northward heat transport anomalies into Eulerian mean and eddy components (Fig. 4.8).

4. Timeseries of Antarctic Bottom Water (AABW) formation rate anomalies for FCM-WAIS and FCM-NH (Fig. 4.9).

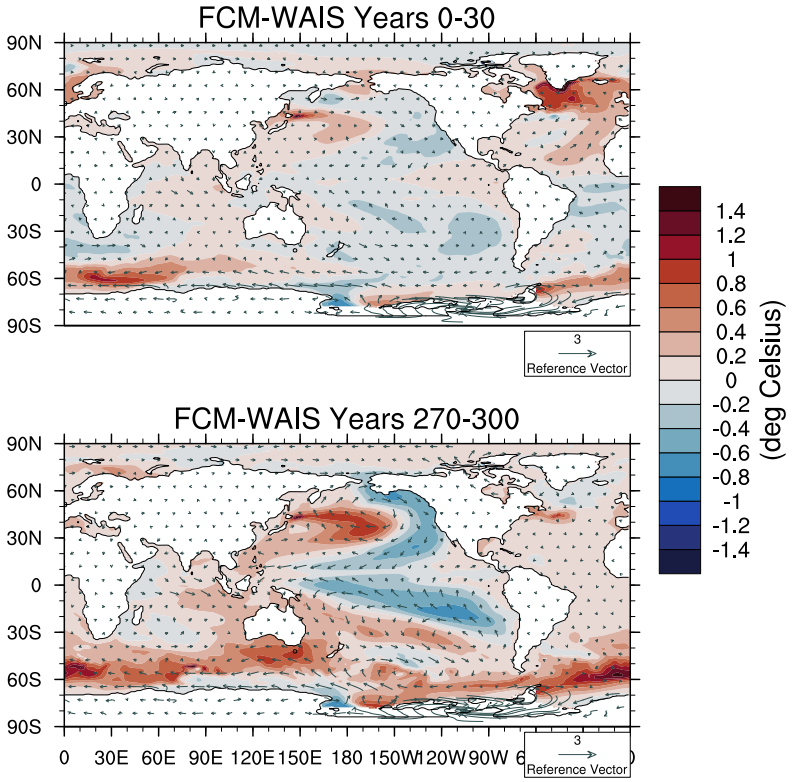

Figure 4.6: Global sea surface temperature anomalies for the first 30 years (top) and last 30 years (bottom) of FCM-WAIS. Wind anomalies are shown as vectors.

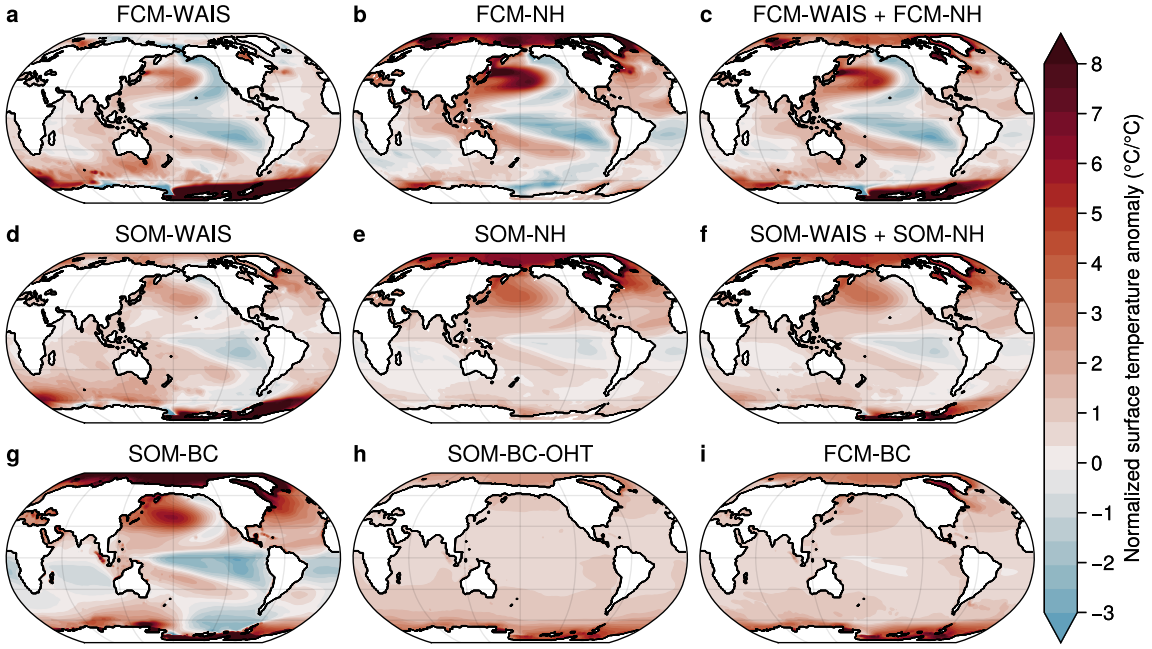

Figure 4.7: As in Fig. 4.2, but normalized by global mean surface temperature anomaly.

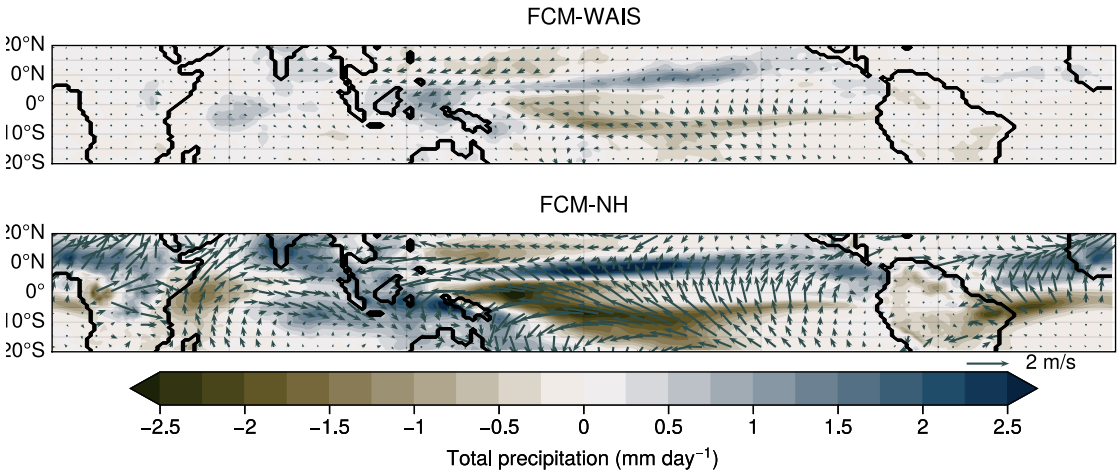

Figure 4.8: Tropical precipitation and wind anomalies for the last 30 years of FCM-WAIS (top) and FCM-NH (bottom).

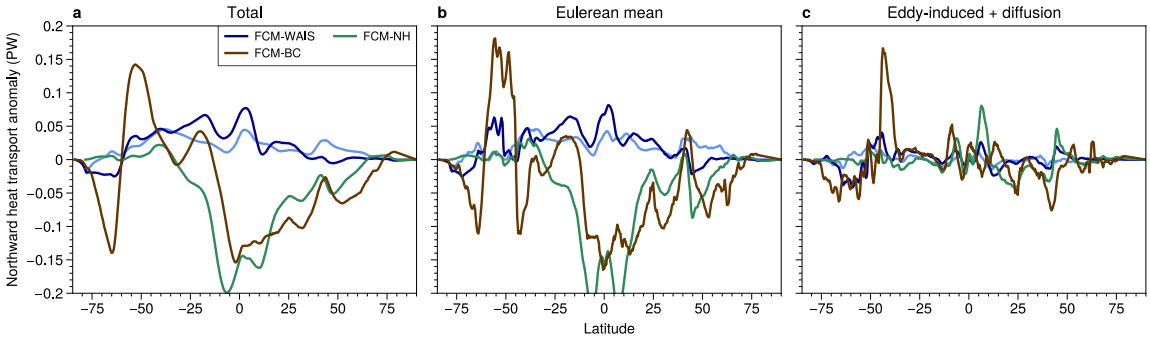

Figure 4.9: Total northward heat transport anomaly for each simulation as in Fig. 4.4 (a), and its decomposition into Eulerian mean (b) and eddy components (c).

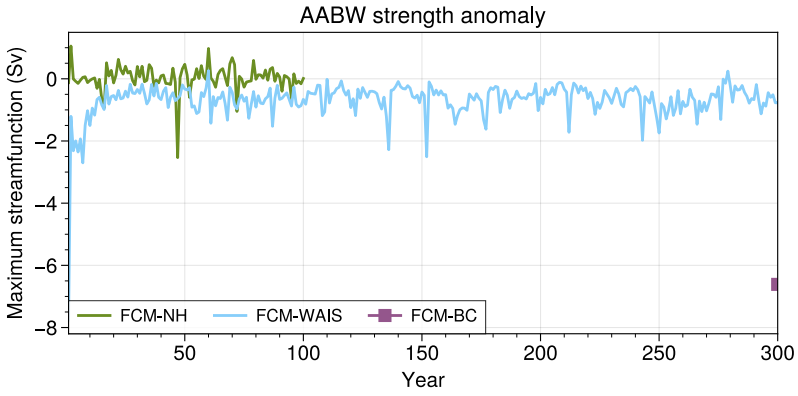

Figure 4.10: Antarctic Bottom Water (AABW) formation rate (Sv) anomalies for FCM-WAIS (blue) and FCM-NH (green), with the time-mean formation rate anomaly for FCM-BC also shown (purple square) (note that the average is taken over the last 50 years of the 400 year FCM-BC simulation). AABW formation rate is defined as the minimum in the total meridional overturning streamfunction (MOC) found south of 60°S.

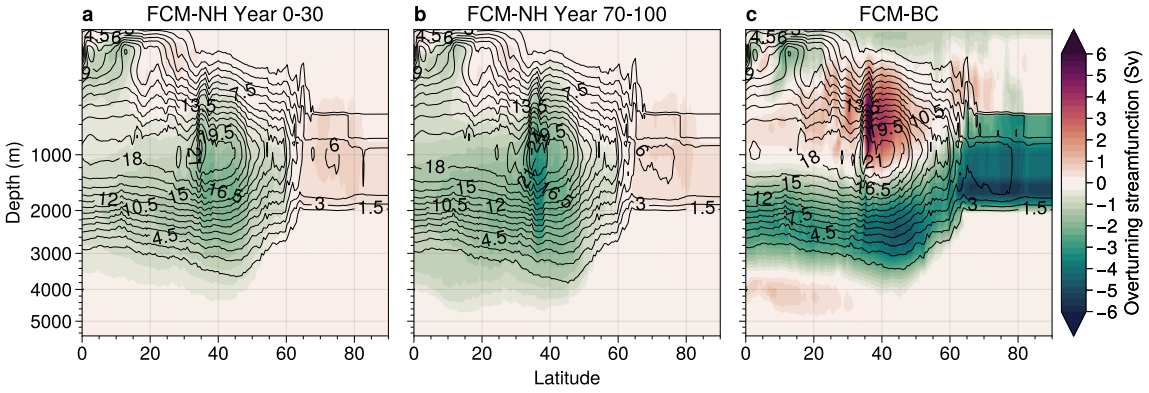

Figure 4.11: AMOC anomalies (filled contours) for the first and last 30 years of FCM-NH, and the last 50 years of FCM-BC, with preindustrial AMOC overlain (contour lines).

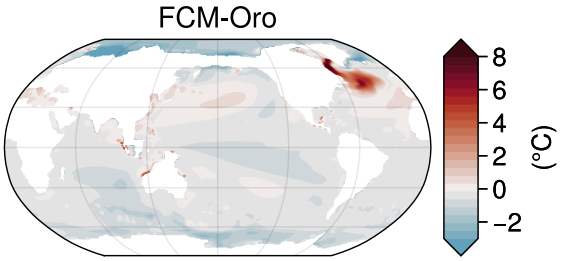

Figure 4.12: Sea surface temperature anomaly associated with orographic changes of the mPWP (excluding ice sheet changes) (FCM-Oro, shown also in Chapter 3, Fig. 3.18; reproduced from Feng et al. (2022)).

Chapter 5

CONCLUSIONS

In this thesis, I set out to examine multiple timescales of future climate change, from decades to millenia, within the framework of forcings and feedbacks. In Chapter 2, I used a simple energy balance model that combined the most up-to-date probability distributions of historical forcing, energy imbalance, and the global radiative feedback to estimate the magnitude of future warming expected upon a cessation of emissions. I found that, due to the cooling effect of aerosols in the atmosphere, there exists a geophysical commitment to additional warming that can persist for decades after emissions cease.

In chapter 3, I turned my attention to longer timescales of climate change, over which evolving spatial patterns of warming are expected to change the value of the global radiative feedback, such that the climate is expected to become more sensitive to emissions. I looked toward the mid-Pliocene Warm Period (mPWP) as an example of a past equilibrated climate state that has served as an analogue for future warming, and as a constraint on climate sensitivity. By separating and quantifying the forcings and feedbacks operating in the mPWP in a state-of-the-art GCM, I found that the spatial pattern of warming in the mPWP implied a dynamical climate response to paleoenvironmental boundary conditions that are not relevant to end-of-century warming, but which may be relevant to warming over hundreds to thousands of years. The implication is that there exists a potential for a reduction in our estimate of modern-day ECS that is constrained by this paleoclimate – but an increase in our estimate of ESS.

In chapter 4, I probed the causal mechanisms for the spatial pattern of warming in the mPWP by investigating the coupled climate response to a key feature of this paleoclimate: the absence of the West Antarctic Ice Sheet (WAIS). By comparing the response to a loss of WAIS to that invoked by the vegetation and Greenland Ice Sheet changes of the mPWP, I found that the removal of the ice sheet, despite exerting minimal radiative forcing on the

climate, results in continued warming of the Southern Ocean as enhanced high latitude ocean heat transport drives a positive sea ice-albedo feedback. These single forcing experiments revealed that high southern latitude ocean heat transport change is a key driver of the Southern Ocean warming, and enhanced climate sensitivity, of the mPWP. The results imply a particular sensitivity to the ice sheet, with relevance to future global warming on millenial timescales.

Some questions, however, remain. It is reasonable to expect that freshwater fluxes resulting from ice sheet melt would affect the transient response to a loss of the WAIS by cooling, temporarily, the surface ocean. In addition, a complete reduction of the ice sheet as I have modeled here would realistically occur only with GHG concentrations at least as high as the present day ($\sim$400ppm), and examining the coupled response to the ice sheet in both a warmer world, and with freshwater fluxes, would further improve the relevance of this work to projections of future global warming.

BIBLIOGRAPHY

Allen, M., H. de Coninck, O. Dube, and Coauthors, 2018: Technical Summary. *Global Warming of 1.5°C. An IPCC Special Report on the impacts of global warming of 1.5°C above pre-industrial levels and related global greenhouse gas emission pathways, in the context of strengthening the global response to the threat of climate change, sustainable development, and efforts to eradicate poverty*, V. Masson-Delmotte, P. Zhai, H.-O. Portner et al., Eds.

Allen, M. R., D. J. Frame, C. Huntingford, C. D. Jones, J. A. Lowe, M. Meinshausen, and N. Meinshausen, 2009: Warming caused by cumulative carbon emissions towards the trillionth tonne. *Nature*, **458 (7242)**, 1163–1166, https://doi.org/10.1038/nature08019.

Alley, R. B., S. Anandakrishnan, K. Christianson, H. J. Horgan, A. Muto, B. R. Parizek, D. Pollard, and R. T. Walker, 2015: Oceanic forcing of ice-sheet retreat: West Antarctica and more. *Annual Review of Earth and Planetary Sciences*, **43 (1)**, 207–231.

Andrews, T., J. M. Gregory, and M. J. Webb, 2015: The dependence of radiative forcing and feedback on evolving patterns of surface temperature change in climate models. *J. Climate*, **28 (4)**, 1630–1648.

Andrews, T., C. J. Smith, G. Myhre, P. M. Forster, R. Chadwick, and D. Ackerley, 2021: Effective radiative forcing in a GCM with fixed surface temperatures. *J. Geophys. Res. Atmos.*, **126 (4)**, https://doi.org/10.1029/2020JD033880.

Andrews, T., and Coauthors, 2018: Accounting for changing temperature patterns increases historical estimates of climate sensitivity. *Geophys. Res. Lett.*, **45 (16)**, 8490–8499.

Andrews, T., and Coauthors, 2022: On the effect of historical SST patterns on radiative feedback. *J. Geophys. Res. Atmos.*, **127 (18)**, https://doi.org/10.1029/2022JD036675.

Annan, J. D., J. C. Hargreaves, T. Mauritsen, E. McClymont, and S. L. Ho, 2024: Can we reliably reconstruct the mid-Pliocene Warm Period with sparse data and uncertain models? *Climate of the Past*, **20 (9)**, 1989–1999.

Armour, K. C., 2017: Energy budget constraints on climate sensitivity in light of inconstant climate feedbacks. *Nature Climate Change*, **7 (5)**, 331–335, https://doi.org/10.1038/nclimate3278.

Armour, K. C., C. M. Bitz, and G. H. Roe, 2013: Time-varying climate sensitivity from regional feedbacks. *J. Climate*, **26 (13)**, 4518–4534, https://doi.org/10.1175/JCLI-D-12-00544.1.

Armour, K. C., J. Marshall, J. R. Scott, A. Donohoe, and E. R. Newsom, 2016: Southern Ocean warming delayed by circumpolar upwelling and equatorward transport. *Nat. Geosci.*, **9 (7)**, 549–554.

Armour, K. C., and G. H. Roe, 2011: Climate commitment in an uncertain world. *Geophys. Res. Lett.*, **38**, https://doi.org/10.1029/2011GL048739.

Baatsen, M. L., A. S. von der Heydt, M. A. Kliphuis, A. M. Oldeman, and J. E. Weiffenbach, 2021: Warm mid-Pliocene conditions without high climate sensitivity: the CCSM4-Utrecht (CESM 1.0.5) contribution to the PlioMIP2. *Climate of the Past Discuss.*, **2021**, 1–30, https://doi.org/10.5194/cp-18-657-2022, 2022.

Bellouin, N., J. Quaas, E. Gryspeerdt, S. Kinne, P. Stier, D. Watson-Parris, O. Boucher, and Coauthors, 2020: Bounding global aerosol radiative forcing of climate change. *Rev. Geophys.*, **58 (1)**, https://doi.org/10.1029/2019RG000660.

Bjordal, J., T. Storelvmo, K. Alterskjær, and T. Carlsen, 2020: Equilibrium Climate Sensitivity above 5C plausible due to state-dependent cloud feedback. *Nat. Geosci.*, **13 (11)**, 718–721.

Bloch-Johnson, J., M. Rugenstein, M. B. Stolpe, T. Rohrschneider, Y. Zheng, and J. M. Gregory, 2021: Climate sensitivity increases under higher CO_2 levels due to feedback temperature dependence. *Geophys. Res. Lett.*, **48 (4)**.

Bloch-Johnson, J., and Coauthors, 2024: The Green's Function Model Intercomparison Project (GFMIP) protocol. *J. Adv. Model. Earth Syst.*, **16 (2)**.

Bonan, D., K. Armour, G. Roe, N. Siler, and N. Feldl, 2018: Sources of uncertainty in the meridional pattern of climate change. *Geophys. Res. Lett.*, **45 (17)**, 9131–9140.

Bronselaer, B., M. Winton, S. M. Griffies, W. J. Hurlin, K. B. Rodgers, O. V. Sergienko, R. J. Stouffer, and J. L. Russell, 2018: Change in future climate due to Antarctic meltwater. *Nature*, **564 (7734)**, 53–58.

Burke, K. D., J. W. Williams, M. A. Chandler, A. M. Haywood, D. J. Lunt, and B. L. Otto-Bliesner, 2018: Pliocene and Eocene provide best analogs for near-future climates. *Proc. Natl. Acad. Sci. (USA)*, **115 (52)**, 13,288–13,293, https://doi.org/10.1073/pnas.1809600115.

Burls, N., and A. Fedorov, 2014: Simulating Pliocene warmth and a permanent El Niño-like state: The role of cloud albedo. *Paleoceanography*, **29 (10)**, 893–910.

Burton, L. E., and Coauthors, 2023: On the climatic influence of CO_2 forcing in the Pliocene. *Climate of the Past Discuss.*, **19**, 1–28, https://doi.org/10.5194/cp-19-747-2023.

Caballero, R., and M. Huber, 2013: State-dependent climate sensitivity in past warm climates and its implications for future climate projections. *Proc. Natl. Acad. Sci. (USA)*, **110 (35)**, 14 162–14 167.

Canadell, J. G., P. Monteiro, M. Costa, and Coauthors, 2021: Global Carbon and other Biogeochemical Cycles and Feedbacks. *Climate Change 2021: The Physical Science Basis. Contribution of Working Group I to the Sixth Assessment Report of the Intergovernmental Panel on Climate Change*, V. Masson-Delmotte, P. Zhai, A. Pirani et al., Eds., Cambridge University Press. In Press.

Ceppi, P., and J. M. Gregory, 2017: Relationship of tropospheric stability to climate sensitivity and Earth's observed radiation budget. *Proc. Natl. Acad. Sci. (USA)*, **114 (50)**, 13,126–13,131.

Chandan, D., and W. R. Peltier, 2017: Regional and global climate for the mid-Pliocene using the University of Toronto version of CCSM4 and plioMIP2 boundary conditions. *Climate of the Past*, **13 (7)**, 919–942, https://doi.org/10.5194/cp-13-919-2017.

Chandan, D., and W. R. Peltier, 2018: On the mechanisms of warming the mid-Pliocene and the inference of a hierarchy of climate sensitivities with relevance to the understanding of climate futures. *Climate of the Past*, **14 (6)**, 825–856, https://doi.org/10.5194/cp-14-825-2018.

Chemke, R., L. M. Polvani, J. E. Kay, and C. Orbe, 2021: Quantifying the role of ocean coupling in Arctic amplification and sea-ice loss over the 21st century. *Npj Climate Atmos. Sci.*, **4 (1)**, 46, https://doi.org/10.1038/s41612-021-00204-8.

Chen, D., M. Rojas, B. Samset, and Coauthors, 2021: Framing, Context, and Methods. *Climate Change 2021: The Physical Science Basis. Contribution of Working Group I to the Sixth Assessment Report of the Intergovernmental Panel on Climate Change*, V. Masson-Delmotte, P. Zhai, A. Pirani et al., Eds., Cambridge University Press. In Press.

Collins, M., R. Knutti, J. Arblaster, and Coauthors, 2013: Long-term Climate Change: Projections, Commitments and Irreversibility. *Climate Change 2013: The Physical Science Basis. Contribution of Working Group I to the Fifth Assessment Report of the Intergovernmental Panel on Climate Change*, T. Stocker, D. Qin, G.-K. Plattner et al., Eds., Cambridge University Press, Cambridge, United Kingdom and New York, NY, USA.

Cooper, V. T., and Coauthors, 2024: Last Glacial Maximum pattern effects reduce climate sensitivity estimates. *Sci. Adv.*, **10 (16)**.

Danabasoglu, G., and Coauthors, 2020: The Community Earth System Model version 2 (CESM2). *J. Adv. Model. Earth Syst.*, **12 (2)**, https://doi.org/10.1029/2019MS001916.

Davis, I., and B. Medeiros, 2024: Assessing CESM2 clouds and their response to climate change using cloud regimes. *J. Climate*, **37 (10)**, 2965–2985.

Dong, Y., K. C. Armour, D. S. Battisti, and E. Blanchard-Wrigglesworth, 2022: Two-way teleconnections between the Southern Ocean and the tropical Pacific via a dynamic feedback. *J. Climate*, **35 (19)**, 6267–6282, https://doi.org/10.1175/JCLI-D-22-0080.1.

Dong, Y., K. C. Armour, M. D. Zelinka, C. Proistosescu, D. S. Battisti, C. Zhou, and T. Andrews, 2020: Intermodel spread in the pattern effect and its contribution to climate sensitivity in CMIP5 and CMIP6 models. *J. Climate*, **33 (18)**, 7755–7775.

Dong, Y., C. Proistosescu, K. C. Armour, and D. S. Battisti, 2019: Attributing historical and future evolution of radiative feedbacks to regional warming patterns using a Green's function approach: The preeminence of the western Pacific. *J. Climate*, **32 (17)**, 5471–5491, https://doi.org/10.1175/JCLI-D-18-0843.1.

Dowsett, H., and Coauthors, 2016: The PRISM4 (mid-Piacenzian) paleoenvironmental reconstruction. *Climate of the Past*, **12 (7)**, 1519–1538, https://doi.org/10.5194/cp-12-1519-2016.

Dvorak, M., 2022a: Data for "Estimating the timing of geophysical commitment to 1.5 and 2.0°C". Zenodo, https://doi.org/10.5281/zenodo.6456363.

Dvorak, M., 2022b: Methods and results for "Estimating the timing of geophysical commitment to 1.5 and 2.0°C". GitHub, https://doi.org/10.5281/zenodo.6455705.

Dvorak, M., K. C. Armour, R. Feng, V. T. Cooper, J. Zhu, N. Burls, and C. Proistosescu, 2025: Mid-Pliocene climate forcing, sea surface temperature patterns, and implications for modern-day climate sensitivity. *J. Climate*, **38 (13)**, 3037–3053.

Ehlert, D., and K. Zickfeld, 2017: What determines the warming commitment after cessation of CO_2 emissions? *Environ. Res. Lett.*, **12 (1)**, 015 002, https://doi.org/10.1088/1748-9326/aa564a.

Eyring, V., S. Bony, G. A. Meehl, C. A. Senior, B. Stevens, R. J. Stouffer, and K. E. Taylor, 2016: Overview of the Coupled Model Intercomparison Project Phase 6 (CMIP6) experimental design and organization. *Geosci. Model Dev.*, **9 (5)**, 1937–1958, https://doi.org/10.5194/gmd-9-1937-2016.

Feng, R., B. L. Otto-Bliesner, E. C. Brady, and N. Rosenbloom, 2020: Increased climate response and Earth System Sensitivity from CCSM4 to CESM2 in mid-Pliocene simulations. *J. Adv. Model. Earth Syst.*, **12 (8)**, https://doi.org/10.1029/2019MS002033.

Feng, R., B. L. Otto-Bliesner, T. L. Fletcher, C. R. Tabor, A. P. Ballantyne, and E. C. Brady, 2017: Amplified Late Pliocene terrestrial warmth in northern high latitudes from greater radiative forcing and closed Arctic Ocean gateways. *Earth Planet. Sci. Lett.*, **466**, 129–138, https://doi.org/10.1016/j.epsl.2017.03.006.

Feng, R., and Coauthors, 2022: Past terrestrial hydroclimate sensitivity controlled by Earth system feedbacks. *Nat. Comm.*, **13 (1)**, 1306, https://doi.org/10.1038/s41467-022-28814-7.

Forster, P., and Coauthors, 2021: The Earth's Energy Budget, Climate Feedbacks, and Climate Sensitivity. *Climate Change 2021: The Physical Science Basis. Contribution of Working Group I to the Sixth Assessment Report of the Intergovernmental Panel on Climate Change*, Cambridge University Press, 923–1054, https://doi.org/10.1017/9781009157896.009.

Forster, P. M., and Coauthors, 2016: Recommendations for diagnosing effective radiative forcing from climate models for CMIP6. *J. Geophys. Res. Atmos.*, **121 (20)**, 12–460, https://doi.org/10.1002/2016JD025320.

Frölicher, T. L., M. Winton, and J. L. Sarmiento, 2014: Continued global warming after CO_2 emissions stoppage. *Nature Climate Change*, **4 (1)**, 40–44, https://doi.org/10.1038/nclimate2060.

Geoffroy, O., D. Saint-Martin, D. J. L. Olivié, A. Voldoire, G. Bellon, and S. Tytéca, 2013: Transient Climate Response in a two-layer energy-balance model. Part I: Analytical solution and parameter calibration using CMIP5 AOGCM experiments. *J. Climate*, **26 (6)**, 1841 – 1857, https://doi.org/10.1175/JCLI-D-12-00195.1.

Gettelman, A., and Coauthors, 2019: High climate sensitivity in the Community Earth System Model version 2 (CESM2). *Geophys. Res. Lett.*, **46 (14)**, 8329–8337.

Golledge, N. R., E. D. Keller, N. Gomez, K. A. Naughten, J. Bernales, L. D. Trusel, and T. L. Edwards, 2019: Global environmental consequences of twenty-first-century ice-sheet melt. *Nature*, **566 (7742)**, 65–72.

Goodwin, P., R. G. Williams, and A. Ridgwell, 2015: Sensitivity of climate to cumulative carbon emissions due to compensation of ocean heat and carbon uptake. *Nature Geosci.*, **8 (1)**, 29–34, https://doi.org/10.1038/ngeo2304.

Goosse, H., and Coauthors, 2018: Quantifying climate feedbacks in polar regions. *Nature Comm.*, **9 (1)**, 1919, https://doi.org/10.1038/s41467-018-04173-0.

Green, B., and J. Marshall, 2017: Coupling of trade winds with ocean circulation damps ITCZ shifts. *J. Climate*, **30 (12)**, 4395–4411.

Gregory, J. M., and Coauthors, 2004: A new method for diagnosing radiative forcing and climate sensitivity. *Geophys. Res. Lett.*, **31 (3)**, https://doi.org/10.1029/2003GL018747.

Hansen, J., and Coauthors, 2005: Efficacy of climate forcings. *J. Geophys. Res. Atmos.*, **110 (D18)**, https://doi.org/10.1029/2005JD005776.

Hansen, J. E., and Coauthors, 2023: Global warming in the pipeline. *Oxford Open Climate Change*, **3 (1)**, https://doi.org/10.1093/oxfclm/kgad008.

Hare, B., and M. Meinshausen, 2006: How much warming are we committed to and how much can be avoided? *Climatic Change*, **75 (1)**, 111–149, https://doi.org/10.1007/s10584-005-9027-9.

Hartmann, D. L., 2022: The Antarctic ozone hole and the pattern effect on climate sensitivity. *Proc. Natl. Acad. Sci. (USA)*, **119 (35)**, https://doi.org/10.1073/pnas.2207889119.

Haywood, A. M., and Coauthors, 2013: Large-scale features of Pliocene climate: results from the Pliocene Model Intercomparison Project. *Climate of the Past*, **9**, https://doi.org/10.5194/cp-9-191-2013.

Haywood, A. M., and Coauthors, 2016: The Pliocene Model Intercomparison Project (PlioMIP) Phase 2: Scientific objectives and experimental design. *Climate of the Past*, **12 (3)**, 663–675, https://doi.org/10.5194/cp-12-663-2016.

Haywood, A. M., and Coauthors, 2020: The Pliocene Model Intercomparison Project Phase 2: Large-scale climate features and climate sensitivity. *Climate of the Past*, **16**, 2095–2123, https://doi.org/10.5194/cp-9-191-2013.

Haywood, A. M., and Coauthors, 2024: Pliocene Model Intercomparison Project Phase 3 (PlioMIP3)–science plan and experimental design. *Global and Planetary Change*, **232**, 104 316.

Held, I. M., M. Winton, K. Takahashi, T. Delworth, F. Zeng, and G. K. Vallis, 2010: Probing the fast and slow components of global warming by returning abruptly to preindustrial forcing. *J. Climate*, **23 (9)**, 2418 – 2427, https://doi.org/10.1175/2009JCLI3466.1.

Holloway, M. D., L. C. Sime, J. S. Singarayer, J. C. Tindall, P. Bunch, and P. J. Valdes, 2016: Antarctic Last Interglacial isotope peak in response to sea ice retreat not ice-sheet collapse. *Nature Comm.*, **7 (1)**, 12 293.

Hu, A., G. A. Meehl, W. Han, B. Otto-Bliestner, A. Abe-Ouchi, and N. Rosenbloom, 2015: Effects of the Bering Strait closure on AMOC and global climate under different background climates. *Prog. Oceanogr.*, **132**, 174–196.

IPCC, 2021: Summary for Policymakers. *Climate Change 2021: The Physical Science Basis. Contribution of Working Group I to the Sixth Assessment Report of the Intergovernmental Panel on Climate Change*, V. Masson-Delmotte, P. Zhai, A. Pirani et al., Eds., Cambridge University Press. In Press.

Jones, C. D., T. M. Frolicher, C. Koven, and Coauthors, 2019: The Zero Emissions Commitment Model Intercomparison Project (ZECMIP) contribution to C4MIP: quantifying committed climate changes following zero carbon emissions. *Geosci. Model Dev.*, **12**, 4375 – 4385, https://doi.org/10.5194/gmd-12-4375-2019.

Joughin, I., B. E. Smith, and B. Medley, 2011: Marine ice sheet collapse potentially under way for the Thwaites. *Environ. Sci*, **2**, 403–406.

Justino, F., A. Silva, M. Pereira, F. Stordal, D. Lindemann, and F. Kucharski, 2015: The large-scale climate in response to the retreat of the West Antarctic Ice Sheet. *J. Climate*, **28 (2)**, 637–650.

Kang, S., P. Ceppi, Y. Yu, and I. Kang, 2023a: Recent global climate feedback controlled by Southern Ocean cooling. *Nat. Geosci.*, **16**, 775–780.

Kang, S. M., I. M. Held, D. M. Frierson, and M. Zhao, 2008: The response of the ITCZ to extratropical thermal forcing: Idealized slab-ocean experiments with a GCM. *J. Climate*, **21 (14)**, 3521–3532.

Kang, S. M., Y. Yu, C. Deser, X. Zhang, I.-S. Kang, S.-S. Lee, K. B. Rodgers, and P. Ceppi, 2023b: Global impacts of recent Southern Ocean cooling. *Proc. Natl. Acad. Sci. (USA)*, **120 (30)**, https://doi.org/10.1073/pnas.2300881120.

Kaplan, M. R., and Coauthors, 2017: Middle to Late Pleistocene stability of the central East Antarctic Ice Sheet at the head of Law Glacier. *Geology*, **45 (8)**, 743–746, https://doi.org/10.1130/G39189.1.

Kim, H., S. M. Kang, J. E. Kay, and S.-P. Xie, 2022: Subtropical clouds key to Southern Ocean teleconnections to the tropical Pacific. *Proc. Natl. Acad. Sci. (USA)*, **119**, https://doi.org/10.1073/pnas.2200514119.

Knutti, R., and M. A. Rugenstein, 2015: Feedbacks, climate sensitivity and the limits of linear models. *Phil. Trans. R. Soc. A*, **373 (2054)**.

Lee, J.-Y., J. Marotzke, G. Bala, and Coauthors, 2021: Future Global Climate: Scenario-Based Projections and Near-Term Information. *Climate Change 2021: The Physical Science Basis. Contribution of Working Group I to the Sixth Assessment Report of the Intergovernmental Panel on Climate Change*, V. [Masson-Delmotte, P. Zhai, A. Pirani, and others], Eds., Cambridge University Press. In Press.

Li, D., R. M. DeConto, D. Pollard, and Y. Hu, 2024: Competing climate feedbacks of ice sheet freshwater discharge in a warming world. *Nature Comm.*, **15 (1)**, 5178.

Lunt, D. J., D. Chandan, A. M. Haywood, G. M. Lunt, J. C. Rougier, U. Salzmann, G. A. Schmidt, and P. J. Valdes, 2021: Multi-variate factorisation of numerical simulations. *Geosci. Model Dev.*, **14 (7)**, 4307–4317.

Lunt, D. J., A. M. Haywood, G. A. Schmidt, U. Salzmann, P. J. Valdes, and H. J. Dowsett, 2010: Earth System Sensitivity inferred from Pliocene modelling and data. *Nat. Geosci.*, **3 (1)**, 60–64.

Lunt, D. J., A. M. Haywood, G. A. Schmidt, U. Salzmann, P. J. Valdes, H. J. Dowsett, and C. A. Loptson, 2012: On the causes of mid-Pliocene warmth and polar amplification. *Earth and Planetary Science Letters*, **321**, 128–138.

Lunt, D. J., and Coauthors, 2013: A multi-model assessment of Last Interglacial temperatures. *Climate of the Past*, **9 (2)**, 699–717.

Luongo, M. T., S.-P. Xie, and I. Eisenman, 2022: Buoyancy forcing dominates the cross-equatorial ocean heat transport response to Northern Hemisphere extratropical cooling. *J. Climate*, **35 (20)**, 6671–6690.

MacDougall, A. H., 2021: Estimated effect of the permafrost carbon feedback on the Zero Emissions Commitment to climate change. *Biogeosciences*, **18 (17)**, 4937–4952, https://doi.org/10.5194/bg-18-4937-2021.

MacDougall, A. H., and P. Friedlingstein, 2015: The origin and limits of the near proportionality between climate warming and cumulative CO_2 emissions. *J. Climate*, **28 (10)**, 4217 – 4230, https://doi.org/10.1175/JCLI-D-14-00036.1.

MacDougall, A. H., and Coauthors, 2020: Is there warming in the pipeline? a multi-model analysis of the Zero Emissions Commitment from CO_2. *Biogeosciences*, **17 (11)**, 2987–3016, https://doi.org/10.5194/bg-17-2987-2020.

Martínez-Botí, M. A., and Coauthors, 2015: Plio-Pleistocene climate sensitivity evaluated using high-resolution CO_2 records. *Nature*, **518 (7537)**, 49–54.

Matthews, H., and K. Zickfeld, 2012: Climate response to zeroed emissions of greenhouse gases and aerosols. *Nature Climate Change*, **2 (5)**, 338 – 341, https://doi.org/10.1038/nclimate1424.

Matthews, H. D., N. P. Gillett, P. A. Stott, and K. Zickfeld, 2009: The proportionality of global warming to cumulative carbon emissions. *Nature*, **459 (7248)**, 829–832, https://doi.org/10.1038/nature08047.

Matthews, H. D., and Coauthors, 2020: Opportunities and challenges in using remaining carbon budgets to guide climate policy. *Nature Geosci.*, **13 (12)**, 769–779, https://doi.org/10.1038/s41561-020-00663-3.

Mauritsen, T., and R. Pincus, 2017: Committed warming inferred from observations. *Nature Climate Change*, **7 (9)**, 652–655, https://doi.org/10.1038/nclimate3357.

McClymont, E. L., and Coauthors, 2020: Lessons from a high CO_2 world: an ocean view from ∼3 million years ago. *Climate of the Past Discuss.*, **2020**, 1–27, https://doi.org/10.5194/cp-16-1599-2020.

Meehl, G. A., and Coauthors, 2020: Characteristics of future warmer base states in CESM2. *Earth and Space Science*, **7 (9)**.

Meinshausen, M., and Coauthors, 2011: The RCP greenhouse gas concentrations and their extensions from 1765 to 2300. *Climatic Change*, **109 (1)**, 213, https://doi.org/10.1007/s10584-011-0156-z.

Millar, R. J., Z. R. Nicholls, P. Friedlingstein, and M. R. Allen, 2017: A modified impulse-response representation of the global near-surface air temperature and atmospheric concentration response to carbon dioxide emissions. *Atmospheric Chemistry and Physics*, **17 (11)**, 7213–7228, https://doi.org/10.5194/acp-17-7213-2017.

Morice, C. P., J. J. Kennedy, N. A. Rayner, and P. D. Jones, 2012: Quantifying uncertainties in global and regional temperature change using an ensemble of observational estimates: the HadCRUT4 data set. *J. Geophys. Res. Atmos.*, **117 (D8)**, https://doi.org/10.1029/2011JD017187.

NOAA, 2020: *National Oceanic and Atmospheric Administration (NOAA) Global Monitoring Laboratory. Trends in Atmospheric Carbon Dioxide: Mauna Loa CO_2 Annual Mean Data*, URL `https://gml.noaa.gov/webdata/ccgg/trends/co2/co2_annmean_mlo.txt`.

O'Connor, G. K., Y. Nakayama, E. J. Steig, S. Hyogo, L. Thompson, and K. Armour, 2024: Influence of local wind patterns on Circumpolar Deep Water transport in the Amundsen Sea Embayment, West Antarctica. *American Geophysical Union, Ocean Sciences Meeting*, 2647.

Otto-Bliesner, B. L., A. Jahn, R. Feng, E. C. Brady, A. Hu, and M. Löfverström, 2016: Amplified North Atlantic warming in the late Pliocene by changes in Arctic gateways. *Geophys. Res. Lett.*, **44 (2)**, 957–964.

Otto-Bliesner, B. L., N. Rosenbloom, E. J. Stone, N. P. McKay, D. J. Lunt, E. C. Brady, and J. T. Overpeck, 2013: How warm was the Last Interglacial? New model–data comparisons. *Phil. Trans. R. Soc. A*, **371 (2001)**.

PALEOSENS, 2012: Making sense of palaeoclimate sensitivity. *Nature*, **491 (7426)**, 683–691.

Pauling, A. G., C. M. Bitz, and E. J. Steig, 2023: Linearity of the climate system response to raising and lowering West Antarctic and coastal Antarctic topography. *J. Climate*, **36 (18)**, 6195–6212.

Pausata, F. S., L. Chafik, R. Caballero, and D. S. Battisti, 2015: Impacts of high-latitude volcanic eruptions on ENSO and AMOC. *Proc. Natl. Acad. Sci. (USA)*, **112 (45)**, 13 784–13 788.

Pincus, R., P. M. Forster, and B. Stevens, 2016: The Radiative Forcing Model Intercomparison Project (RFMIP): Experimental protocol for CMIP6. *Geosci. Model Dev.*, **9**, https://doi.org/10.5194/gmd-9-3447-2016.

Poletti, A., D. Frierson, and K. Armour, 2024: Why do CO_2 quadrupling simulations warm more than twice as much as CO_2 doubling simulations in CMIP6? *Geophys. Res. Lett.*, **51 (10)**.

Pritchard, H., S. R. Ligtenberg, H. A. Fricker, D. G. Vaughan, M. R. van den Broeke, and L. Padman, 2012: Antarctic ice-sheet loss driven by basal melting of ice shelves. *Nature*, **484 (7395)**, 502–505.

Pritchard, H. D., and Coauthors, 2025: Bedmap3 updated ice bed, surface and thickness gridded datasets for Antarctica. *Scientific Data*, **12 (1)**, 414.

Reese, R., and Coauthors, 2023: The stability of present-day Antarctic grounding lines–Part 2: Onset of irreversible retreat of Amundsen Sea glaciers under current climate on centennial timescales cannot be excluded. *The Cryosphere*, **17 (9)**, 3761–3783.

Riahi, K., D. P. van Vuuren, E. Kriegler, and Coauthors, 2017: The Shared Socioeconomic Pathways and their energy, land use, and greenhouse gas emissions implications: an overview. *Global Environmental Change*, **42**, 153 – 168, https://doi.org/10.1016/j.gloenvha.2016.05.009.

Rignot, E., J. Mouginot, M. Morlighem, H. Seroussi, and B. Scheuchl, 2014: Widespread, rapid grounding line retreat of Pine Island, Thwaites, Smith, and Kohler glaciers, West Antarctica, from 1992 to 2011. *Geophys. Res. Lett.*, **41 (10)**, 3502–3509.

Rogelj, J., P. M. Forster, E. Kriegler, C. J. Smith, and R. Séférian, 2019: Estimating and tracking the remaining carbon budget for stringent climate targets. *Nature*, **571 (7765)**, 335–342, https://doi.org/10.1038/s41586-019-1368-z.

Rugenstein, M. A. A., and K. C. Armour, 2021: Three flavors of radiative feedbacks and their implications for estimating Equilibrium Climate Sensitivity. *Geophys. Res. Lett.*, **48**, https://doi.org/10.1029/2021GL092983.

Rugenstein, M. A. A., J. Sedláček, and R. Knutti, 2016: Nonlinearities in patterns of long-term ocean warming. *Geophys. Res. Lett.*, **43 (7)**, 3380–3388, https://doi.org/10.1002/2016GL068041.

Ruppel, C. D., and J. D. Kessler, 2017: The interaction of climate change and methane hydrates. *Rev. Geophys.*, **55 (1)**, 126–168, https://doi.org/https://doi.org/10.1002/2016RG000534.

Schmidtko, S., K. J. Heywood, A. F. Thompson, and S. Aoki, 2014: Multidecadal warming of Antarctic waters. *Science*, **346 (6214)**, 1227–1231.

Seroussi, H., and Coauthors, 2024: Evolution of the Antarctic Ice Sheet over the next three centuries from an ISMIP6 model ensemble. *Earth's Future*, **12 (9)**.

Sherwood, S. C., and Coauthors, 2020: An assessment of Earth's climate sensitivity using multiple lines of evidence. *Rev. Geophys.*, **58 (4)**, https://doi.org/10.1029/2019RG000678.

Silvers, L. G., D. Paynter, and M. Zhao, 2018: The diversity of cloud responses to twentieth century sea surface temperatures. *Geophys. Res. Lett.*, **45 (1)**, 391–400, https://doi.org/10.1002/2017GL075583.

Smith, C., Z. Nicholls, K. Armour, and Coauthors, 2021: The Earth's Energy Budget, Climate Feedbacks, and Climate Sensitivity Supplementary Material. *Climate Change 2021: The Physical Science Basis. Contribution of Working Group I to the Sixth Assessment Report of the Intergovernmental Panel on Climate Change*, V. [Masson-Delmotte, P. Zhai, A. Pirani, and others], Eds.

Smith, C. J., P. M. Forster, M. Allen, J. Fuglestvedt, R. J. Millar, J. Rogelj, and K. Zickfeld, 2019: Current fossil fuel infrastructure does not yet commit us to 1.5 °C warming. *Nature Comm.*, **10 (1)**, 101, https://doi.org/10.1038/s41467-018-07999-w.

Smith, C. J., P. M. Forster, M. Allen, N. Leach, R. J. Millar, G. A. Passerello, and L. A. Regayre, 2018: FAIR v1.3: A simple emissions-based impulse response and carbon cycle

model. *Geosci. Model Dev.*, **11 (6)**, 2273–2297, https://doi.org/10.5194/gmd-11-2273-2018.

Smith, C. J., and Coauthors, 2020: Effective radiative forcing and adjustments in CMIP6 models. *Atmos. Chem. Phys.*, **20 (16)**, 9591–9618.

Soden, B. J., A. J. Broccoli, and R. S. Hemler, 2004: On the use of cloud forcing to estimate cloud feedback. *J. Climate*, **17 (19)**, 3661–3665.

Solomon, S., G.-K. Plattner, R. Knutti, and P. Friedlingstein, 2009: Irreversible climate change due to carbon dioxide emissions. *Proc. Natl. Acad. Sci. USA*, **106**, 1704–1709.

Steig, E. J., K. Huybers, H. A. Singh, N. J. Steiger, Q. Ding, D. M. Frierson, T. Popp, and J. W. White, 2015: Influence of West Antarctic ice sheet collapse on Antarctic surface climate. *Geophys. Res. Lett.*, **42 (12)**, 4862–4868, https://doi.org/10.1002/2015GL063861.

Stepanek, C., E. Samakinwa, G. Knorr, and G. Lohmann, 2020: Contribution of the coupled atmosphere–ocean–sea ice–vegetation model COSMOS to the PlioMIP2. *Climate of the Past*, **16 (6)**, 2275–2323, https://doi.org/10.5194/cp-16-2275-2020.

Stevens, B., S. C. Sherwood, S. Bony, and M. J. Webb, 2016: Prospects for narrowing bounds on Earth's equilibrium climate sensitivity. *Earth's Future*, **4 (11)**, 512–522, https://doi.org/10.1002/2016EF000376.

Stuecker, M. F., and Coauthors, 2018: Polar amplification dominated by local forcing and feedbacks. *Nat. Climate Change*, **8 (12)**, 1076–1081.

Tierney, J. E., J. King, M. B. Osman, J. T. Abell, N. J. Burls, E. Erfani, V. T. Cooper, and R. Feng, 2025: Pliocene warmth and patterns of climate change inferred from paleoclimate data assimilation. *AGU Advances*, **6 (1)**.

Tierney, J. E., and Coauthors, 2020: Past climates inform our future. *Science*, **370 (6517)**, https://doi.org/10.1126/science.aay3701.

Tseng, H.-Y., and Y.-T. Hwang, 2024: Contrasting the evolution of the tropical Pacific SST responses to time-invariant extratropical forcings in the two hemispheres. *Geophys. Res. Lett.*, **51 (23)**.

van den Akker, T., W. H. Lipscomb, G. R. Leguy, J. Bernales, C. Berends, W. J. van de Berg, and R. S. van de Wal, 2024: Present-day mass loss rates are a precursor for West Antarctic Ice Sheet collapse. *EGUsphere*, **2024**, 1–25.

von Schuckmann, K., and Coauthors, 2020: Heat stored in the Earth system: where does the energy go? *Earth System Science Data*, **12 (3)**, 2013–2041, https://doi.org/10.5194/essd-12-2013-2020.

Weiffenbach, J. E., and Coauthors, 2023: Highly stratified mid-Pliocene Southern Ocean in PlioMIP2. *Climate of the Past Discuss.*, **2023**, 1–26, https://doi.org/10.5194/cp-2023-83.

Williams, R. G., V. Roussenov, T. L. Frölicher, and P. Goodwin, 2017: Drivers of continued surface warming after cessation of carbon emissions. *Geophys. Res. Lett.*, **44 (20)**, 10,633–10,642, https://doi.org/10.1002/2017GL075080.

Winton, M., K. Takahashi, and I. M. Held, 2010: Importance of ocean heat uptake efficacy to transient climate change. *J. Climate*, **23 (9)**, 2333 – 2344, https://doi.org/10.1175/2009JCLI3139.1.

Witkowski, C. R., A. S. von der Heydt, P. J. Valdes, M. T. van der Meer, S. Schouten, and J. S. Sinninghe Damsté, 2024: Continuous sterane and phytane δ13C record reveals a substantial pCO_2 decline since the mid-Miocene. *Nat. Comm.*, **15 (1)**, 5192.

Zelinka, M. D., T. A. Myers, D. T. McCoy, S. Po-Chedley, P. M. Caldwell, P. Ceppi, S. A. Klein, and K. E. Taylor, 2020: Causes of higher climate sensitivity in CMIP6 models. *Geophys. Res. Lett.*, **47 (1)**.

Zhou, C., M. Wang, M. D. Zelinka, Y. Liu, Y. Dong, and K. C. Armour, 2023: Explaining forcing efficacy with pattern effect and state dependence. *Geophys. Res. Lett.*, **50 (3)**, https://doi.org/10.1029/2022GL101700.

Zhou, C., M. D. Zelinka, A. E. Dessler, and M. Wang, 2021: Greater committed warming after accounting for the pattern effect. *Nature Climate Change*, **11 (2)**, 132–136, https://doi.org/10.1038/s41558-020-00955-x.

Zhou, C., M. D. Zelinka, and S. A. Klein, 2016: Impact of decadal cloud variations on the Earth's energy budget. *Nature Geosci.*, **9 (12)**, 871–874, https://doi.org/10.1038/ngeo2828.

Zhou, C., M. D. Zelinka, and S. A. Klein, 2017: Analyzing the dependence of global cloud feedback on the spatial pattern of sea surface temperature change with a Green's function approach. *J. Adv. Model. Earth Syst.*, **9 (5)**, 2174–2189.

Zhu, J., B. L. Otto-Bliesner, E. C. Brady, C. J. Poulsen, J. E. Tierney, M. Lofverstrom, and P. DiNezio, 2021: Assessment of equilibrium climate sensitivity of the Community Earth System Model version 2 through simulation of the Last Glacial Maximum. *Geophys. Res. Lett.*, **48 (3)**, https://doi.org/10.1029/2020GL091220.

Zhu, J., and C. J. Poulsen, 2020: On the increase in climate sensitivity and cloud feedback with warming in the Community Atmosphere Models. *Geophys. Res. Lett.*, **47**, https://doi.org/10.1029/2020GL089143.

Zhu, J., and C. J. Poulsen, 2021: Last Glacial Maximum (LGM) climate forcing and ocean dynamical feedback and their implications for estimating climate sensitivity. *Climate of the Past*, **17 (1)**, 253–267.